High temperature rheology of Zr-based bulk metallic glass forming liquids

Dissertation

zur Erlangung des Grades

Doktor der Ingenieurwissenschaften (Dr. -Ing)

der

Naturwissenschaftlich-Technischen Fakultät III
Chemie, Pharmazie, Bio- und Werkstoffwissenschaften

der

Universität des Saarlandes

vorgelegt von

William Hembree

Saarbrücken
October 30, 2015

Tag des Kolloquiums: 16.03.16
Dekan: Prof. Dr.-Ing. Dirk Bähre
1. Gutachter: Prof. Dr. rer. nat. Ralf Busch
2. Gutachter: Prof. Dr.-Ing. Dirk Bähre
Vorsitz: Prof. Dr. mont. Christian Motz
Akad. Mitarbeiter: Dr.-Ing. Dr. rer. nat. Anne Jung

Abstract

Metallic glasses are promising new materials due to their unique properties and near-net shape formability. Viscosity is a key kinetic parameter for understanding supercooled liquids. Good glass formers exhibit sluggish crystallization kinetics due to their slow atomic mobility or high viscosity. However, accurate viscosity measurements are challenging for these liquids, especially at high temperatures in the molten state. In this work, the temperature dependent rheological behavior of select zirconium based bulk metallic glasses is investigated using a custom built concentric cylinder rheometer. This device was designed, built, and programmed to measure molten metallic liquids with viscosities ranging from 10-1000 mPa s up to 1400 K. A suite of LabVIEW measurement controls and graphical data analysis was developed for this work. To verify the results from the Couette rheometer, containerless electrostatic and electromagnetic levitation measurements were used. Additionally, the kinetics near the glass transition were investigated using three point beam bending experiments.

All eight alloys unambiguously exhibit Newtonian fragile behavior above their liquidus temperatures and strong behavior near their glass transition temperatures, suggesting the existence of a liquid-liquid transition between kinetically distinct phases in these systems. Direct observation of such a transition is precluded by crystallization or by experimental limitations.

Zusammenfassung

Metallische Gläser sind vielversprechende Materialen auf Grund ihrer einmaligen Eigenschaften und endkonturnahe Umformbarkeit. Die Viskosität beschreibt der Kinetik für unterkühlten Schmelze. Gute Glasbildner zeichnen sich als hochviskose Flüssigkeiten mit langsame Kristallisations-Kinetik. Genaue Viskositätsmessungen sind sehr anspruchsvoll, insbesondere bei hohen Temperaturen. In dieser Arbeit werden der temperaturabhängigen Viskositäten von ausgesuchten Zirkon-basierende Legierungen untersucht. Dafür werden ein konzentrische-Zylinder Rheometer konzipiert, gebaut, und programmiert, deren metallische Schmelze von 10-1000 mPa s bis 1400 K messen kann. Eine Suite von LabVIEW-Tools ist für Temperatur und Bewegungskontrolle sowie grafische Datenanalyse entwickelt. Die Messungen sind mit tiegelfreier Experimente mittels elektrostatische- und elektromagnetische-Levitation verifiziert. Bei niedrigen Temperaturen, ist die Kinetik mittels Dreipunktbiegebalkenexperimente untersucht.

Diese Legierungen sind bei hohen Temperaturen fragilen newtonsche Flüssigkeiten und sind bei niedrigen Temperaturen starken Flüssigkeiten. Aus dieser kinetischer Diskrepanz wird deutlich, dass sich in die gewählten metallischen Gläser einen Flüssig-Flüssig Phasenübergang auftritt. Allerdings ist direkte Beobachtung dieser Übergang durch Kristallisation oder technische Einschränkungen verdeckt.

I dedicate this work to my grandparents

Acknowledgments

I would like to express my sincere gratitude to my supervisor Prof. Dr. Ralf Busch for his guidance and immeasurable patience over the course of both my master and doctoral studies. In addition to sharing his own insight and wisdom, he has proven to be willing to listen to new ideas and criticism. Thanks to this, he has fostered a truly wonderful group at the Chair of Metallic Materials. Because I am studying half-way across the world from home, I am profoundly grateful to the welcoming and professional atmosphere that Ralf has provided.

I would also like to thank everyone at the Chair of Metallic Materials (*Lehrstuhl für metallische Werkstoffe*, LMW) for their support and camaraderie over the course of my studies in Saarbrücken. I am incredibly grateful to Dr. Isabella Gallino for her insight and counsel on a wide range of topics as well as her unwavering congeniality. I want to thank Dr.-Ing. Frank Aubertin for the innumerable times that he has jovially contributed his boundless and diverse expertise to this project. It has been a privilege to work with Hermann Altmeyer and Jörg Eiden and this project would not have been possible without their invaluable technical assistance and masterful craftsmanship. I want to thank Martina Stemmler for her contributions to the sample characterization. I would also like to thank Sigrid Neusius for her unflinching attention to bureaucratic detail as well as for her warmth and amiability.

My peers and colleagues at the LMW have all made my stay in Germany enjoyable and I will cherish my memories with all of them. I want to thank Dr. Zach Evenson for his support over the past seven years. As a fellow Oregonian, our serendipitous acquaintance in Germany has proven to be an ongoing source of inspiration and stalwart friendship for which I am extremely grateful. I also wish to thank Dr.-Ing. Sanja Stanojevic for her level-headedness and compassion. Likewise, I would like to thank Dr.-Ing. Jochen Heinrich for his valuable fellowship and for lending his own engineering expertise to this project. I am incredibly grateful to Dr. Shuai Wei for his calorimetric contributions and many fruitful scientific discussions. In particular, I would like to acknowledge Moritz Stolpe for his singular ingenuity, brutal honesty, and keen insight in a vast array issues that extend beyond the laboratory. I am immensely grateful to an *awesome pig* known as Oliver Gross for his assistance with the calorimetric measurements as well as his efficient delegation of work among the HiWis. I also want to recognize the wild and devilish Simon Hechler

for his contagious ambition and inspiration. Of course, I also want to thank all of the research assistants for their hard work, including Benedikt Bochtler, Lisa-Yvonne Schmitt, Alexander Kuball, Maximilian Frey, and Markus Kelkel. I would especially like to thank Stefan Gärtner for his direct contributions to this work and for being one of the most diligent workers I know.

This work would not have been possible without the contributions from the incredible team at the German Institute for Materials Physics in Space. Among them, I would first like to thank Prof. Andreas Meyer, not just for coordinating the partnership with our own institute, but also for giving us the opportunity to participate in some of the most exciting experiments possible. I want to also thank Dr. Fan Yang for his pivotal role in drawing up our funding proposals. I would like to acknowledge Isabell Jonas for her rapport and generous contributions and to this work, including her fantastic measurements with the electrostatic levitation furnace. Finally, I would like to express my heartfelt thanks to the entire TEMPUS crew for lending their technical expertise to this work. The measurements on the parabolic flights were a once in a lifetime experience and they would not have been possible without the Novespace organization and cooperation between the German and French space agencies.

I also want to express my sincere gratitude towards Dr. Jamie Kruzic at Oregon State University for his invaluable guidance. Very early on in my doctoral studies, his honesty and insight prevented my project from becoming a hulking wreck.

I would like to thank Prof. Christian Stehr of Oregon State University for inspiring me to to pursue a graduate program in Germany. Along the same lines, my stay in Europe would not have been possible without the AMASE master program and the financial support of the Erasmus Mundus program. Specifically, I would like to recognize Prof. Dr.-Ing. Frank Mücklich and Dr.-Ing. Flavio Soldera for their invaluable support during those early years of my stay in Germany. Finally, this work would not have been possible without funding from the German Research Foundation (*Deutsche Forschungs Gemeinschaft*, DLR).

I want to give special thanks to friends like Mik Larsen, Charles Dickerman, Emery Garcia, Loren Albert, Victoria Mejía, and countless others who have given me support and encouragement during my studies in Germany regardless of the borders and lands that separate us.

Lastly, I would like to express my heartfelt gratitude towards my family for their perpetual love and encouragement. My parents, Susan and David Hembree have always supported my endeavors, no matter how far away from home they take me. My brother Paul has been a constant source of inspiration and friendship, and I hope to one day attain his level of accomplishment and brilliance. My life abroad would have been impossible without their support.

Contents

Chapter 1

Introduction

Since their discovery in the 1960s, considerable effort has been devoted to the research and development of metallic glasses. These materials eschew the periodic lattice structure of conventional crystalline alloys, instead exhibiting an amorphous arrangement of atoms. Metallic glasses are attractive candidates for technological applications due to their exceptional material properties and ability to be processed in the supercooled liquid region. Studies of their thermophysical properties are crucial not only for industrial processing parameters but also for understanding the nature of glasses and supercooled liquids.

As glass forming liquids are undercooled, they exhibit a drastic dynamic slowdown until eventually falling out of equilibrium at the glass transition. The atomic mobility is reflected in the changes in transport properties such as viscosity or diffusivity. The degree to which these properties adhere to Arrhenius behavior leads to the "fragility" classification of liquids. On the one hand, liquids that exhibit Arrhenius behavior, such as SiO_2, are known as *strong* liquids. On the other hand, non-Arrhenius liquids, such as o-Terphenyl, are known as *fragile* liquids. Metallic glasses belong to neither extreme and tend to have intermediate fragilities. Recent studies have shown evidence for a dynamic crossover in various glass forming systems. This crossover has been related to polyamorphous transitions between compositionally identical phases with distinct thermodynamic and kinetic signatures This phenomenon has garnered significant research attention and evidence for such transitions have been found in a variety of glass forming systems, including water, SiO_2, Y_2O_3-Al_2O_3, and a number of metallic glasses. The precise origin of polyamorphism and it's link with the changes in fragility are, however, still poorly understood. Chapter 2 introduces some of the background of glass forming and expands upon the phenomenology of fragility.

This work is principally concerned with investigations of the kinetic behavior of metallic glass forming liquids across a wide range of temperatures. All compositions chosen for this study are Zirconium-based alloys with varying degrees of compositional complexity and glass forming ability. Several belong to the Vitreloy family, including $Zr_{58.5}Cu_{15.6}Ni_{12.8}Al_{10.3}Nb_{2.8}$ (Vitreloy 106a), $Zr_{57.0}Cu_{15.4}Ni_{12.6}Al_{10.0}Nb_{5.0}$ (Vitreloy 106), $Zr_{52.5}Cu_{17.9}Ni_{14.6}Al_{10.0}Ti_{5.0}$ (Vitreloy 105), and $Cu_{47.0}Ti_{34.0}Zr_{11.0}Ni_{8.0}$ (Vitreloy 101). Additionally, two alloys based off of Vitreloy 106a that were recently developed by J. Heinrich [121] were included in this study, namely $Zr_{59.3}Cu_{28.8}Al_{10.4}Nb_{1.5}$ (AMZ4) and $Zr705_{60.8}Cu_{28.8}Al_{10.4}$ (AMZ4 705), the latter of which substitutes high purity Zirconium and Niobium with an industrial grade Zr-R60705 pre-alloy. Finally, $Zr_{65.0}Cu_{17.5}Ni_{10.0}Al_{7.5}$ and $Zr_{60.0}Cu_{25.0}Al_{15.0}$ were studied, both of which were originally discovered by Inoue et al. [42].

The kinetic investigations were accomplished through experimental measurements of the viscosity. Near the glass transition temperature, isothermal three point beam bending experiments were used to determine the equilibrium viscosities. As the title of this dissertation implies, the bulk of the work was concerned with measurements at high temperatures near the melting point. Due to the challenges of working with reactive melts at high temperatures, a combination of independent experiments were conducted, including measurements in a custom built concentric cylinder rheometer as well as in containerless electromagnetic and electrostatic levitation furnaces. As part of this work, the custom built concentric cylinder (Couette) rheometer was designed, constructed, and programmed. This machine is the successor to the Couette rheometer used by Way et al. to study the Strong-Fragile transition in Vitreloy 1. Due to an unfortunate series of technical issues, the former machine was retired and the present work was initiated. The details of the machine design process as well as the required calculations are outlined in chapter 3. The other techniques are summarized in detail in chapter 4 and the results and discussion are presented in chapter 5. Chapter 6 summarizes the conclusions of this work and provides a brief outlook.

Chapter 2

Background

David Turnbull's research in the 1950's on the kinetics of undercooled liquid metals led to the prediction that it was possible to freeze nearly any liquid into a glassy state if the onset of crystallization could be avoided [166–169, 171]. Shortly thereafter, the first successful synthesis of a metallic glass was reported by Pol Duwez and coworkers in 1960, who used splat quenching to produce 10 μm thick amorphous flakes of $Au_{75}Si_{25}$ at cooling rates of 10^6 Ks^{-1} [176]. Over the next ten years, the Chen and Turnbull discovered ternary Pd-based alloys with improved glass forming ability and could eventually use conventional suction casting to produce amorphous rods of Pd-Cu-Si alloys up to 1 mm in diameter with cooling rates of only 10^3 Ks^{-1} [22–24]. This led to the first of the so called "bulk" metallic glasses (BMGs), which are classified by having critical thicknesses exceeding 1 mm. The collaboration of Drehman, Greer, and Turnbull in 1982 led to the discovery that heterogeneous nucleation in Pd-Ni-P alloys could be futher suppressed with fluxing with boron oxide, leading to the fabrication of amorphous samples with thicknesses of 1 cm with cooling rates as low as 10 Ks^{-1} [3]. As metallic glasses garnered more attention from researchers, the scope of compositions also expanded beyond the confines of Au- or Pd-based alloys. For example, in the 1990's Inoue and colleagues studied La-Al-Ni [38], La-Al-Cu-Ni [41], Mg-Y-Cu [40], Mg-Y-Ni [123], and Zr-Cu-Ni-Al [39, 42] alloys, all of which showed exceptional glass forming ability. The first commercial family of BMGs was developed by Peker and Johnson in 1993, including the extensively studied composition $Zr_{41.2}Ti_{13.8}Cu_{12.5}Ni_{10}Be_{22.5}$ (known as Vitreloy 1 or Vit1) [147,148] which could be cast into fully amorphous samples beyond a centimeter thickness without the use of fluxing or any complicated processing methods.

There are a wide variety of methods for synthesizing metallic glasses. Early attempts relied upon rapid quenching techniques, such as splat quenching or melt spinning. With the development of BMGs with increasing glass forming

ability, rapid solidification techniques also grew to encompass conventional casting into cooled molds. However, production of metallic glasses is not restricted to rapid solidification techniques from the liquid. Vapor deposition methods are also used to create thin amorphous films on cooled substrates. Furthermore, amorphous phases can be synthesized through solid-state reactions or through mechanical alloying methods.

Over the course of their development, considerable effort has been dedicated to understanding and improving the glass forming ability (GFA) of these systems. Two common metrics of the GFA are the critical cooling rate, R_c, and the critical casting thickness, D_c, both of which describe the requisite heat extraction for solidification into a glass. In this chapter, some of the thermodynamic and kinetic factors that contribute to the GFA will be discussed. Much of the information on thermodynamics and kinetics can be found in textbooks such as [28, 115] and is summarized here in the words of the author.

2.1 Glass formation

As a liquid is cooled below the melting temperature T_m, it will remain as a metastable supercooled liquid until either crystallizing or until structural arrest and vitrification occurs at the glass transition. The formation of a glass from a supercooled liquid depends on the conditions for bypassing crystallization. It is necessary, therefore, to understand the processes of crystallization, which occurs by the formation of crystalline nuclei and their subsequent growth. The thermodynamic driving force for crystallization is the difference between Gibbs free energy of the liquid and crystalline phase (see figure 2.1)

$$G^L = H^L - TS^L \tag{2.1}$$

$$G^X = H^X - TS^X \tag{2.2}$$

$$\Delta G = \Delta H - \Delta T \Delta S \tag{2.3}$$

Driven by thermal perturbations, the formation of a crystalline nucleus requires atomic rearrangements within the liquid and a departure from equilibrium. For nucleation to proceed, the energy to form a stable volume of the crystalline phase, ΔG_v, must overcome its interfacial energy with the surrounding liquid, γ_s.

The simplest case in which this can occur is for the *homogeneous nucleation* of a spherical cluster of radius r within the bulk of the liquid phase, whose driving force is given by

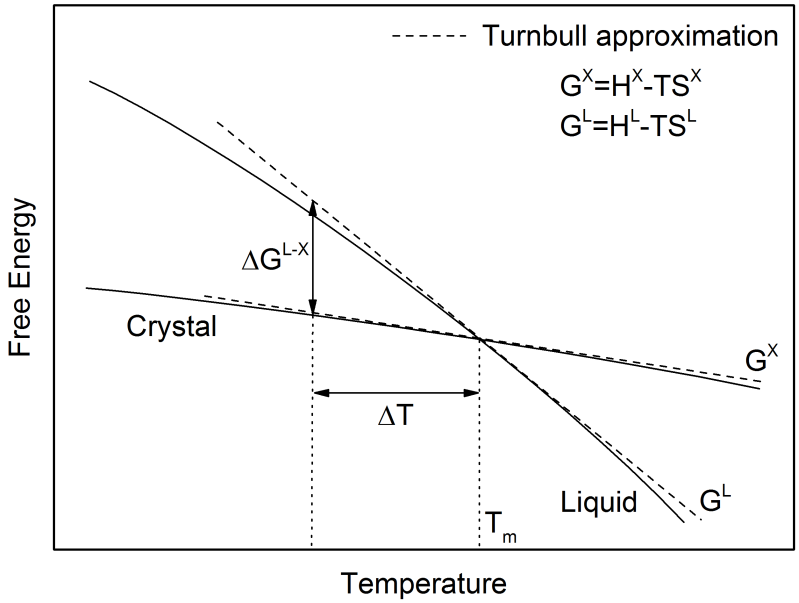

Figure 2.1: Illustration of the Gibbs free energy of a liquid and crystalline phase. The Turnbull approximation gives the the driving force for crystallization ΔG^{L-X} for small undercoolings ΔT.

$$\Delta G_{hom} = -\frac{4}{3}\pi r^3 \Delta G_v + 4\pi r^2 \gamma_s \tag{2.4}$$

Where first term on the right hand side describes the volume energy which is proportional to $-r^3$ and the second term describes the interfacial energy which is proportional to r^2. Differentiation of equation 2.4 yields the critical nucleus radius r^*

$$r^* = \frac{2\gamma_s}{\Delta G_v} \tag{2.5}$$

If the clusters have a radius smaller than the critical radius $r < r^*$, then they are unstable embryos whose dissolution is energetically favored. Conversely, those having radii exceeding the critical radius $r > r^*$ are stable nuclei. For small undercoolings, the free energy difference can be approximated by the entropy of fusion at the melting temperature

$$\Delta G = \Delta S_f \Delta T = \frac{\Delta H_f \Delta T}{T_m} \tag{2.6}$$

where ΔS_f and ΔH_f are the entropy and enthalpy of fusion, respectively. Substituting equation 2.6 into 2.5 allows the expression of the critical radius r^* for a given undercooling ΔT as

$$r^* = \frac{2\gamma_s T_m}{\Delta H_f} \frac{1}{\Delta T} \tag{2.7}$$

similarly, the critical energy barrier for nucleation ΔG^* is

$$\Delta G^*_{hom} = \frac{16\pi\gamma_s^3 T_m^2}{3\Delta H_f^2} \frac{1}{\Delta T^2} \tag{2.8}$$

While useful for its simplicity, homogeneous nucleation is actually quite difficult to realize in real world settings due to the presence of heterogeneities that act as preferential nucleation centers. These heterogeneities are typically second phase particles, free surfaces, or interfaces with solid container walls. Due to its impact on this work, it is worth spending some time discussing *heterogeneous nucleation* and its implications on crystallization.

Volmer [175] derived the work required for heterogeneous nucleation of a secondary phase β within some primary α phase by considering the wetting behavior of the nucleus to a flat solid substrate, shown schematically in figure 2.2. The interfacial energy of each phase relative to each other is related to the wetting angle by $\gamma_{\alpha S} = \gamma_{\beta S} + \gamma_{\alpha\beta}\cos\theta$. Forming a nucleus of some volume V_β will result in an excess free energy of

$$\Delta G_{het} = V_\beta \Delta G_V + A_{\alpha\beta}\gamma_{\alpha\beta} + A_{\beta S}\gamma_{\beta S} - A_{\beta S}\gamma_{\alpha S} \tag{2.9}$$

The increase in energy associated with the creation of the interfaces between the α and β phases and between the β phase and substrate is balanced against the creation of some energetically favorable volume of β as well as against the removal of the interfacial area between the α phase and substrate. For a constant nucleus radius, the critical energy barrier for heterogeneous

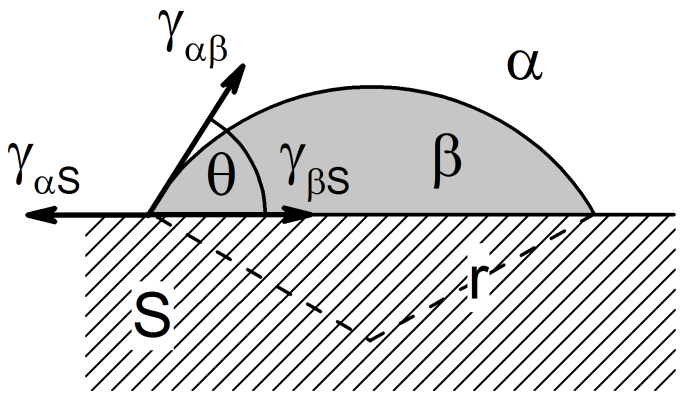

Figure 2.2: Illustration the nucleation of a crystalline nuclei (β) of radius r from the liquid (*alpha*) to the surface of a solid heterogeneity (S). The wetting angle θ is determined by the relative surface tensions between the nucleating phase and the heterogeneity $\gamma_{\alpha\beta}$, the nucleating phase and the surrounding liquid $\gamma_{\beta L}$, and the surrounding liquid and the heterogeneity $\gamma_{\alpha L}$.

nucleation differs from that of homogeneous nucleation only by a geometric factor $S(\theta)$, or

$$\Delta G^*_{het} = \Delta G^*_{hom} S\left(\theta\right) = \left[\frac{16\pi\gamma_s^3 T_m^2}{3\Delta H_f^2}\frac{1}{\Delta T^2}\right] S\left(\theta\right) \tag{2.10}$$

where the surface factor $S(\theta)$ is

$$S(\theta) = \frac{\left(2+\cos\theta\right)\left(1-\cos\theta\right)^2}{4} \tag{2.11}$$

In the case where the droplet does not wet to the surface, $\theta = 180$, the surface factor is equal to unity and the case for homogeneous nucleation is reproduced. Meanwhile, for the case of a droplet wetting to the surface, $S(\theta) \leq 1$, the energy barrier for nucleation is reduced proportionally. For perfect wetting, $S(\theta) = 0$, there are no barriers for nucleation at the surface. As a consequence, heterogeneous nucleation sites promote crystallization by reducing the thermodynamic energy barrier $\Delta G^*_{het} \leq \Delta G^*_{hom}$, as shown schematically in figure 2.3

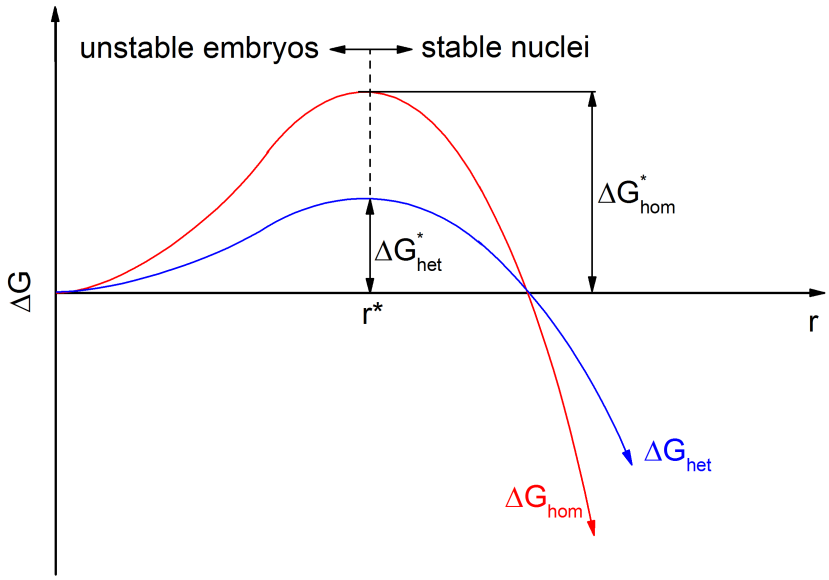

Figure 2.3: The excess free energy requirements for heterogeneous nucleation are smaller than those for homogeneous nucleation $\Delta G^*_{het} \leq \Delta G^*_{hom}$ for a fixed critical radius $r*$.

At any given undercooling, the number of clusters that have reached the critical size can be described by a Boltzmann distribution describing the probability that they have reached the critical energy barrier

$$n^*_r = n_0 exp\left(-\frac{\Delta G^*}{kT}\right) \tag{2.12}$$

where n_0 is the number of atoms in the system for homogeneous nucleation and is the number of atoms in contact with heterogeneities for heterogeneous nucleation. Depending on the kinetic fluctuations within the liquid, atoms may attach or detach from these clusters. Stable nuclei will form if one or more atoms is added to these critical clusters and the chance of this occurring increases with increasing undercooling. Under steady state conditions, the rate of nucleation can be expressed as

$$I = I_0 exp\left(-\frac{\Delta G^*}{kT}\right) \tag{2.13}$$

The pre-factor can be expressed as $I_0 = 4\pi r^* n_l v_0 p n_c$, where n_l is the number of atoms in the metastable liquid, v_0 is the atomic vibration frequency,

p is the probability that an atom adheres to a critical nucleus, and n_c is the number of adsorption sites per unit area [163]. Since the variations in I_0 are very small compared to the exponential term in equation 2.13, the pre-factor is often simplified to $I_0 = n_l v_0$, which is about $10^{42}\mathrm{m}^3\mathrm{s}$ for metallic systems. However, this rather simplified interpretation of I_0 has received criticism since it neglects dynamic processes such as fluctuations in local structure [146]. In spite of these contentions, equation 2.13 remains useful for a qualitative description of the underlying principles of nucleation.

In light of this assessment, it is helpful to note that the pre-exponent I_0 is directly proportional to the diffusivity (or inversely with viscosity) and shares a thermally activated exponential change with decreasing temperature that can be described by $exp\,(-Q/RT)$. Consequently, in addition to low thermodynamic critical energy barriers, a high atomic mobility will also provide favorable conditions for the nucleation of crystals. Because this mobility decreases rapidly upon undercooling, nucleation becomes kinetically limited at very low temperatures. Thus, the nucleation rate will have some peak value determined by the balance of the increasing driving force and decreasing atomic mobility with undercooling.

Once crystalline nuclei have formed, their size distribution is determined by the growth processes involved, which can be broken down once again into diffusional and interfacial mechanisms. The growth of nuclei at the expense of the surrounding liquid phase depends largely on the morphology of the crystal-liquid interface [172]. According to the criteria developed by Jackson [125], rough or diffuse interfaces are expected for materials with small entropies of fusion $\Delta S_f < 2R$, while smooth interfaces are expected for large entropies of fusion $\Delta S_f < 4R$. In the former case, the growth velocity is well described by

$$u(T) = va_0 \left[1 - exp\left(-\frac{\Delta G^{l-x}}{RT}\right)\right] \tag{2.14}$$

Because both nucleation and growth rates are strongly correlated with undercooling, Turnbull devised the reduced glass transition temperature $T_{rg} = T_g/T_m$ as an empirical means of predicting the glass forming ability of a system [170]. By definition, the viscosity at T_g is 10^{12} Pa s, at which point it's mechanical behavior is indistinguishable from a solid. Since $I(T)$ and $u(T)$ are both inversely proportional to the viscosity of the liquid, higher values of T_{rg} correspond to a system's ability to kinetically suppress crystallization. According to Turnbull, for values of $T_{rg} \geq 2/3$, the homogeneous nucleation of crystals is constrained to a narrow temperature range for which the growth rates are relatively slow, shown schematically in figure 2.4. As a result, the liquid may be more readily undercooled to the glassy state.

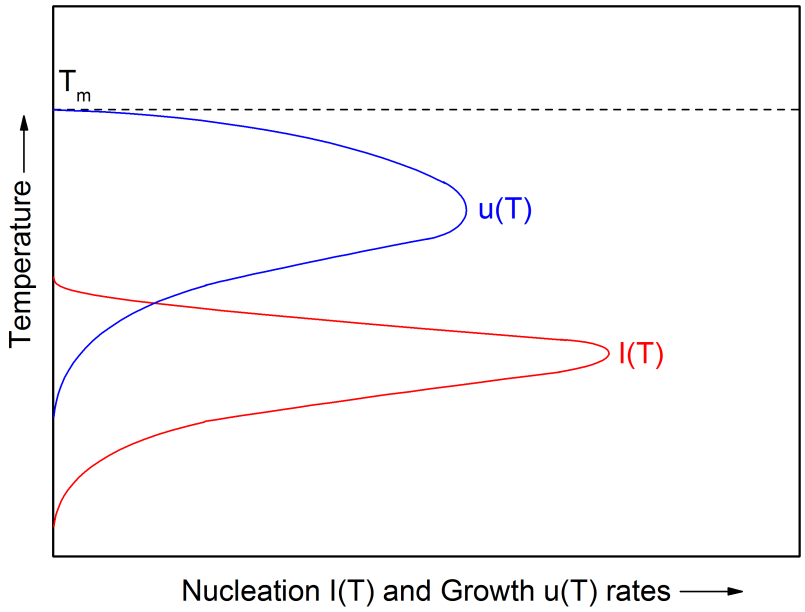

Figure 2.4: Schematic diagram showing how the rate of homogeneous nucleation $I(T)$ and growth $u(T)$ vary with undercooling. In good glass forming systems, the peak nucleation rate is accompanied by only a very slow diffusional limited growth.

If the growth rate is assumed to be constant and if the nuclei do not impinge on one another, then the volume fraction of the crystalline phase at short times, including those having nucleated after some delay τ, is given by

$$X = \frac{4}{3}\pi I u^3 \int_0^t (t-\tau)^3 \, d\tau = \frac{\pi}{3} I u^3 t^4 \tag{2.15}$$

For longer times the *Johnson-Mehl-Avrami-Kolmogorov* (JMAK) equation [11, 127, 131] can be used to more accurately predict the volume fraction of crystals after some time

$$X = 1 - exp\left(-\frac{\pi}{3} I u^3 t^4\right) \tag{2.16}$$

which reproduces equation 2.15 for very short times and small volume fractions. This can be rewritten then in terms of time as

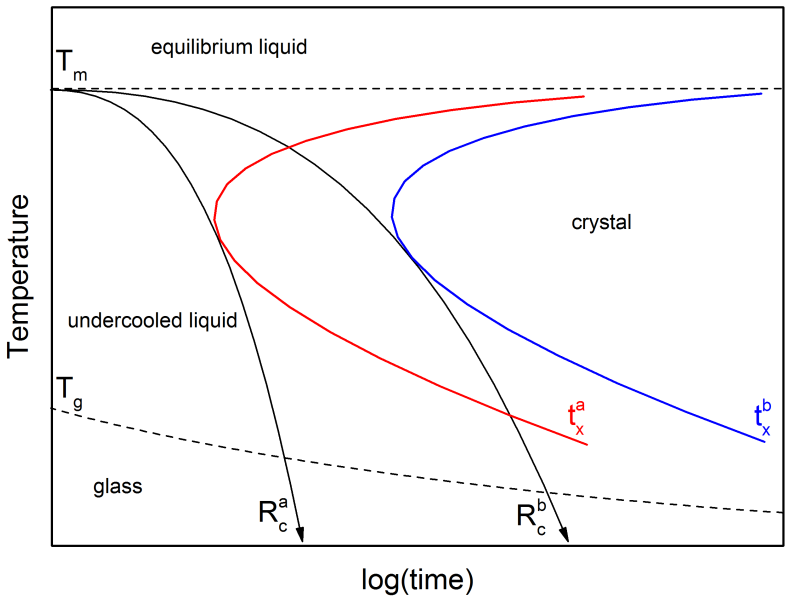

Figure 2.5: Time-Temperature-Transformation diagram for two glass forming systems a (red) and b (blue). System b is a better glass former due to its lower critical cooling requirements, $R_c^b < R_c^a$.

$$t_x = \left(\frac{3X}{\pi I u^3}\right)^{1/4} \tag{2.17}$$

For a defined observable volume fraction of crystals, the onset time t_x for crystallization for various isothermal treatments can be found using equation 2.17. By plotting the calculated logarithmic onset times versus temperature, an isothermal *Time-Temperature-Transformation* (TTT) diagram can be defined for a system, shown schematically in figure 2.5. The characteristic "nose" shape is a direct consequence of the competing thermodynamic and kinetic limitations of crystallization nucleation and growth. In order to form a glass during undercooling from the liquid state, the onset of crystallization must be avoided. Systems with longer times until the onset of crystallization have smaller necessary critical cooling rates, R_c, and are more readily cooled to the glassy state.

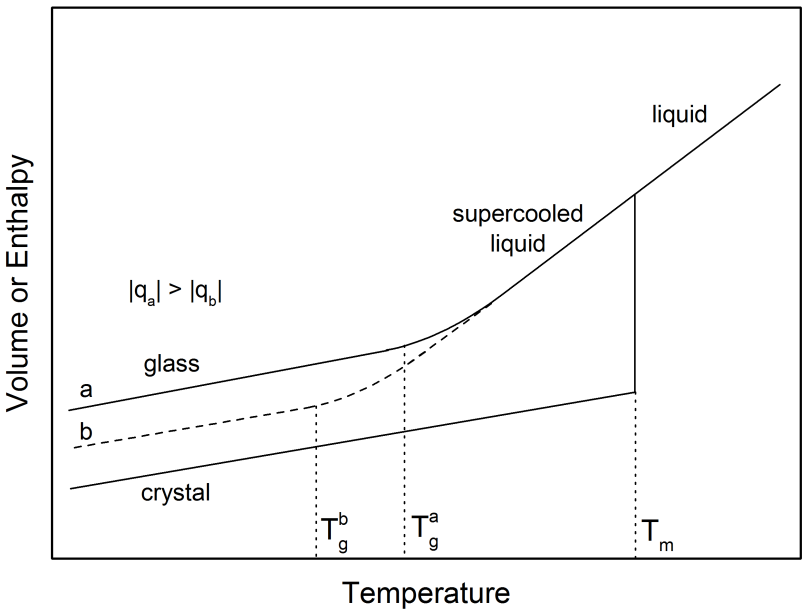

Figure 2.6: As a liquid is undercooled from the equilibrium state, it will either freeze into the crystalline phase at T_m or be frozen into the glassy state at T_g. The former transition is associated with a discontinuous change in the volume and enthalpy, while the latter shows a continuous change. T_g will be shifted to lower temperatures at slower cooling rates q.

2.2 The glass transition

If a liquid is undercooled and the intervening crystallization is avoided, the atomic mobility decreases until the time necessary for *structural relaxation* prevents complete equilibration on laboratory timescales. Structural relaxation refers to the time necessary for a system to return to equilibrium after some perturbation and can be related to the viscosity through the Maxwell expression $\eta = \tau G_\infty$, where G_∞ is the instantaneous shear modulus. This transition is accompanied with a monotonic decrease in the rate of change of volume, enthalpy, or entropy with temperature until eventually falling out of equilibrium and freezing into the glassy state. The $H(T)$ or $V(T)$ curves of the frozen in glass run parallel to the crystalline solid state as shown schematically in figure 2.6. Unlike crystallization at the freezing point, vitrification occurs over a range of temperatures and furthermore, T_g depends on the rate at which the liquid is cooled $q = dT/dt$. Therefore, the glass transition is considered a kinetic event rather than a true thermodynamic transition. The lower the cooling rate is, the more time the system has to change between available structural configurations. Consequently, the system will be able to remain in the metastable undercooled liquid state longer and T_g will be shifted to lower temperatures [51, 53].

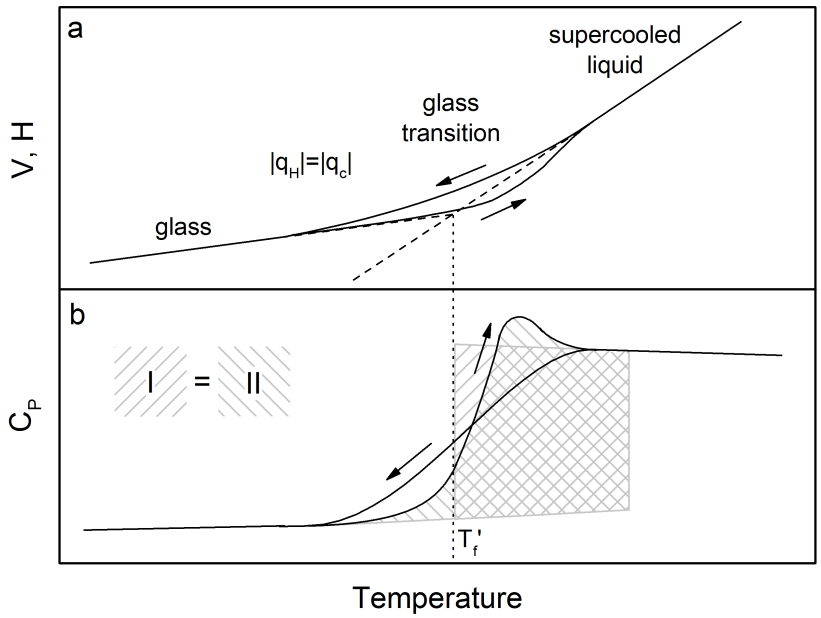

Figure 2.7: The limiting fictive temperature T_f' for a glass that has been cooled or heated at some rate $|q|$ through the glass transition is found by extrapolating the thermodynamic property of the glassy state to that of the metastable equilibrium liquid (a). Experimentally, it can be found by determining the temperature at which the areas I and II are equivalent under the specific heat curve upon heating through the glass transition (b).

Upon subsequent reheating at the same rate as cooling, $|q|$, the volume or enthalpy will follow the same path as the cooling curve until reaching the glass transition itself, at which point it continuously deviates from the original path and moves towards the equilibrium liquid state until eventually rejoining the curve at the end of the transition. This hysteresis between the heating and cooling curves arises from the tendency for the system to move towards equilibrium with time.

Because the glass transition occurs over a range of temperatures, it is useful to use the concept of a *limiting fictive temperature* to define the glassy configuration that is obtained for a given cooling rate. A fictive temperature T_f can be defined anywhere that the thermodynamic properties of the glass and equilibrium liquid are equal. Extrapolating the enthalpy or volume curve of the glass to the equilibrium state gives the limiting fictive temperature, T_f', for that particular glass as shown in figure 2.7a [52, 83].

Experimental investigations of the glass transition are commonly performed with calorimetric measurements of the specific heat. The change in isobaric specific heat upon cooling or heating across the glass transition at the same rate is shown in figure 2.7b. The hysteresis in the thermodynamic properties caused by the additional relaxation upon reheating through the glass transition

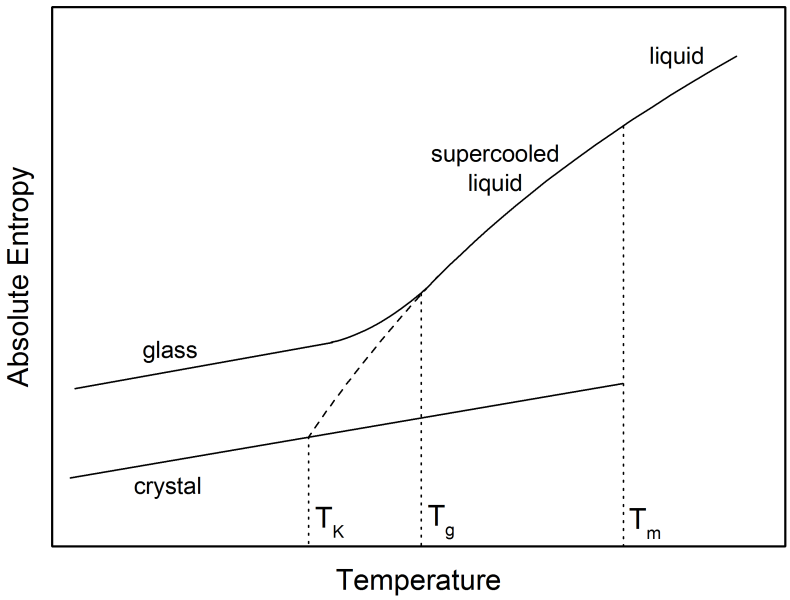

Figure 2.8: The change in absolute entropy with temperature for a liquid and the underlying thermodynamically stable crystalline phase. The dashed line represents an extrapolation of the entropy of the supercooled liquid at infinitely slow cooling rates, resulting in the Kauzmann paradox at $0 < T_K < T_g$.

manifests as an overshoot in the heat capacity. Moynihan and coworkers [52] outlined a means of determining T_f' with two equivalent areas defined by the integral expression

$$\int_{T^*}^{T_f'} \left(C_p^{eq} - C_p^{glass}\right) dT_f = \int_{T^*}^{T'} \left(C_p - C_p^{glass}\right) dT \tag{2.18}$$

where T' and T^* are temperatures below and above the glass transition, respectively. The shaded areas in figure 2.7b correspond to the two integral terms. As a result, the limiting fictive temperature can be defined for the glass configuration obtained at any given cooling rate.

One of the defining features of the undercooled liquid state is that it exhibits a higher heat capacity relative to that of the thermodynamically stable crystalline phase. However, what happens if the liquid could be undercooled at an infinitely slow rate without the intervention of crystallization or the kinetic glass transition? In 1948, Kauzmann outlined the ramifications of this hypothetical situation and identified what remains as one of the most significant questions in glass science [129]. Figure 2.8 illustrates this scenario, where the extrapolation of the entropy of the liquid state to low temperatures eventually crosses that of the crystal at some temperature T_K. This apparent

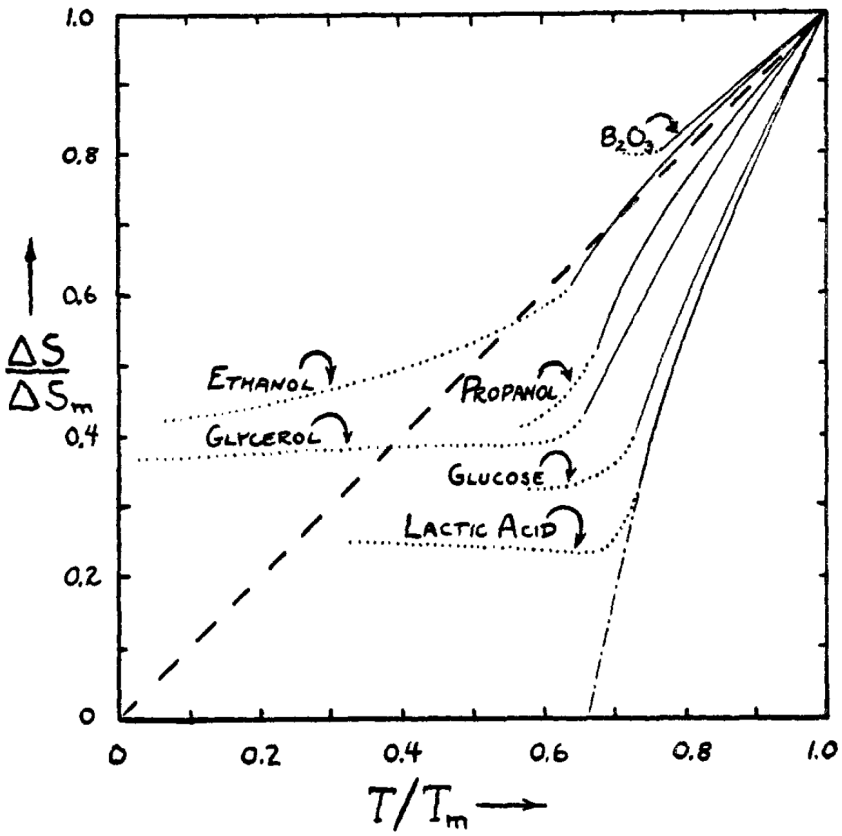

Figure 2.9: Kauzmann's plot of the differences in entropy between the supercooled liquid and crystalline phases normalized to the entropy of fusion ΔS_m for a selection of glass forming liquids, adapted from [129].

violation of the third law of thermodynamics in what is now known as the *Kauzmann paradox*.

The difference in entropy between the liquid and crystal normalized to the entropy of fusion is shown for a select number of glass formers in figure 2.9 [129]. To avoid the thermodynamic catastrophe, a second order transition to an "ideal" glass whose structure remains unchanged below T_K [111, 159]. Kauzmann supposed that the free energy barrier for crystallization would diminish to zero above T_K, such that spontaneous homogeneous nucleation would prevent the entropy paradox. However, as has already been shown in figure 2.4 and reported elsewhere [4,158], the nucleation rate passes through a maximum before being kinetically limited with further decreases in undercooling. To this day, work continues to explain the thermodynamic and kinetic behavior of undercooled liquids.

2.3 Kinetic slowdown and fragility

Upon undercooling, glass forming liquids exhibit a drastic kinetic slowdown, manifesting in measurable changes in shear viscosity, η, relaxation times, τ, and the self-diffusion constant, D. The viscosity represents a liquid's resistance to applied shear stresses and increases up to sixteen orders of magnitude from the equilibrium liquid at T_m to the glass at T_g. Viscosity and the diffusion coefficient can be related according to the Stokes-Einstein equation [36]

$$D = \frac{k_B T}{6\pi r \eta} \tag{2.19}$$

where r is the radius of the diffusing particle. The rapid deceleration of the liquid dynamics has been shown to follow non-Arrhenius behavior for many glass forming systems. For Arrhenius behavior, the viscous flow can be described by the activation energy $E(T)$ that must be overcome for atomic rearrangements [150]

$$\eta(T) = \eta_0 \exp\left(\frac{E(T)}{RT}\right) \tag{2.20}$$

where η_0 is the limit of viscosity at high temperatures. The lower limit of viscosity can be expressed as $\eta_0 = hN_A/v_m$, where h is Plank's constant, N_A is Avogadro's number, and v_m is the atomic volume [143]. However, the activation energy in equation 2.20 varies with temperature for real liquids [12] and is often described by the empirical Vogel-Fulcher-Tamman (VFT) equation [109, 161, 174]

$$\eta(T) = \eta_0 \exp\left(\frac{D^* T_0}{T - T_0}\right) \tag{2.21}$$

where the parameter D^* describes how closely the behavior is described by an Arrhenius law, T_0 is the temperature at which the barriers to flow approach infinity. The VFT equation reproduces an Arrhenius law for the limits as $D^* \to \infty$ and $T_0 \to 0$.

Angell developed the *fragility* classification of glasses, where "fragile" liquids show a super-Arrhenius rise in viscosity near T_g, while "strong" liquids

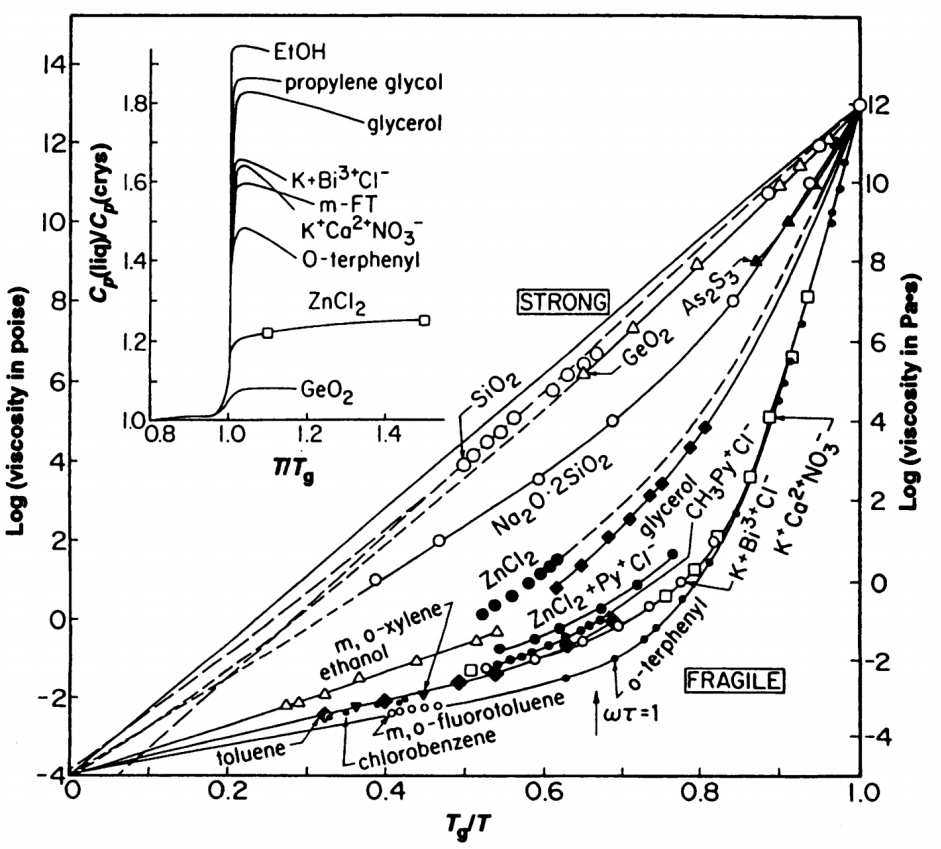

Figure 2.10: Arrhenius plot of the viscosity scaled to the glass transition temperature of several liquids. The inset shows that the jump in heat capacity at T_g is typically smaller for strong liquids than for fragile ones. Figure adapted from [5].

maintain a near-Arrhenius kinetic slowdown [5]. Figure 2.10 shows the logarithmic viscosities normalized to the glass transition temperatures for several glass forming liquids, highlighting the wide variety of kinetic fragilities among glass formers. In addition to the parameter D^*, the kinetic fragility can be described by an effective activation enthalpy at T_g known as the kinetic fragility index, m, which is the slope of the viscosity curve at the glass transition temperature

$$m = \left.\frac{d\log_{10}\eta}{d\left(T_g/T\right)}\right|_{T=T_g} \tag{2.22}$$

The parameters m and D^* are related by $m = 16 + 590/D^*$.

Because of the purely empirical basis of the fitting parameters, the VFT-equation offers a unsatisfactory description of the underlying mechanisms for viscous flow. Indeed, some systems do not comply with a simple three parameter model and require additional fitting parameters [119]. Therefore, several other models have been developed in order to offer a phenomenological description of the kinetic slowdown, the most widely used of which are the entropy and free volume models.

Gibbs and Dimarzio [29–31, 111] developed a statistico-mechanical theory which attributed the slowdown of relaxation behavior upon undercooling to the scarcity of available configurations. This theory became the basis for the probabilistic description of cooperative rearrangements outlined by Adam and Gibbs [2] which describes the relaxation or viscous slowdown in terms of the configurational entropy,

$$\eta = \eta_0 \exp\left(\frac{C}{TS_c}\right) \tag{2.23}$$

where C is a constant representing a free energy barrier to cooperative rearrangements and $S_c = S_{glass} - S_{crystal}$ is the configurational entropy. Relaxation in the Adam-Gibbs model involves the thermal activation of cooperatively rearranging regions of molecules that are considered independently from the surroundings and have a finite and diminishing number of available configurations at low temperatures. At a given temperature, $S_c(T)$ describes the number of possible atomic configurations that are available. If the excess entropy at T_K is equivalent to the configurational entropy, this model eloquently resolves the Kauzmann paradox with a divergence in relaxation time towards infinity, which is concomitant with a second-order phase transition when $S_c = 0$.

Alternatively, the free-volume model has been used to describe the kinetic slowdown upon undercooling towards the glass transition. Fox and Flory [106–108] suggested that molecular transport is enabled by the presence of holes through which free motion is possible. Cohen and Turnbull [25, 170] expanded this concept to describe the diffusive slowdown in simple liquids. Originally based on a hard sphere model, the free-volume theory proposes that atomic mobility is constrained within a cage defined by the neighboring molecules. In terms of the viscosity, the free-volume model is given by the Doolittle expression [32]

$$\eta = \eta_0 \exp\left(\frac{bv_0}{v_f}\right) \tag{2.24}$$

where b is a numerical material factor on the order of unity, v_f is the average free volume per molecule, and v_0 represents a critical volume necessary for motion. Cohen and Turnbull expressed the temperature dependence of the average free volume per molecule in terms of the volumetric thermal expansion coefficients of the liquid and glass, $v_f = v_m(\alpha_l - \alpha_g)(T - T_0)$, where v_m is the atomic volume and T_0 is the temperature at which viscous flow is no longer possible. Cohen and Grest [117] would later improve the description of the free volume by incorporating the effect of solid-like cells in the environment, resulting in

$$v_f = \frac{k_B}{2\zeta_0}\left(T - T_q + \sqrt{(T - T_q)^2 + \frac{4v_a\zeta_0}{k_B}T}\right) \tag{2.25}$$

where T_q, $k_B(2\zeta_0)^{-1}$, and $4v_a\zeta_0 k_B^{-1}$ are fitting constants.

2.3.1 Glass forming ability

Considerable effort has been devoted to understanding the conditions that improve the glass forming ability (GFA) of alloys. Considering glass formation from a purely kinetic perspective, Turnbull devised an empirical method for predicting the glass forming ability of a system using the ratio of the glass transition temperature to the liquidus temperature of a system. This ratio is known as the reduced glass transition temperature, where $T_{rg} = T_g/T_l$. For increasing values of T_{rg}, the viscosity of the undercooled melt should be higher and the rate of homogeneous nucleation should be slower, permitting vitrification with lower critical cooling rates. For systems where $T_{rg} \geq 2/3$, the homogeneous nucleation of crystals should be completely suppressed. This condition is most easily realized in systems with deep eutectic compositions where the driving force for crystallization is small.

Another set of empirical criteria for developing BMGs and improving their GFA was developed by Inoue [160]. First, the alloy should contain at least three components. An increasing number of constituent elements improves the GFA. Second, there should be a difference in atomic size of about 12% between the main elements. Third, the major constituent elements should have a negative heat of mixing. The combination of these factors leads to a densely packed liquid and the destabilization of the crystalline lattice, thereby improving the GFA.

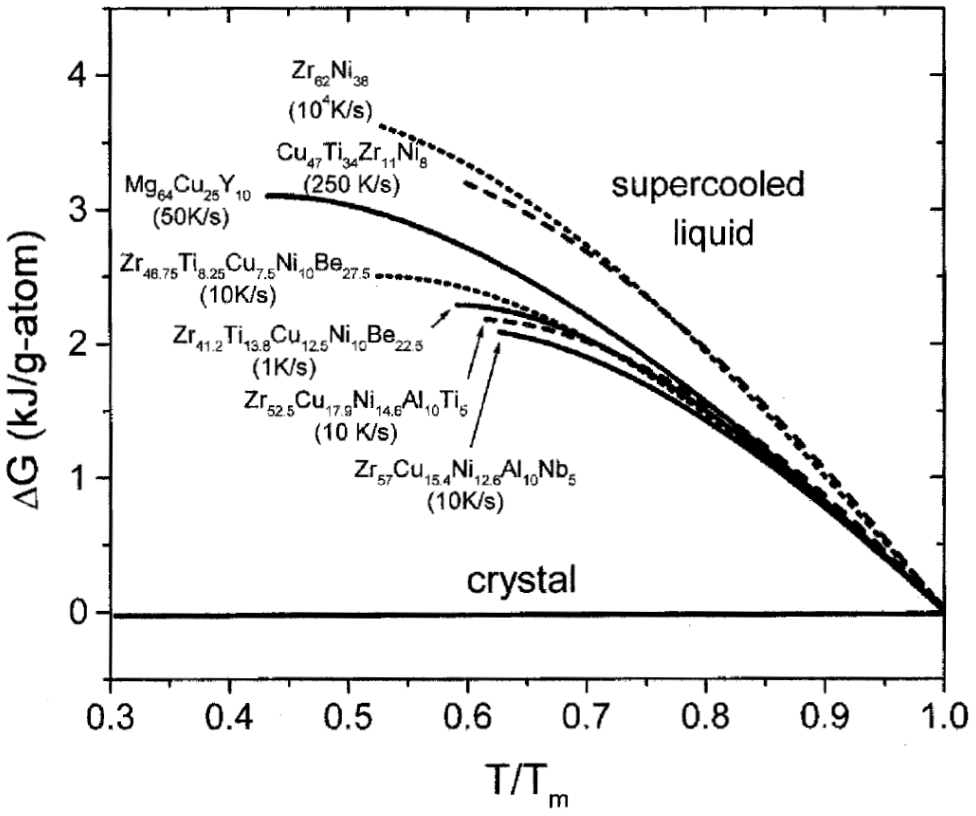

Figure 2.11: A plot of the Gibbs free energy difference between the liquid and crystalline state, ΔG_{l-x}, for various glass forming systems with the critical cooling rate indicated for each alloy. Systems with lower critical cooling rates typically have shallower curves. Adapted from [18].

Thermodynamically, the Gibbs free energy difference ΔG_{l-x} between the liquid and crystal determine the GFA of a system. In a comparative study of the specific heat capacities of various metallic glass forming systems, Busch showed that systems with the lowest critical cooling rates typically had smaller ΔG_{l-x} [18]. The slope of the free energy curve is determined by the entropy at the melting point. The lower the entropy is, the smaller the free volume will be, and therefore the undercooled liquid will be more likely to be highly viscous with short range order.

The relationship between the viscosity of undercooled liquids and glass forming ability was summarized in a study by Busch and coworkers [18]. A liquid's viscosity reflects its atomic mobility and is therefore the key parameter for determining the crystallization nucleation and growth rates. Pure metals or binary alloys have melt viscosities on the order of 10^{-3} Pa s and tend to be very poor glass formers due to their rapid kinetics. In contrast, good glass formers such as SiO_2 have high melt viscosities and exhibit kinetically strong behavior upon undercooling. The melt viscosity of BMGs are typically on the order of 1

Pa s and they exhibit moderate fragilities near the glass transition, indicating that the kinetics of these undercooled liquids are sluggish compared to simple metallic liquids. Similarly, kinetically strong glasses exhibit shallower heat capacity curves compared to fragile glasses, thereby showing that the kinetic and thermodynamic considerations for GFA are well correlated.

2.4 Microstructure

Metallic glasses have complex disordered microstructures that set them apart from network glass formers. Lacking long-range order, these alloys only exhibit topological and chemical order on short-to-medium range length scales. Short range ordering (SRO) is found on the length scale of the nearest neighbor atoms, while medium range order (MRO) extends beyond the nearest neighbor shell. Early work by Bernal [14] used the dense random packing of hard spheres to describe the topological ordering of glasses. However, random packing has been shown to be inefficient for multicomponent systems with atomic size mismatches [140, 141]. Miracle refined this topological description of metallic glasses by including a description for ordering beyond the nearest neighbor shell, resulting in the so called dense efficient packing model. In this model, ordering on short length scales is defined through solute centered clusters. Ordering on medium range is defined through the arrangement of these clusters on a fcc or hcp lattice as shown in figure 2.12. One weakness of the efficient packing model is that it does not account for chemical contributions to the

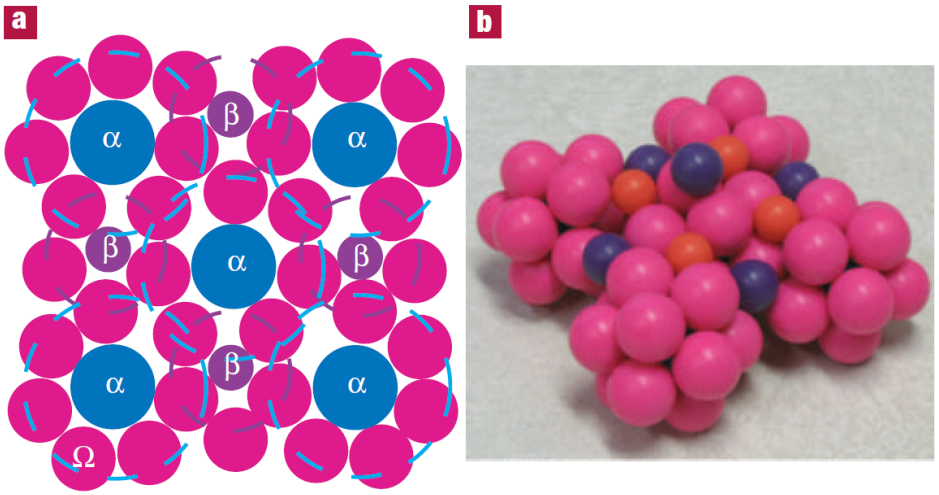

Figure 2.12: Two illustrations of partial unit cells according to Miracle's efficient cluster packing model.(a) a two-dimensional section through the (1 0 0) plane of the unit cell showing the inter-penetration of solvent (Ω) clusters that are centered around the solute (α and β) atoms. (b) is a three dimensional representation of a Zr-(Al, Ti)-(Cu, Ni)-Be alloy according to efficient packing model. Adapted from [140].

stability of an amorphous alloy. For example, solutes which are topologically similar but have different enthalpies of mixing will lead to different behavior and structures [140]. Despite this drawback, however, the model accurately describes the first coordination shell of a solvent-centered clusters in select binary metallic glasses, adequately describing medium range order within ≤ 1.0 nm.

2.5 Mechanical properties

By virtue of their densely packed aperiodic structure, metallic glasses have exceptional properties, making them attractive candidates for a variety of engineering applications. Compared to crystalline alloys, they exhibit relatively high yield strengths (the highest reported exceeding 5 Gpa for Co-Fe alloys) and elastic strains up to 2% [164]. Their high resilience per unit volume $\sigma_y^2/E\rho$ and low mechanical damping reflects an extraordinary ability to store elastic energy (Figure 2.13), making them ideal spring materials. Additionally, the absence of a grain structure and lack of abrupt shrinkage on solidification make it possible to reproduce of near-atomic scale features. Similarly, they not as susceptible to corrosion that might otherwise occur preferentially along microstructural features such as grain boundaries [124].

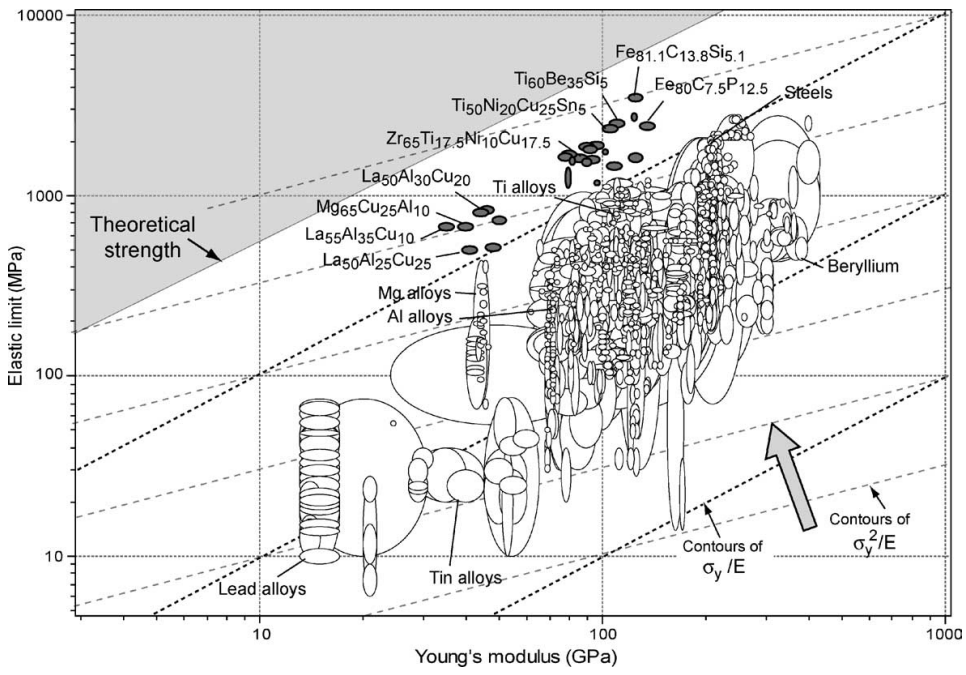

Figure 2.13: Ashby property map comparing the yield strength σ_y and Young's modulus E of a variety of engineering materials. Additional contours show the resilience σ_y^2/E and yield strain σ_y/E. Adapted from [9].

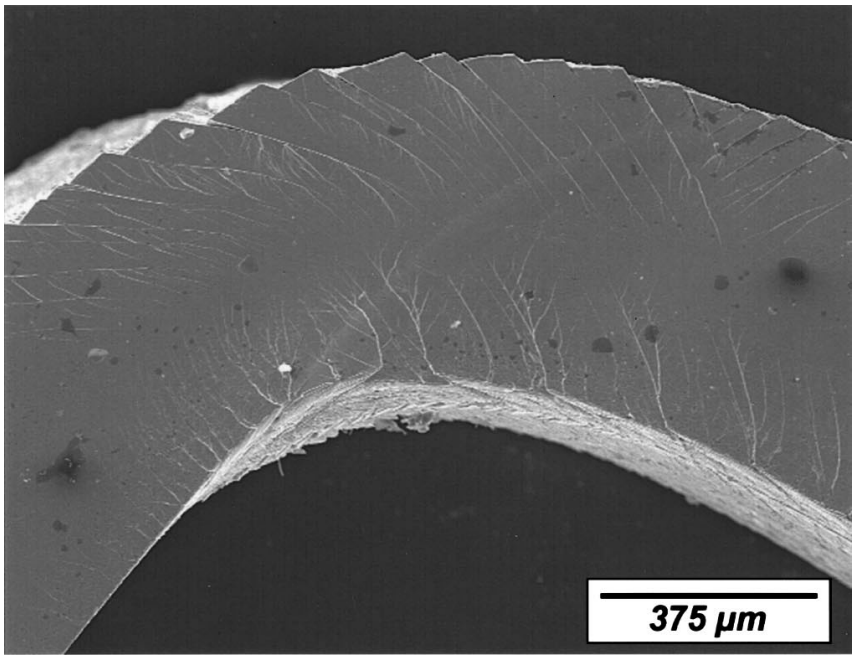

Figure 2.14: Scanning electron microscope micrograph showing shear banding in a melt spun ribbon of Vitreloy 106 that was bent over a 1 mm mandrell. Figure adapted from [88].

Metallic glasses have a wide range of fracture toughnesses but typically possess very limited tensile ductility. In crystalline materials, work hardening distributes strains throughout the material during plastic deformation. However, this mechanism is not present in metallic glasses. Instead, these strains are concentrated in highly localized shear displacement events or *shear bands* (Figure 2.14), where a planar volume of atoms is sheared in a process similar to mode II fracture, with the distinction that cohesion is maintained between the two halves. The propagation of shear bands can proceed uninhibited because metallic glasses lack the microstructural features that would otherwise resist plastic flow. This limits the application of metallic glasses for structural applications because of their tendency to fail catastrophically.

Although the exact mechanism of the deformation of metallic glasses is not yet completely understood, it is generally accepted that shear strains must involve the rearrangement of atoms locally. Argon used the distortion of two-dimensional rafts of bubbles under shear stresses as an analogy to the local redistribution of flow stresses among clusters of atoms in metallic glasses [7, 8] (Figure 2.15a). These deformed regions are now commonly referred to as a *shear transformation zones* (STZ). The atoms involved in an STZ undergo a thermally activated inelastic transition between two low energy configurations. Despite their close resemblance to the nucleation of dislocation loops, STZs are transient events rather than defects in the glassy structure [7]. Concurrently, Spaepen used Turnbull's free volume model to explain the flow in metallic

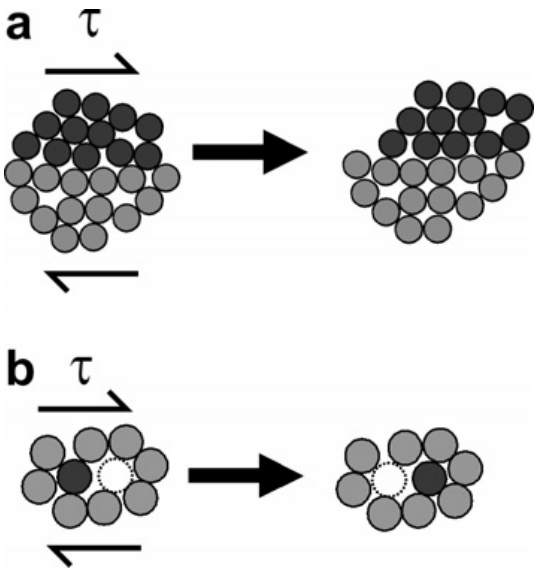

Figure 2.15: Illustration of the two mechanisms used to describe inelastic deformation in metallic glasses, (a) Argon's shear transformation zones [8] and (b) Spaepen's local diffusive jump into an area of higher free volume [157]. Figure adapted from [45].

glasses in terms of local atomic diffusion [157] (Figure 2.15b). In this model, atoms are redistributed via discrete atomic jumps into areas of high free volume in a manner similar to vacancy diffusion in crystalline solids. In both cases, the local rearrangement of atoms requires higher energies compared to conventional deformation mechanisms such as the gliding of dislocations in crystalline metals.

Depending on the temperature and strain rate, plastic flow in metallic glasses will be distributed either homogeneously or heterogeneously. At low temperatures shear localization is preferred. Meanwhile, at higher temperatures the material will deform homogeneously in manner that is typically described as the viscous flow of a supercooled liquid. Furthermore, steady-state flow conditions are stress- or strain-rate sensitive. For low stresses, STZ or diffusive motion is balanced alongside structural relaxation. The superposition of these events under steady-state conditions can be approximated as the Newtonian flow of an energetically activated volume of atoms. Increasing the stress causes distinctly non-Newtonian behavior [45]. This behavior is summarized in a stress and strain rate deformation map shown in figure 2.16.

The fact that glasses can be deformed homogeneously at low shear rates near T_g in the supercooled liquid state has far-reaching implications on the processability of these systems. Unlike their crystalline counterparts, metallic glasses are capable of near-net-shape formability within the supercooled liquid state, a process which which is called *thermo-plastic forming* (TPF). In

typical TPF processes, the glassy sample is heated into the supercooled liquid region (SCLR), between the glass transition temperature T_g and the onset of crystallization T_x. As the material is heated above the glass transition, it softens drastically ($10^9 \leq \eta 10^12$ Pa s) and can be deformed with relative ease. Additionally, the processing window is confined to times before the onset crystallization, which can be quantitatively described with the use of isothermal TTT diagrams. Alloys with large supercooled liquid regions are ideal candidates for TPF processing [152, 153]. Although more fragile glasses show drastically reduced viscosities with slight increases in temperature, they are also more likely to crystallize upon reheating. Therefore, there is little correlation between TPF formability and fragility.

Consequently, BMGs can be processed with techniques similar to those used in conventional plastics, opening up a multitude of geometries. Some examples of such techniques that have been successfully applied to BMGs include blow molding [73], extrusion [61, 133], injection molding [43], and replication of nano-scale features through imprinting [75]. Similarly, TPF can be used to create atomically smooth surfaces, whereby the smoothing process is driven by surface tension and the size of surface features are only limited by the presence of surface contaminants [57, 58, 75].

Accordingly, Schroers and coworkers have characterized the formability of various alloys within the supercooled liquid region. The best correlation, as expected, came from the size of the supercooled liquid region. Additionally, the kinetic fragility and Poisson ratio were found to correlate to the formability [153]. While kinetically fragile glasses exhibit more rapidly decreasing viscosities at higher temperatures, they are generally more readily crystallized upon reheating.

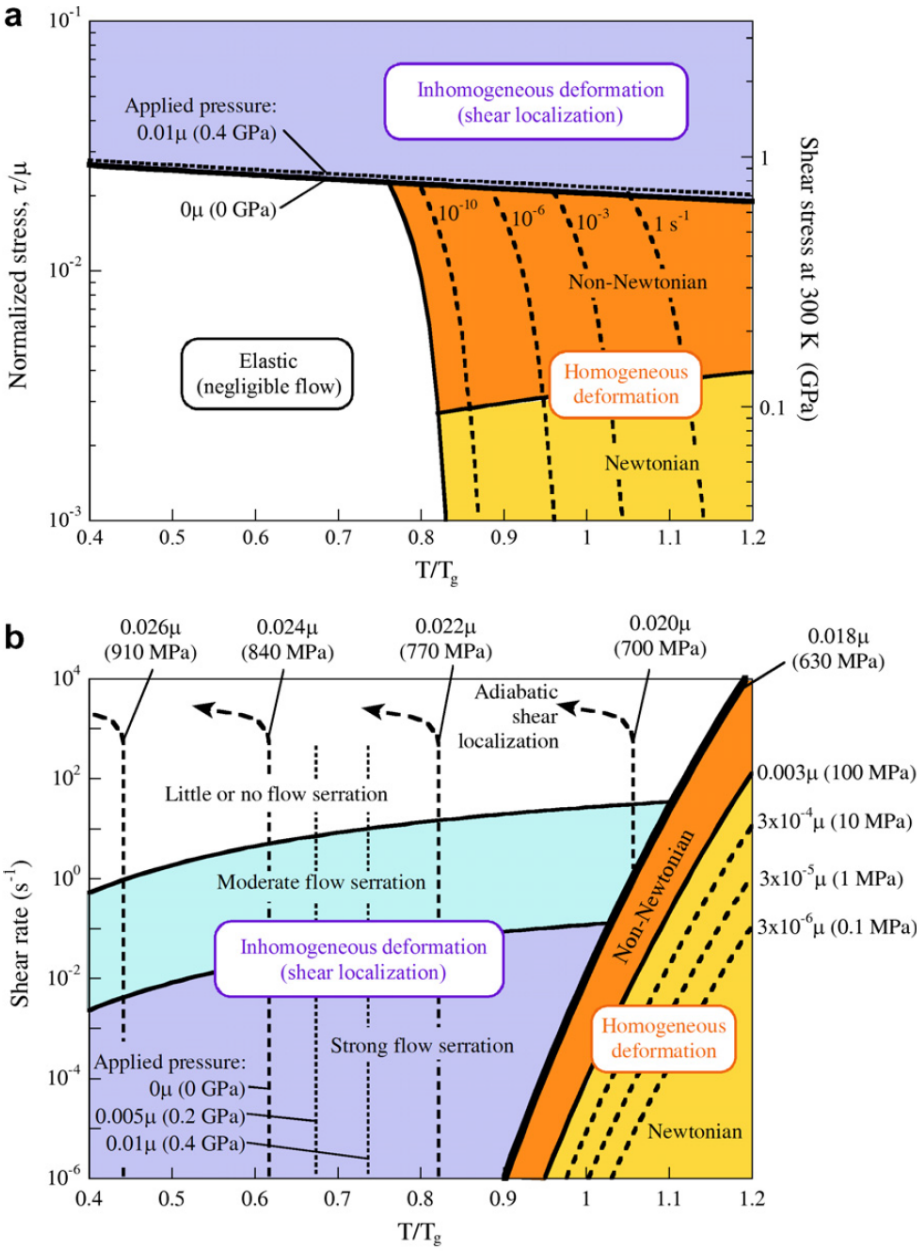

Figure 2.16: Deformation map for varying (a) stress- and (b) strain-rates versus temperature. Contours show the homogeneous and inhomogeneous deformation regimes as well as transitions between Newtonian-Non-Newtonian flow behavior. Specific values for stress are shown for Vit1. Figure adapted from [45].

2.6 The Strong-Fragile transition

For a variety of glass forming systems, there is a growing body of evidence for the existence of dynamic crossovers between thermodynamically and kinetically distinct liquid phases. These *liquid-liquid transitions* (LLTs) are often referred to as *polyamorphous* phase transitions, whereby a system can transform between different amorphous phases with identical chemical compositions, which is analogous to polymorphism in crystalline materials. Recent experimental and computational investigations suggest the existence of LLTs for water [6, 46, 85], Y_2O_3-Al_2O_3 [59], SiO_2 [86], BeF_2 [91, 162], Ce-Al [62], and in a number of metallic glasses [47, 49, 50, 62, 87, 92, 101]. While LLTs in inorganic and molecular glass formers are usually attributed to changes in the local chemical environment, the lack of directional bonding in metallic glass forming systems raises further questions about the mechanisms of polyamorphism.

Although the exact nature of polyamorphism remains ambiguous, measurements and simulations of the structure and thermodynamic properties provide valuable insight into the underlying mechanisms and characteristics. These transitions are associated with a continuous change in the thermodynamic properties of the liquid, which is signified by an endothermic heat capacity peak on undercooling. Concomitantly, the relaxation behavior undergoes a change from fragile behavior at high temperatures to strong behavior at low temperatures.

Perhaps the most widely studied and debated case of polyamorphism is in that of liquid water. In 1985, Mishima and coworkers [85] first discovered the pressure induced transition between high- and low-density amorphous water at ambient temperatures using in-situ X-ray diffraction experiments. The high-density liquid (HDL) phase was formed by compressing the samples at 77 K to 16 kbar and subsequent decompression to zero pressure showed an abrupt 22% volume change at approximately 6 kbar, resulting in the low-density liquid (LDL) phase. Ito and coworkers [6, 76] investigated the excess entropy associated with this anomaly and found that water behaves as a strong liquid in the low temperature regime and at high temperatures it is extremely fragile.

Phenomenologically, polyamorphism is often explained by the presence of a liquid-liquid critical point where two compositionally identical phases coincide. This can be represented on a Pressure-Temperature (P-T) phase diagram with the *Widom line*, which is defined as the locus of maxima of the thermodynamic response functions (e.g. isobaric heat capacity). The Widom line is found by extrapolating the coexistence line from the two-phase region into the single-phase region. When crossing this line, the system undergoes drastic yet continuous changes in the thermodynamic properties. In the case of water, the critical point and the Widom line separate the HDL and LDL

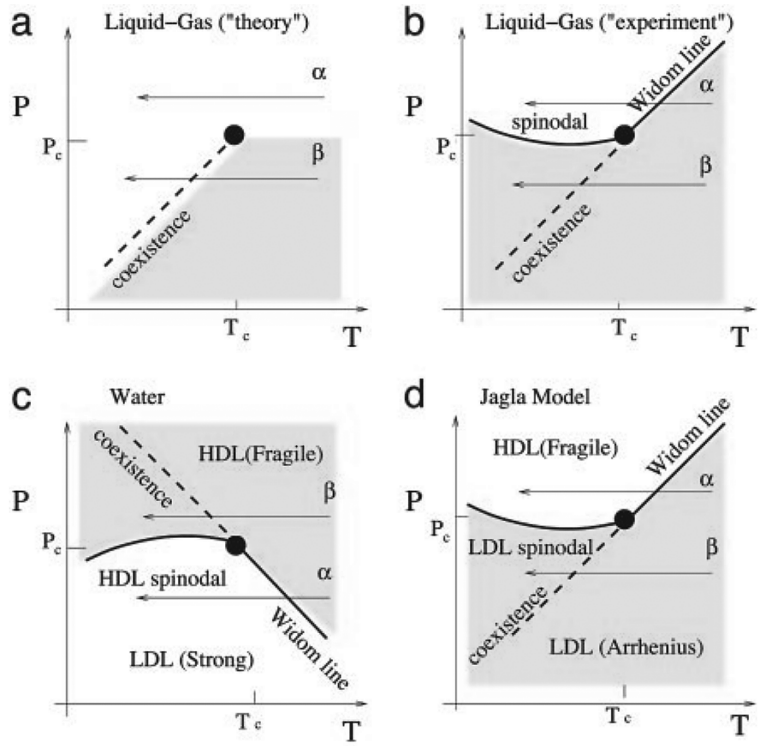

Figure 2.17: Schematic pressure-temperature phase diagram that illustrates four distinct phase transitions and the associated critical points (filled circles). (a) shows a predicted first-order liquid-gas transition, (b) shows the same situation but for a system that can remain in a supercooled metstable state until reaching a spinodal limit, (c) shows the hypothetical case for confined water with a negatively sloped liquid-liquid coexistence line and similarly extrapolated Widom line, and (d) shows the phase diagram of a liquid simulated with the two-state Jagla model. Figure adapted from [80].

phases as shown in figure 2.17 [80].

In many systems, however, experimental detection of the critical point is hindered by the limitations of undercooling and the onset of crystallization. For this reason, molecular dynamics simulations are invaluable for exploring the dynamics of very deeply supercooled (or superheated) liquids. One method is the Jagla model, where particle interactions within the liquid are based on a spherically symmetric two-scale potential that includes attractive and repulsive ramps as well as hard cores [126]. By tuning the parameters of the interaction potentials (e.g. ramp length ratios), anomalies like those observed in supercooled water can be readily simulated (see figure 2.17d) [80, 81, 112].

Recent work has shown that one of the salient features of liquid-liquid transitions is the discrepancy between the high and low temperature kinetic fragilities. For archetypal strong or fragile liquids, this crossover occurs at

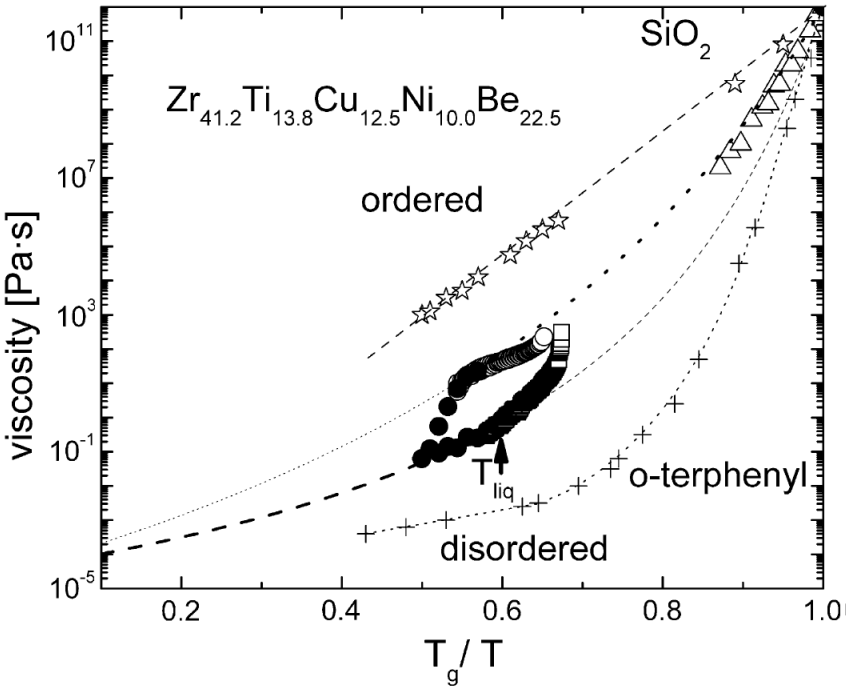

Figure 2.18: Angell plot showing the Strong-Fragile transition that was observed in Vit1 using Couette viscosity measurements. Included are isothermal measurements (solid circles) as well as continuous cooling experiments at 2 K s^{-1} from 1125 K (open circles) and from 1225 K (open squares). Figure from [47].

very high or low temperatures, respectively, and is obscured for conventional measurements. However, liquids with intermediate kinetic fragilities, such as metallic glasses, have been shown to display clear evidence for LLTs based on the fragile high temperature behavior and strong low temperature behavior. Particularly, in the case of $Zr_{41.2}Ti_{13.8}Cu_{12.5}Ni_{10.0}Be_{22.5}$ (Vit 1), Busch and coworkers [47] directly observed a crossover from a strong liquid to a fragile liquid above 1225 K as shown in figure 2.18. Upon subsequent cooling, the liquid remained in the fragile state until crystallization. The fragility parameter of the strong liquid were reported as $D^* = 26.5$ while the fragile liquid were reported as $D^* = 12$. Furthermore, the kinetically strong liquid showed shear thinning behavior which disappeared once the fragile liquid phase was reached. The strong liquid behavior and shear thinning was attributed to the presence and subsequent destruction of order within the melt [47, 48, 101].

In 2013, Wei and coworkers [92] investigated the calorimetric and structural anomalies associated with the S-F transition in Vit 1 using in-situ high-energy synchrotron X-ray diffraction experiments in an electrostatic levitation furnace (ESL). Containerless processing in the ESL enabled recording of diffraction intensity patterns upon undercooling from the equilibrium melt at > 1300 K down to vitrification below < 700 K. The total structure factor S(Q) was

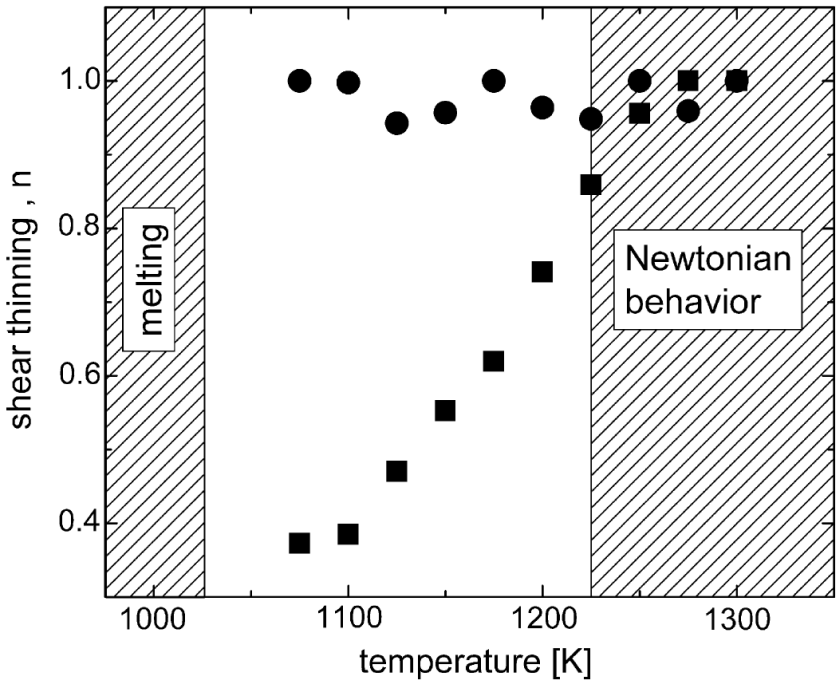

Figure 2.19: Plot showing the change in shear thinning exponent for Vitreloy 1. Solid squares correspond to the strong liquid that exhibited pronounced shear thinning ($n < 1$), while solid circles correspond to the fragile liquid obtained after heating to > 1225 K that showed Newtonian behavior ($n = 1$). Figure from [47].

extracted from the diffraction data and changes in the first peak position Q_1 were investigated in detail. In real space, Q_1 corresponds to the medium-range order in the liquid. A clear discontinuity in the volume changes (given by $1/Q_1^3$) was observed at 830 K which could not be attributed to the glass transition. Additionally, this structural change coincided with an exothermic heat capacity anomaly obtained from the measurements of hemispherical total emissivity (c_p/ϵ) of Ohsaka and coworkers [78]. Previous structural investigations by Rhim and coworkers mistakenly associated the shifts in S(Q) from crystallization with the hysteresis of the strong-fragile transition [79]. In contrast, the work of Wei et al. were able to ruled out crystallization due to the lack of Bragg peaks and from estimation of the changes of volume according to the rule of mixing. Reheating the sample resulted in crystallization and eventual melting, whereupon Q_1 returned to the behavior seen previously above $>$ 1300 K that was associated with the fragile liquid. Additionally, the full-width at half-maximum (FWHM) of Q_1 displayed a temperature dependent hysteresis, suggesting that some structural reconfiguration to a more disordered state occurs at high temperatures. This work together with the previous investigations of Busch and coworkers strongly suggest that Vit1 exhibits a strong-fragile transition.

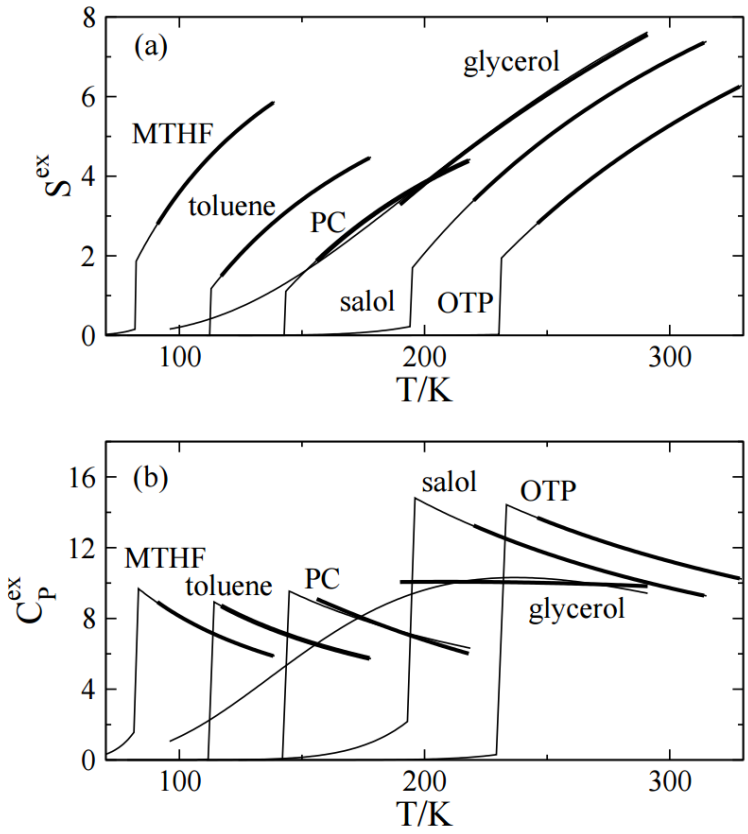

Figure 2.20: Excess entropy (a) and excess heat capacity (b) for various fragile glass forming liquids, showing both experimental data from [142] as thick lines and simulated data predicting a 1st-order transition below the glass transition temperatures. The units in k_B are given per molecule. Figure from [137].

Similar heat capacity anomalies are reported for archetypal strong liquids such as SiO_2 [86, 156] and BeF_2 [82, 91] at high temperatures [5]. Molecular dynamics simulations have shown that SiO_2 undergoes a transition to fragile behavior above 3300 K [66, 68]. Likewise, Hemmati and coworkers [82] simulated a heat capacity peak above T_m in BeF_2. Meanwhile, liquids that are canonically fragile molecular glass formers such as toluene, glycerol, and o-terphenyl have been shown to exhibit an apparently first order transition below T_g [137].

The heat capacity signatures and associated entropy fluctuations at the LLT in various glass forming liquids are summarized in Angell's "big picture" (see figure 2.21). On the one extreme, there are liquids that remain fragile across a wide range of temperatures and the LLT is expected to manifest as a first order transition below T_g. On the other extreme, archetypal strong liquids such as SiO_2 are expected to transition to a fragile state well above their melting point. In between these two extremes there are systems that exhibit

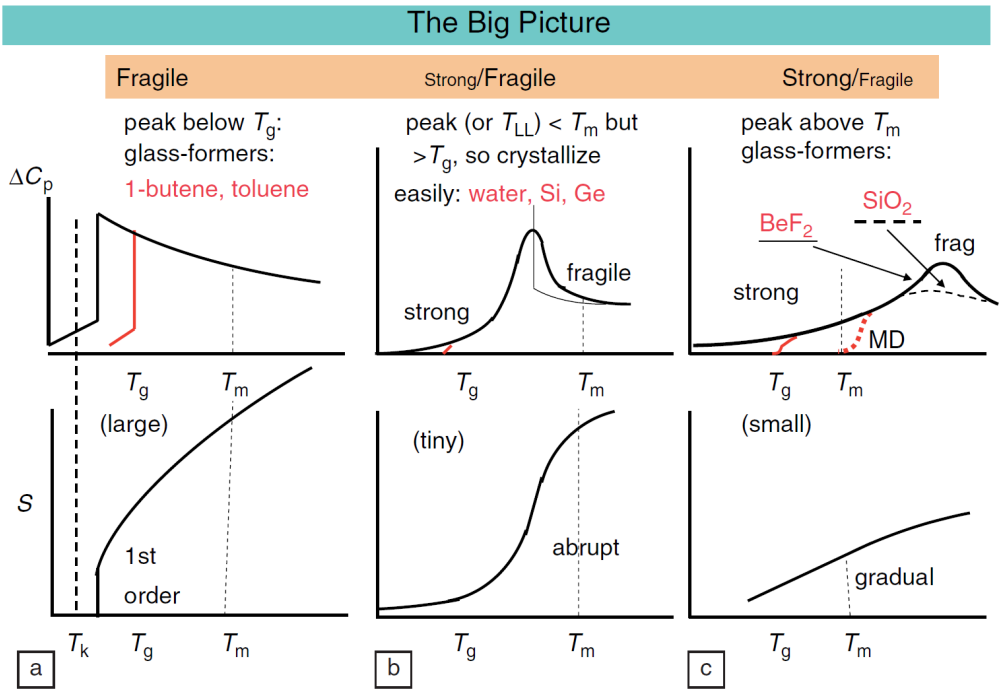

Figure 2.21: Angell's big picture of glass-forming liquids, showing the heat capacity jumps and entropy fluctuations associated with a liquid-liquid transition for (a) canonically fragile molecular glass formers that have a LLT manifesting as a 1st order transition below T_g, (b) glass formers that readily crystallize and have a LLT between T_g and T_m, and (c) archetypal strong glass-formers such as SiO_2 that have a LLT above T_m. For both (b) and (c), the liquid is kinetically strong at low temperatures and fragile above the LLT. Figure from [6].

strong behavior near T_g and fragile behavior near T_m and the LLT anomaly manifests within intermediate temperature ranges. Within this scheme, Angell hypothesizes that LLTs are universal features of glass forming liquids. Experimentally, however, it is difficult to observe the extreme cases where the transition occurs either far below T_g or above T_m. Compared to the two extremes, glasses that fall into the intermediate case allow for easier experimental access to LLTs, therefore making them prime candidates for investigations of these phenomena. Some examples of systems belonging to this group include water, Si, Ge, and metallic glass forming liquids.

Chapter 3

The Couette rheometer

The primary focus of this work was the redesign and reconstruction of a concentric cylinder rheometer with the capability to measure molten BMG alloys. The original instrument was constructed at Oregon State University by Tyler Shaw and Chris Way and was brought to Saarland University. Due to technical issues, however, the rheometer was decommissioned and the plans for reconstruction were set into motion. This chapter will first outline the theoretical framework for concentric cylinder rheometry and then give a comprehensive overview of the engineering design of the apparatus.

3.1 Rheology and Couette Flow

Rheology is the branch of natural sciences that is concerned with the deformation and flow of materials. In the presence of external perturbations, a continuous media of finite size will have some inner reaction that can be related to the inherent properties of the material with the help of the appropriate equations of solid state continuum and fluid dynamics. By treating a material as a continuum, body geometry can be neglected and the rheological properties determined according to a point of reference with appropriate models. The classical Hookean and Newtonian models provide the simplest descriptions of the flow of ideal elastic solids and ideal liquids, respectively. As this work is principally concerned with the flow of liquids, the latter model will serve as a starting point for the theoretical description of viscosity and flow.

Viscosity was first described by Isaac Newton as a fluid's resistance to displacement that is proportional to the velocity gradient [144]. This can be expressed in its one dimensional form as

$$\tau_{yx} = \eta \frac{dv_x}{dy} \tag{3.1}$$

where τ_{yx} is the shear stress, η is the shear viscosity, and $\frac{dv_x}{dy}$ is the velocity gradient in one dimension. Note that the absolute velocity is unimportant, since the viscosity is concerned strictly with the relative rate of separation between two points in the liquid.

One useful visualization for this is the flow of liquid between two parallel plates, where one plate is held fixed and the other moves at a constant velocity. For laminar flow with perfect adhesion at the interface between the plate and liquid (i.e. no wall slippage), the viscous stress is directly proportional to the shear rate in accordance to equation 3.1. George Stokes and Claude-Louis Navier both expanded upon Newton's simple expression by applying the principles of conservation of mass, momentum, and energy. The resulting three dimensional equations of motion are known as the Navier-Stokes equations. The derivation of the equations of motion can be found in any fluid dynamics textbook [135] and are included for reference in appendix A.1.

In 1890 Maurice Couette demonstrated the validity of equation 3.1 by measuring the viscous stresses arising from confined flow between coaxial cylinders [74]. In the original device, the liquid was sheared between a rotating outer cylinder and a stationary inner cylinder that was suspended from a torsion wire. By recording the angular deflection of the torsion wire, the reaction force imparted on the stator could be determined and related to the viscous stresses in the liquid. Due to its relative simplicity, the working principles of Couette's apparatus remain largely unchanged in modern instruments, including the device used in the present study.

The working equations for Couette rheometry are derived from the Navier-Stokes equations under specified boundary conditions and assumptions. First and foremost, the system is assumed to have reached steady state and flowing in a laminar manner. Only circumferential flow, v_θ, is considered and the radial and axial velocity components are assumed to be zero, $v_r = v_z = 0$. Additionally, body forces (gravity), convection, and end effects are ignored. The system is assumed to have angular symmetry, such that $\partial/\partial\theta = 0$.

As a result of these assumptions, the equations of motion in cylindrical coordinates simplify to [21, 113, 135, 138, 179]:

r-component:

$$-\rho\frac{v_\theta^2}{r} = \frac{1}{r}\frac{\partial\left(r\sigma_{rr}\right)}{\partial r} - \frac{\sigma_{\theta\theta}}{r} \tag{3.2}$$

θ-component:

$$0 = \frac{\partial\left(r^2\tau_{r\theta}\right)}{\partial r} \tag{3.3}$$

z-component:

$$0 = -\frac{\partial p}{\partial z} + \rho g_z \tag{3.4}$$

where equation 3.2 accounts for the normal stresses acting on the fluid, equation 3.3 describes the shear stresses acting on the fluid which arise from the relative motion of the inner and outer walls, and equation 3.2 simply describes the hydrostatic pressure within the shear cell at any depth. Normal stresses are responsible for some important end effects, such as pressure gradients from centrifugal forces that may result in either rod climb or depressions in the surface of the liquid. Note that the z axis is oriented vertically for practical reasons, since the outer cylinder is often a cup that must contain the liquid.

Equation 3.3 is of particular importance to Couette rheometry with the definition of further boundary conditions according to the assumption of perfect slip at the walls. If the inner cylinder rotates at an angular velocity ω_i and the outer cylinder is stationary ($\omega_o = 0$), then the boundary conditions for perfect stick conditions at the inner wall ($r = R_i$) and outer wall ($r = R_o$) are

$$v_\theta(r) = \begin{cases} \omega_i R_i & \text{at } r = R_i \\ 0 & \text{at } r = R_o \end{cases} \tag{3.5}$$

Integration of equation 3.3 yields the shear distribution within the annulus of the rheometer,

$$\int \frac{\partial \left(r^2 \tau_{r\theta}\right)}{\partial r} \rightarrow \tau_{\theta r} = \frac{c_1}{r^2} \tag{3.6}$$

where c_1 is an integration constant. The integration constant can be resolved through the balance of forces, yielding the general expression for shear stress within the gap

$$\tau_{\theta r}(r) = \frac{M_r}{2\pi L r^2} \tag{3.7}$$

where L is the axial length of the surface being sheared (i.e. immersion length) and M_r is the reaction torque measured at either R_i or R_o. To relate the shear stress to the viscosity, the distribution of shear rates within the gap must be described. In its simplest form, the shear rate as a function of radius is given by

$$\dot{\gamma}(r) = \frac{1}{r^2} \frac{(2R_i^2 R_o^2)}{(R_o^2 - R_i^2)} \omega \tag{3.8}$$

The viscosity of a liquid is given by the ratio of shear stress to shear rate, or $\eta = \tau_{\theta r}(r)/\dot{\gamma}(r)$. For a system with a rotating inner cylinder, it is conventional to relate the shear stress and rates at $r = R_i$, leading to [135]

$$\eta = \frac{\tau_{\theta r}(R_i)}{\dot{\gamma}(R_i)} = \frac{(R_o^2 - R_i^2)}{4\pi L R_o^2 R_i^2} \frac{M}{\omega_i} \tag{3.9}$$

Wide gap shear cells

When the annulus gap is very large ($k = R_i/R_o < 0.1$) then equation 3.9 breaks down and the difference in shear rate at the walls can no longer be neglected. It must be either directly measured or defined as a function of the shear stresses. Accordingly, the first step is to define the derivative shear rate in cylindrical coordinates,

$$\dot{\gamma} = \frac{\partial v_\theta}{\partial r} - \frac{v_\theta}{r} = r\frac{\partial}{\partial r}\left(\frac{v_\theta}{r}\right) = r\frac{\partial \omega}{\partial r} \tag{3.10}$$

This can be expanded the help of equation 3.6 to define the shear rate a function of the circumferential shear stress $\tau_{r\theta}$

$$\dot{\gamma}(r) = \left| r\frac{\partial \omega}{\partial r} \right| = 2\tau_{r\theta}\frac{d\omega}{d\tau_{r\theta}} \tag{3.11}$$

For a system whose stator is the outer cylinder and rotor is the inner cylinder, this equation can be integrated with respect to the angular velocity

$$\int_0^{\omega_i} d\omega = \omega_i = \int_{\tau_{R_o}}^{\tau_{R_i}} \frac{\dot{\gamma}(\tau)}{2\tau} d\tau \tag{3.12}$$

Differentiating the results with respect to the shear stress at the rotor, τ_{R_i} yields

$$\frac{d\omega_i}{d\tau_{R_i}} = \frac{1}{2}\left[\frac{\dot{\gamma}(\tau_{R_i})}{\tau_{R_i}} - \frac{\dot{\gamma}(\tau_{R_o})}{\tau_{R_o}}\frac{d\tau_{R_o}}{d\tau_{R_i}}\right] \tag{3.13}$$

from equation 3.7, one can define the following

$$\frac{d\tau_{R_o}}{d\tau_{R_i}} = \left(\frac{R_i}{R_o}\right)^2 \tag{3.14}$$

Substituting this into the previous expression gives

$$2\tau_{R_i}\frac{d\omega_i}{d\tau_{R_i}} = \dot{\gamma}(\tau_{R_i}) - \dot{\gamma}(\tau_{R_o}) \tag{3.15}$$

for wide gaps, where $k < 0.1$, then $\dot{\gamma}(\tau_{R_o}) << \dot{\gamma}(\tau_{R_i})$ and equation 3.15 simplifies to

$$2\tau_{R_i}\frac{d\omega_i}{d\tau_{R_i}} \cong \dot{\gamma}(\tau_{R_i}) \tag{3.16}$$

or

$$\dot{\gamma}_{R_i} \cong 2\omega_i\frac{d\ln\omega_i}{d\ln M_i} \tag{3.17}$$

In addition to determining the shear rate for wide gap shear cells, equation 3.17 can also be used for concentric cylinder rheometers with heterogeneous geometries (e.g. vaned rotors), where the position dependent velocity is difficult to measure directly [135, 138].

Power law fluids

Yet another complication arises when measuring non-Newtonian fluids, where the viscous response is shear rate dependent. For all intents and purposes, the derivation of the shear rate is analogous to that for a wide gap shear cell, where the shear rate is allowed to vary across the annulus. A Taylor series expansion of equation 3.15 gives [135]:

$$\dot{\gamma}(\tau_{R_i}) = -\frac{\omega_i}{\ln k}\left[1 - \frac{1}{n}\ln k + \left(\frac{1}{n}\ln k\right)^{2/3} - \left(\frac{1}{n}\ln k\right)^{4/45}\ldots\right] \tag{3.18}$$

where n is the power law index, which can in turn be expressed as

$$n = \frac{d\ln M_i}{d\ln\omega_i} \tag{3.19}$$

For intermediate gap sizes, where $0.5 < k < 1.0$, then n is approximately constant between R_o and R_i and equation 3.15 can be rewritten as

$$\dot{\gamma}_{R_i} = \frac{2\omega_i}{n\left(1 - k^{2/n}\right)} \tag{3.20}$$

and

$$\dot{\gamma}_{R_o} = \frac{-2\omega_i}{n\left(1 - k^{-2/n}\right)} \tag{3.21}$$

The value of n can be determined through a linear regression of the stress response to the strain response, where n is the slope of the fit of $\ln M$ versus $\ln \omega$ [1]. $n = 1$ for Newtonian fluids, $n < 1$ for shear thinning fluids, and $n > 1$ for shear thickening fluids.

Shear thinning or pseudoplastic behavior is relatively common in dispersions or polymer systems that undergo some structural rearrangements upon agitation which promote flow [138]. In metallic systems, shear thinning has been reported in semi-solid alloys used typically for *rheocasting* applications [10]. Agitation of the liquid upon undercooling into the semi-solid state breaks down any dendrites into agglomerates of rounded spheroids. At rest, these spheroids agglomerate and the system behaves similarly to colloidal dispersions. Upon further shearing, the apparent viscosity of these systems exhibits pseudoplastic behavior due to deagglomeration of these particles.

Shear thickening or dilatant behavior is much less common since it is typically seen only in dispersions with a high solid concentration or extremely high shear rates. It has been suggested that dilatancy in non-aggregating monodisperse systems at high shear rates originates from a structural transition, where the particles switch from a layered arrangement of particles to a random packed structure that inhibits flow [13, 15]. This behavior is highly dependent on the volume fraction of the particles as well as their interaction forces, which in turn have both hydrodynamic and electrostatic contributions [15].

Representative viscosity calculations

If the gap between the inner and outer cylinders is narrow, then the effects of curvature can be neglected and the shear rate is assumed to be constant

[1] In the current system, one must be aware of some of the practical errors that may arise. Extremely low shear stresses will not be properly resolved by the sensor. Furthermore, at low shear rates the relative circumferential stabilization will be poor.

within the gap. In this case, the flow is identical to that of planar flow between parallel plates. This assumption is only valid when the ratio between the inner and outer radii is approximately equal to unity. Accordingly, DIN 53019 and ISO 3219 standards dictate a maximum ratio of $\delta_{cc} = R_o/R_i \leq 1.0847$ ($k > 0.9219$) for a system to follow the narrow gap assumptions [138].

Furthermore, DIN compliant shear cells must adhere to certain geometrical standards. First and foremost, the inner cylinder must have a tapered end whose interior apex has an angle of $\alpha = 120°$. Second, the length of the inner cylinder should be three times its radius, $L/R_i = 3$. Third, the distance between the bottom of the cylindrical section of the bob and lower surface of the cup should be approximately equal to the inner radius, $L'/R_i = 1$. Similarly, the bob should be fully immersed such that the distance between its top and the surface of the liquid should be equal to the inner radius, $L"/R_i = 1$. Finally, the radius of the bob shaft, R_s, is defined as $R_s/R_i = 0.3$ according to the DIN standards. ISO standards are slightly more flexible, allowing for longer bob cylinders, sharper angles of the taper, and more volume of liquid below the bob.

Another geometry that fulfills the DIN requirements is the so called *Mooney-Ewart conicylinder*, where the distance between the bottom of the bob and lower surface of the cup is shortened drastically such that the shear rate in the conical gap is equal to that between the cylindrical walls. To this end, the taper angle of the bob is defined as $\alpha = \left(\delta_{cc}^2 - 1\right) / \left(1 + \delta_{cc}^2\right)$. This geometry drastically reduces the volume of liquid necessary for a measurement. Along the same lines, Mooney-Ewart shear cells have no requirements for a specific filling height above the bob ($L"$). Unless significant climbing due to normal stresses or surface composition changes (i.e. slag formation) occur, the upper surface has a significantly smaller influence on the shear stress contributions to the measurements.

For all of the DIN shear cells, it is customary to determine the average or *representative* shear viscosity within the concentric annulus. In order to account for the shear stress contribution from the conical surface of the bob, an additional unit-less correction length term c_L is included in the calculation. With this correction length included, the representative shear stress in its expanded form is [138]:

$$\tau_{rep} = \left(\frac{1 + \delta_{cc}^2}{2\delta_{cc}^2}\right) \frac{M}{2\pi L R_i^2 c_L} \tag{3.22}$$

The correction length can be determined through calibration of the system with fluids of known rheological behavior, and is typically about $c_L = 1.10$ for

DIN geometries. Similarly, the representative shear rate in the gap is given by

$$\dot{\gamma}_{rep} = \left(\frac{1+\delta_{cc}^2}{\delta_{cc}^2-1}\right)\omega_i \tag{3.23}$$

By definition, the representative shear viscosity is given by

$$\eta_{rep} = \frac{\tau_{rep}}{\dot{\gamma}_{rep}} \tag{3.24}$$

3.1.1 Instabilities

The applicability of Couette rheometry and its governing equations are only suitable under the premise that all of the assumptions hold true. Upon their failure, analysis becomes significantly more difficult or is rendered impossible. In this section, the most common instabilities are described along with their consequences on viscosity measurements.

Secondary flow

When a liquid flowing past solid boundaries exceeds some critical limit it will develop eddying flow acting perpendicular to the axis of primary flow. The onset of these so called *secondary flow* instabilities are determined by the viscosity of the liquid and geometry of the system. In the case of Couette rheometry, these eddies are known as *Taylor vortices*, named after Sir Geoffrey Taylor, who was the first to systematically study this phenomenon using a custom built rheometer and water with colored dye [135].

These vortices dissipate energy in a manner analogous to Reynolds turbulence, where the inertia of the flowing liquid overcomes the internal forces. However, unlike pure turbulent effects, these vortices also arise from the centrifugal effects within the gap. In a Couette measurement system, the repercussions of this turbulence is an increase in the measured torque, leading to erroneously high apparent viscosities. Therefore, to ensure accurate rheological measurements, it is imperative to prevent the onset of Taylor secondary flow effects. For Newtonian fluids confined between a rotating inner cylinder and stationary outer cylinder, the conditions for stable flow are given by the Taylor number,

$$Ta = \frac{\rho^2 \omega_i^2 \left(R_o - R_i\right)^3 R_i}{\eta \left(\dot{\gamma}\right)^2} < 3400 \tag{3.25}$$

Non-Newtonian fluids tend to exhibit higher Taylor numbers. Therefore, the value above is usually taken as a conservative limit for most measurement systems. For any experiment, the maximum shear rate must first be determined based on the conditions for stable flow.

One can also determine the conditions for purely turbulent flow in a concentric cylinder rheometer, the criterion for which is based on the Reynolds number

$$Re = \frac{\omega_i \rho \left(R_o^2 - R_i^2\right)}{2\eta} \tag{3.26}$$

for $Re \geq 1$, instabilities at the upper and lower ends of the cylindrical section of the bob will arise (i.e. end effects). Under normal operating conditions, it is nearly impossible to prevent these end effects without specialized gasket rings. For $Re \geq 1000$, turbulence within the annulus will occur. Once again, angular velocities should be selected to minimize turbulence.

Alignment instabilities

Even for instruments built to very exacting tolerances, it is challenging to ensure perfect geometrical alignment and stability during real experiments, especially at high temperatures where components are subject to thermal expansion. Therefore, the acceptable limits of these instabilities along with their consequences on rheological measurements must be considered [21, 135, 138].

For Couette systems, one of the most problematic alignment instabilities occurs when the cylinders are no longer coaxial and rotate in an eccentric manner. Fortunately, this case of flow is relatively well understood and is applied in devices such as journal bearings. For a Newtonian fluid confined between parallel cylinders whose axes are offset by some eccentricity, ϵ, the distribution of pressure within the gap will result in a reaction force acting on the container walls, given by

$$F_\epsilon = \frac{12\pi\eta\omega_i L R_i^2 \alpha^2}{(R_o - R_i)^2 (1 + 2\alpha^2) (\alpha^2 - 1)^{1/2}} \tag{3.27}$$

where $\alpha = \frac{R_o - R_i}{\epsilon}$ is a unit-less parameter that accounts for the mean eccentricity in the gap. At high angular velocities the magnitude of this force increases, which has a tendency to reduce the eccentricity. If the eccentricity is allowed to decrease, then the increase in angular velocity results in the stabilization of the system and realignment of the axes until the bob axis is coincident with that of the cup.

More importantly, the eccentricity of the cylinders causes a reduction in the measured torque, which may in turn lead to an underestimation of the viscosity. For narrow gap geometries the reduction in torque is approximately

$$\frac{M}{M_o} = \frac{2\left(1 - \left[\epsilon/\overline{\Delta R}\right]^2\right)^{1/2}}{2 + \left(\epsilon/\overline{\Delta R}\right)^2} \tag{3.28}$$

where $\overline{\Delta R}$ is the average gap width and M_o is the torque measured for the same system without eccentricities. This effect should not be neglected, since the differences in torque can lead to significant errors in the viscosity calculations. However, due to the difficulties in measuring the actual eccentricity, it is probably simpler to take advantage of the self-stabilization at higher angular velocities to minimize the error in torque.

Shear heating

Due to the extreme sensitivity that viscosity has to slight changes in temperature, viscous dissipation of heat should not be neglected during an experiment. Indeed, the exchange of heat between a moving surface that is in contact with some fluid has wide ranging applications and is one of the key concepts necessary for developing a system that can measure the temperature dependent viscosity. There are two dimensionless quantities that allow direct insights into the viscous dissipation of energy, namely the *Prandtl* and *Eckert* numbers. The Prandtl number describes the ratio of viscous diffusion to thermal diffusion and is given by [135]:

$$Pr = \frac{c_p \eta}{k_T} \tag{3.29}$$

while the Eckert number characterizes the dissipation of kinetic energy within some flowing continuum

$$Ec = \frac{u^2}{c_p \Delta T} \tag{3.30}$$

where k_T is the thermal conductivity, u is the local velocity, and ΔT is the temperature difference between the moving wall and bulk of the fluid. The product of these two numbers produces a third dimensionless quantity known as the *Brinkman* number, which effectively describes the conduction of heat generated from viscous dissipation to the walls of a container,

$$Br = PrEc = \frac{u^2 \eta}{k_T \Delta T} \tag{3.31}$$

3.2 Reconstruction and redesign

After a multitude of technical issues culminating in the destruction of the torque sensor, the original Couette rheometer that was used by Chris Way to study Vitreloy 1 was decommissioned in 2010 and the current project was initiated. The refurbished rheometer was to be operationally similar to the original device while incorporating improvements both to the design and programming. Many of the programming changes have been covered in greater detail in reference [122] and will only be reviewed briefly along with the changes over the past five years. Instead, most of this section will be devoted to explaining the changes to critical components of the measurement system and will be broken down by component groups, starting from the overall structure, working down to the vacuum chamber, and finally taking a closer look at the shear cell itself. Figure 3.1 shows the Couette rheometer used in this study alongside the most critical subsystems.

3.2.1 Alignment system and frame

Perhaps the most obvious change that was made to the system was a complete overhaul of the chassis that supports the vacuum chamber. Originally, the

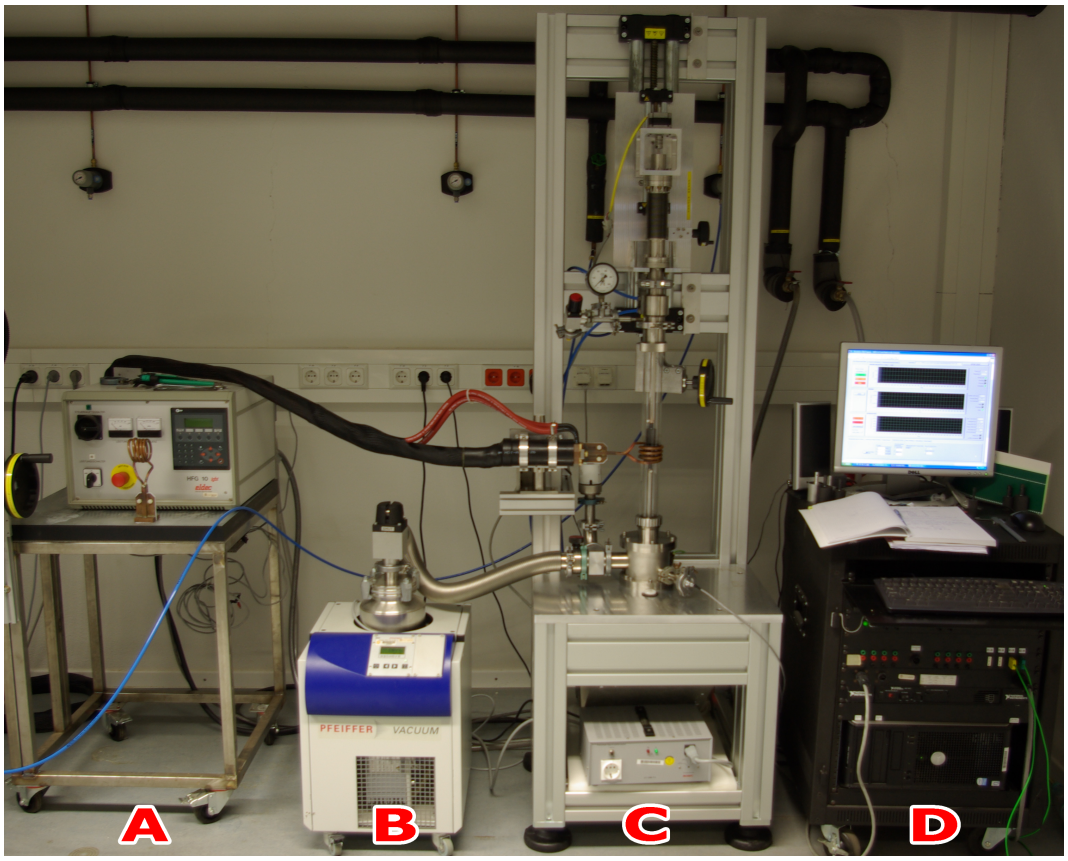

Figure 3.1: Photograph of the Couette rheometer and main subsystems where (A) is the high frequency inductive generator, (B) is the turbo-molecular pump, (C) is the rheometer, and (D) is the data acquisition computer.

main structural element of the viscometer was a massive steel pylon which was bolted to the floor and ceiling, creating a completely rigid frame. The recipient was suspended with the help of a rather complicated 3-axis gimbal, which was also intended to reposition and align the system. Although the design was well intended, the shortcomings of this ill-conceived structure caused more problems than it solved.

First of all, by affixing the entire apparatus to the building, any and all transient vibrations in the building were transmitted directly into the viscometer. This would not have been such a critical issue if some manner of dampening was applied, however, this was not the case. As a result, the measurement of low viscosity fluids (near the limit of the torque sensor) could be easily disturbed in the event of an unexpected tremor, including those caused by a door slamming shut.

Second, the 3-axis gimbal which was intended for accurate repositioning and alignment of the shear cell suffered from a number of design inconsistencies. Rather than rotating or translating with respect to a sensible coordinate

system, the pivots of the gimbal were arranged such that they not only provided redundant degrees of freedom but also caused unintended structural deflections upon actuation. For example, the system included a pair of coarse threaded adjustment screws mounted coaxially, which were intended to allow rotation of the viscometer from a horizontal axis. However, the adjustment of these screws caused additional flexure in the lever arm upon which the recipient was mounted due to the off-center location of the mounting axle. Nearly every gimbal axis suffered from similar design flaws. As a result, the proper alignment of the shear cell was incredibly difficult.

In order to solve these issues, a modular approach was taken in order to facilitate the relocation of the apparatus as well as provide a solid foundation for the recipient. Extruded aluminum beams with universal connectors were used to create the frame. The entire device is passively isolated from ambient vibrations using elastomer pads. The magnitude of instrumental vibrations is expected to be very low, because the primary source is from a small stepper motor which is used to rotate the bob of the device. Additional contributions may arise from the turbomolecular pump, however, a flexible stainless steel bellows connecting the recipient to the pump minimizes the direct transmission of vibrations.

Compared to the previously over-designed gimbal system, the current device employs a completely different adjustment philosophy. Rather than allowing for adjustment along excessive degrees of freedom, the location of the key components is instead fixed whenever possible while minor repositioning is allowed to account for machining tolerances. Horizontal repositioning of the recipient is facilitated by oversized slots in the aluminum mounting table. These slots allow 3 mm translation side-to-side and about 10 mm translation forwards-backwards. Meanwhile, the vertical position of the table is fixed to the frame and is not necessary to adjust once the device is fully assembled.

Positioning the bob (i.e. immersion) during an experiment and removing the glass tube after an experiment requires a stacked pair of translational manipulators. One is mounted directly to the aluminum frame and allows the entire motorized portion of the device to be raised or lowered by approximately 300 cm, giving ample clearance for installation and removal of the glass tube. The second translational manipulator is mounted on the motorized head of the device and is responsible for adjustment of the vertical position of the bob during an experiment. This manipulator allows for approximately 20 cm of vertical translation and includes a set screw for locking the position. Despite using new hardware, this vertical positioning system has conceptually remained largely unchanged with respect to the older model of the device.

3.2.2 Vacuum Chamber

Although not as readily apparent as the changes to the overall structure, the changes to and within the recipient are some of the most significant for the operation and stability of the system. The recipient consists of a lower, middle, and upper segment, each of which has a specific purpose. First, the lower segment houses the torque sensor as well as the electrical and vacuum inlets. Next, the middle segment is the glass tube which contains the shear cell. Finally, the upper segment acts as a feed-through for the rotating bob axle and inert gas inlet. The upper segment also includes a water cooled spindle bearing to promote the coaxial alignment of the bob during an experiment. Neither the middle nor the upper segments were modified in the current device. Most of the changes to the system were instead focused on the lower segment.

Originally, the lower segment of the recipient consisted of an 18 cm diameter 30 cm tall stainless steel tube with ISO-K (DIN 28404, ISO 1609) flanges on either end. Intersecting tubes with ISO-KF(DIN 28403, ISO 2961) flanges of various diameter acted as inlets for gas, thermocouples, and the torque sensor. Inside the chamber, the torque sensor was mounted on a platform, which was intended to allow fine tuning of the positioning of the cup while the recipient was open.

This system, unfortunately, was plagued by some major design oversights. Due to the location of the inlet for the vacuum pump relative to the positioning gimbal, the bending moment exhibited on the chamber from contraction of the vacuum bellows displaced and twisted the chamber, requiring additional repositioning and alignment after pumping. Unfortunately, any prior minor adjustments from within the chamber were rendered ineffectual due to the aforementioned displacement from the pump.

One of the main goals of the work leading up to this project was to minimize potential damage to the torque sensor from transverse loading of the cup axle [122]. This loading originated from eccentric motion of the bob as well as the misalignment after evacuating the chamber. To accomplish this, the sensor platform was replaced with a water cooled pillar mounted directly to the lower ISO-K flange of the recipient. This platform included a pair of ball bearings, which allowed for rotation of the axle but were intended to transfer the brunt of the transverse bending moment to the bearing housing rather than the sensor. Although this platform succeeded in protecting the sensor, the rolling friction of the bearings impeded the rotation of the axle, sacrificing measurement sensitivity considerably.

Unfortunately, the same mistake involving ball-bearings was made in the early stages of the new device. These bearings were later removed to improve sensitivity of the measurements but the bearing-housing remains intact as a

monument to the previous design oversight. The subsequent improvements to the coaxial alignment of the shear cells and overall reduction in the length of the lower axle have minimized transverse loading. However, there is still a large risk of damaging the torque sensor if the shear cell is loaded improperly.

The current lower segment was completely redesigned in order to resolve as many of these issues as possible, and is schematically represented in figure 3.2. The recipient is a 15 cm diameter 15 cm tall stainless steel tube. By having a smaller volume and smaller internal surface area, evacuation of the chamber is improved. Ample clearance is given for access to all of the internal components upon removal of the upper flange. Three ISO-KF flanges of varying diameter are distributed around the chamber to provide inlets for the vacuum pump, thermocouples, and the torque sensor. The largest of these three flanges is connected to the vacuum pump and is fitted with a quick release lock for easy access to the rigid coaxial couple between the torque sensor and the shear cell shaft. In lieu of large and bulky ISO-K flanges, the upper and lower flanges use custom designed o-ring seals and are precisely located with shear pins. Furthermore, the lower flange acts as a mount for the torque sensor. A CNC-milled pocket in the flange allows clearance for the moving components in the sensor. An open-loop water cooling system runs through this flange, cooling the sensor. This system runs in series with the cooling of the spindle bearing in the upper segment.

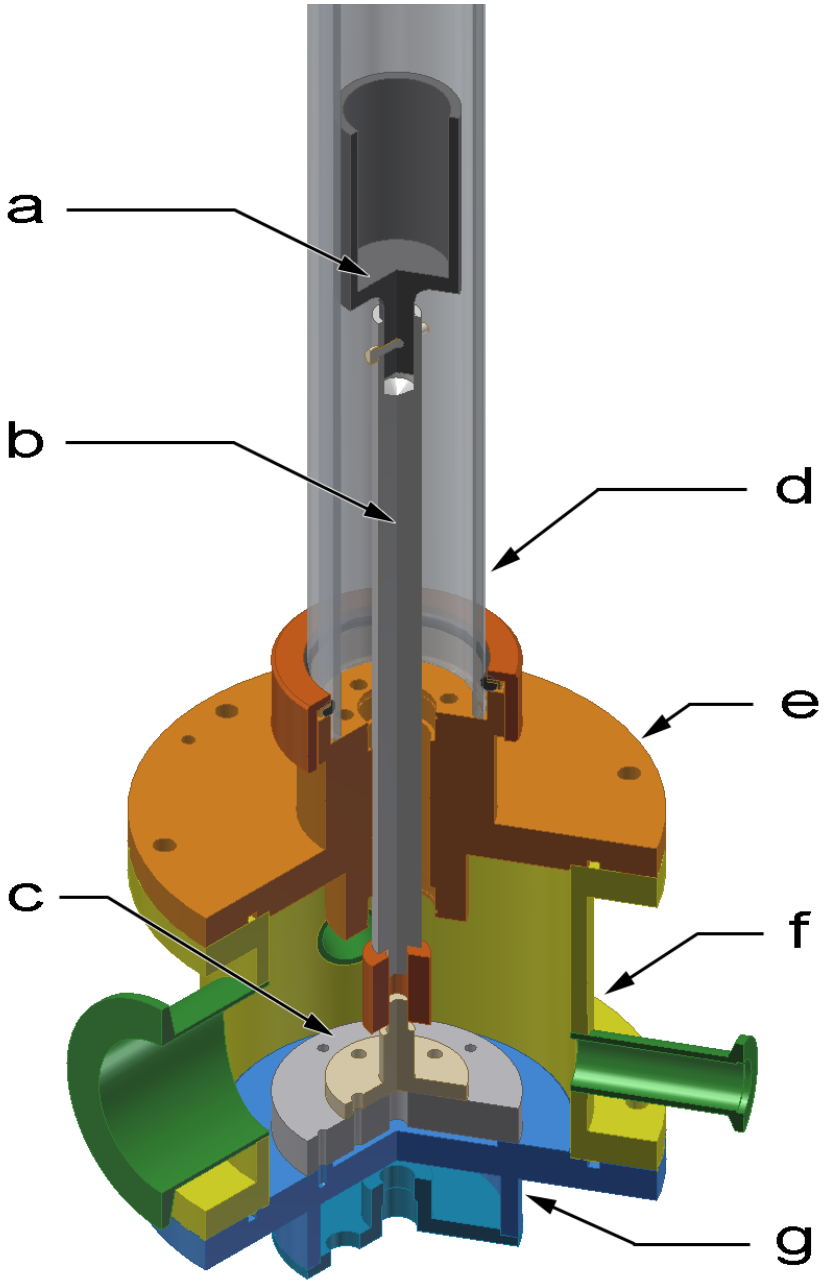

Figure 3.2: Cross section view of the lower vacuum chamber with the following parts labeled: (a) shear cell cup, (b) cup shaft, (c) torque sensor, (d) quartz glass tube, (e) upper recipient flange and glass seal, (f) main recipient and inlets, and (g) lower water cooled recipient flange.

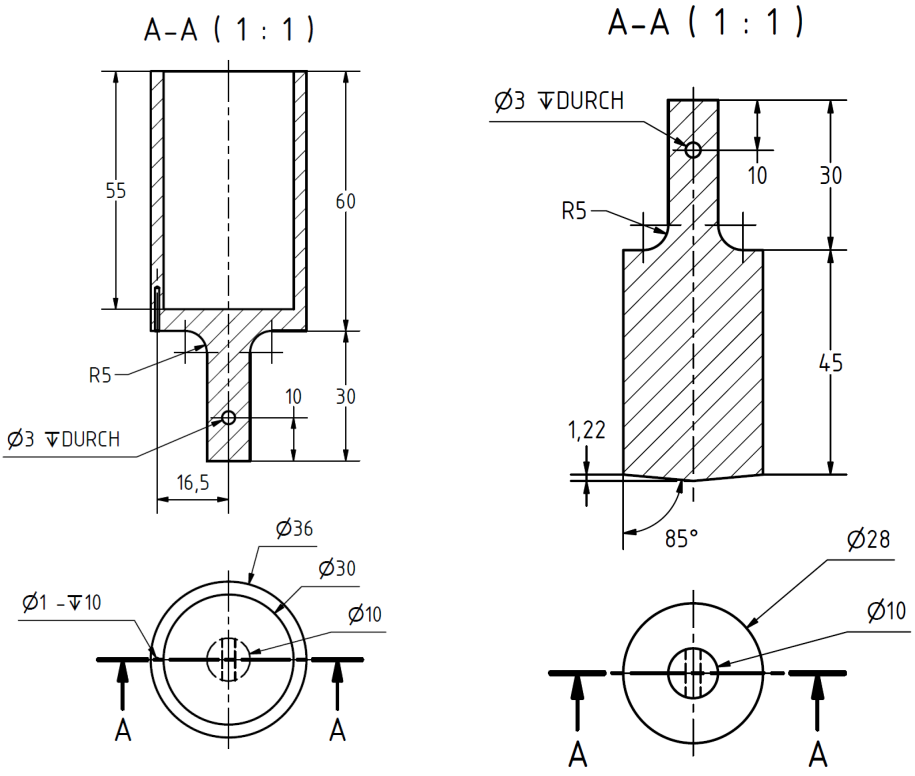

(a) DIN 53019 cup **(b)** DIN 53019 bob

Figure 3.3: Technical drawings of the cup (a) and bob (b) used in this study

3.2.3 Shear cell

In the original device, a narrow gap shear cell with a flat bottomed bob was used. Although the aspect ratio of the shear cell fulfilled DIN standards, the relatively small radii reduced the magnitude of the transmitted torque due to viscous shearing. Furthermore, the mounting shanks of the shear cell were relatively thin and therefore very easily broken during installation or operation. With these problems in mind, several iterations were made to the design of the shear cell until arriving at the present implementation.

The initial iteration of the shear cell for the new device included larger radii as well as considerably thicker mounting shanks. Unfortunately, the larger bob and flat bottom exacerbated the entrapment of gas. Despite this, measurement sensitivity was improved due to the larger moment arm brought about by the increased cup and bob radii. Furthermore, the enlargement of the shank diameter was accompanied by rounded fillets at the interface with the rest of the shear cell, eliminating the stress concentrations at the sharp corners.

The next pair of iterations were based on the Mooney-Ewart conicylinder, which comply with DIN 53019 standards. The bob was modified to include a conical taper at the end. The intention of this taper is to ensure that the shear rate remains constant under the bob as well as to guide gas bubbles to the annulus gap. The only difference in these two iterations was the scale of the shear cell, with a constant aspect ratio. Figures 3.3a and 3.3b show the technical drawings of the cup and bob, respectively.

As the viscometer was intended specifically for measuring reactive zirconium based liquids, materials selection of the shear cell was a critical factor and has remained largely unchanged compared to the original device. With that in mind, the system uses a low-porosity isostatically pressed graphite produced by the SGL Carbon group under the brand name *Sigrafine*[2] R6710. The properties of the material are summarized in table 3.1.

Table 3.1: SGL Carbon Group Sigrafine R6710 Graphite [114]

Property	Value
Average Grain Size	3 μm
Bulk Density	1.88 g cm^{-3}
Porosity	10 %
Electrical Resistivity	13 μΩm
Flexural strength	85 MPa
Compressive strength	170 MPa
Modulus of Elasticity	13.5 GPa
Thermal expansion	4.7×10^{-6} K^{-1}
Thermal conductivity	105 $Wm^{-1}K^{-1}$

Thanks to its moderately high electrical resistivity (about one hundred times that of stainless steel), graphite excels as an inductive susceptor and is used in the Couette rheometer to heat the bulk metallic glass samples. According to the Joule-Lenz law, the heat, Q that can be generated over time with some applied current I is directly proportional to the resistivity, $Q \propto I^2Rt$. Inductive heating causes a non-uniform distribution of current in the conductor, where the maximum current density is located at the surface and decreases exponentially with increasing depth. This appropriately named *skin effect* is quantified by the penetration depth, δ, at which point the power density is equal to $1/exp$ its maximum value at the surface and is proportional to the square root of the ratio of the electrical resistivity to the relative magnetic permeability, μ_r, and the frequency of the field, F [97],

[2]formerly known under the brand name *Ringsdorff*

$$\delta \propto \sqrt{\frac{R}{\mu_r F}} \tag{3.32}$$

A precise calculation of the penetration depth is hindered by the lack of data for the high temperature permeability and resistivity for this graphite. Both values can change drastically with temperature, microstructure (i.e. porosity), and composition (i.e. ash content). However, it is typically on the order of several millimeters using high frequency generators.

One of the early observations using this graphite was the formation of a passivating zirconium-carbide layer at the interface between the melt and shear cell. This layer impedes the contamination of the sample with graphite. Based on a worst-case estimation of the short-circuit diffusion of Sarian and Criscione [151], Way et al. estimated the diffusion coefficient of carbon through the ZrC layer at 1300 K to be $D = 1.184 \times 10^{-15}\text{cm}^2\text{s}^{-1}$ [47]. The diffusion length, then, can be calculated with $x = \sqrt{Dt}$. For an experiment lasting 8 hours at 1300 K, the total diffusion length is 1.85 μm, which is consistent with scanning electron microscopy investigations of the shear cell cross section after a measurement [110]. It should be noted, however, that abrasive wear between the cup and bob may still cause pieces of graphite or ZrC layer to break off and contaminate the measurements. Proper alignment of the shear cells is therefore paramount.

Coaxial alignment of the shear cells during an experiment has always been one of the greatest challenges and improvements to the mounting hardware are ongoing at the time of writing. Originally, the thin shanks of the cup and bob were tightly fitted within holes at the end of a pair of cylindrical titanium getters. Stainless steel set screws threaded into the sides of the getters pressed against the sides of the graphite shank to affix them. The titanium getters themselves were fitted coaxially at holes in the end stainless steel shafts. Off-center stainless steel shear pins were used to transmit torque from the shear cell to and from the shafts. A series of split-ring rigid shaft connectors then connected the shafts to the upper spindle bearing shaft and lower sensor shaft. Tolerance stacking from the excessive amount of coaxial connectors resulted in significant misalignment problems. Consequently, the original viscometer was required a complicated adjustment setup to compensate for these misalignments.

The most recent redesign of the shear cell mounting system has removed many of the redundant connectors that resulted in large cumulative tolerance stacking. The shanks of the cup and bob are fitted directly into the stainless steel shafts. A titanium shear pin is fitted tightly through holes in the sides

of each shaft and shank, doubling as getters for impurities in the atmosphere. Earlier iterations used ceramic pins, but these broke too easily during experiments. Only a single rigid coaxial fitting is used on each shaft to connect them to their respective elements.

3.2.4 Torque Sensor

At the heart of the Couette rheometer lies a high sensitivity torque sensor, which is responsible for the accurate measurement of the reaction torque exhibited on the shear cell due to the viscous stresses in the melt. This sensor is connected to the cup shaft with a rigid coaxial couple and mounting flange. Originally, this was a Lebow 2127-10 reaction torque sensor with a 70 mNm (10 oz-in) nominal capacity. This sensor was connected to the computer with an Analog Devices 5B-38-05 full bridge strain gage module. At some point, this sensor was overloaded to the extent that the press-fitted sensor shaft was loosened within the strain gage ring. Unfortunately, production of that particular sensor has long since been discontinued, and a replacement alternative was necessary.

The current system uses an ME Messsysteme TD-70 torque sensor with a nominal capacity of 25 mNm. This sensor is CNC milled from a single block of aluminum and has an overload capacity of 100 mNm. At the point of overload, further stresses are carried by dead stops along the static circumference of the sensor, thereby reducing the risk of damaging the strain gages. The sensor is intended for use at temperatures below 60°C, necessitating water cooling in the current application. To reduce the chance of electrical interference from the rest of the apparatus, shielded cables and inlet connections are used. Rather than connecting to the strain gage module, a proprietary signal amplifier GSV-2AS is used to communicate between the sensor and the computer. This amplifier allows for on-the-fly sensor zeroing, corrections for minor nonlinearities, and amplification up to 8×.

3.2.5 LabVIEW Programming

This rheometer uses a custom written LabVIEW program for data acquisition as well as communication with external hardware for motion and temperature control. Innumerable changes have been made to the program in the past five years, and an attempt to cover all of the changes would be futile. Instead, only the major developments and their direct implications on viscosity measurements will be covered. The following discussion of the program is organized by the primary functions: user interface, data acquisition, temperature control, motor control, torque sensor communication, and data handling.

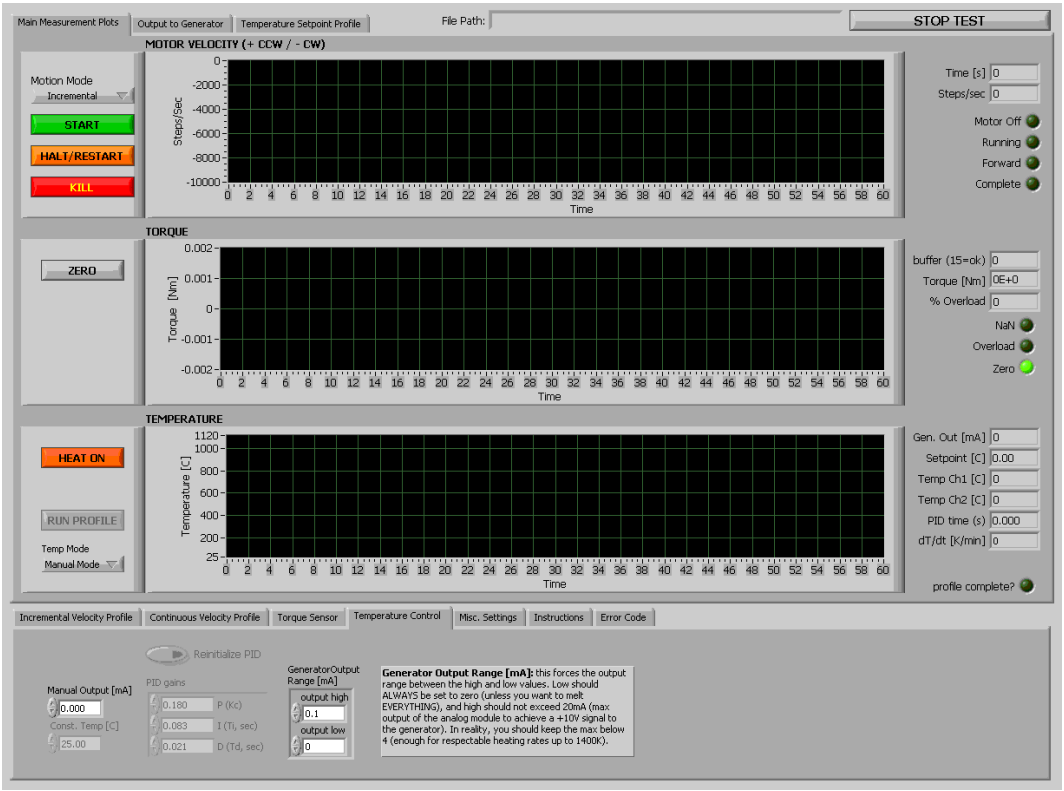

Figure 3.4: The front panel display of the data acquisition program for the Couette rheometer. The three graphs show the motor velocity, torque, and temperature. Controls necessary for running the experiment are located on the left side, while on the right side indicators are provided. Tabs containing further controls are located at the bottom.

User Interface and Data Acquisition

A single data acquisition program provides all of the controls and indicators necessary for running the Couette rheometer. The graphical user interface[3] displays the numeric readouts as well as plots display the torque, temperature, motor velocity, and generator output in real time during a measurement, as shown in figure 3.4. Indicators are provided to notify the user when certain events occur (e.g. sensor zeroing, motor running, data saving to hard disk). Furthermore, tools are available to allow the direct control of most variables in the system.

The original LabVIEW program's user interface lacked a cohesive arrangement of the display elements. Changes to the interface were focused on improving the efficiency of the layout by reorganizing elements based on their function. To avoid cluttering the main window, additional tabs were created to accommodate all of the new functions that were included in the program. Some of the new user interface elements include an overview of the output to

[3]known as the *front panel* in LabVIEW terminology

the high frequency generator, a detailed preview of the temperature program, and an error message panel.

The working functions of the data acquisition program can be found in the block diagram, which operates behind the scenes of the user interface. The block diagram contains four main elements, shown in figure 3.5. Part (a) contains all of the logic for operating the stepper motor, including the definition of the motion profiles and constant velocity modes. Part (b) is a case structure that initializes the temperature controller and allows for the recording of the thermocouple signals. Part (c) is a timed while loop that contains all of the actual data recording logic, including torque, temperature, motor velocity, and generator power signals. Finally, part (d) is a separate case that ensures that the generator is shut off when the program is stopped. If the program crashes or is interrupted, it may be necessary to manually shut down the inductive generator.

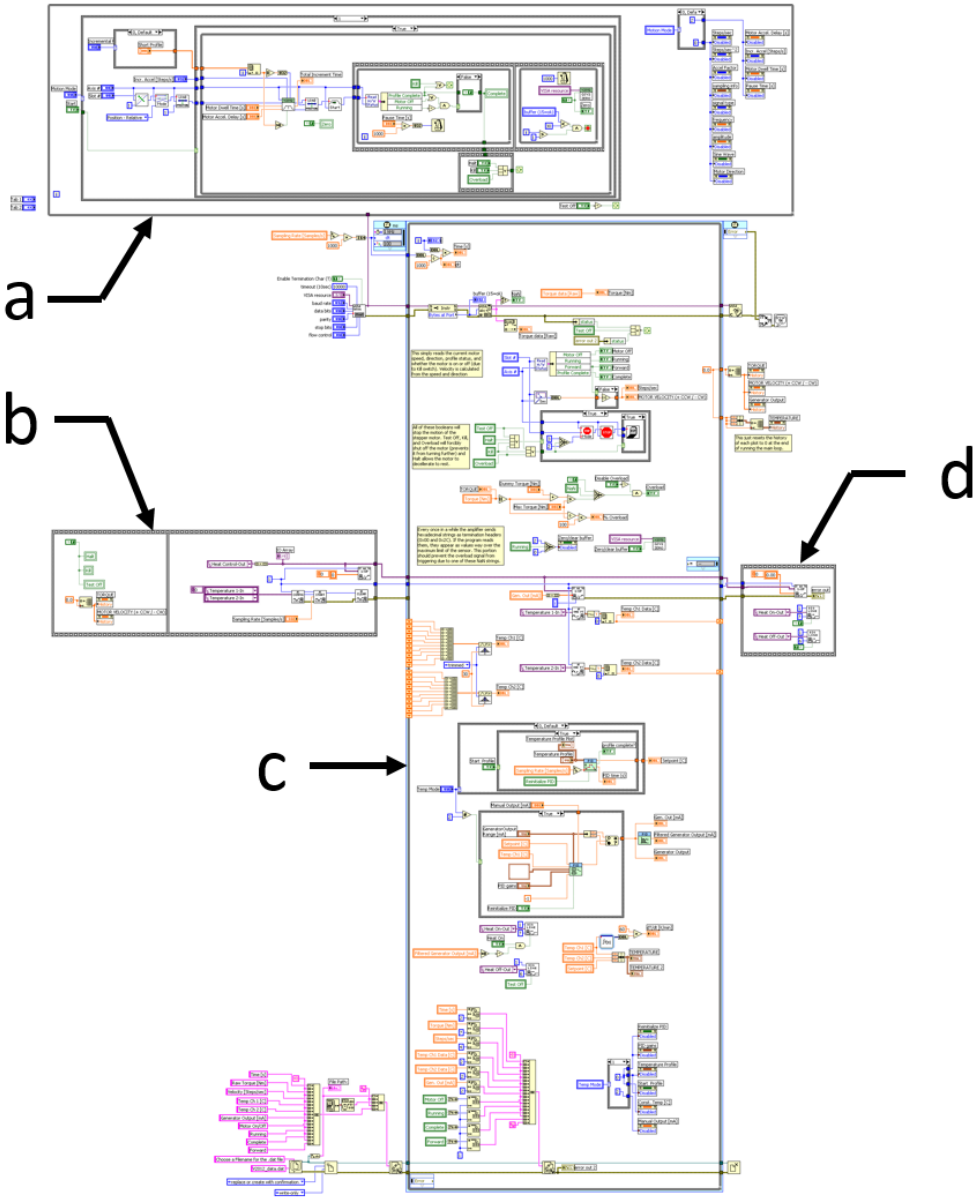

Figure 3.5: The block diagram of the data acquisition program, which is split into four parts, (a) the motor control loop, (b) thermocouple and generator initialization, (c) main data acquisition loop, (d) generator shut off

Temperature Control

Despite being fundamentally similar to the original design, the temperature control loop has been completely overhauled in the new system in order to allow for measurements at low temperatures. At the heart of this system, the generator output current is determined with a Proportional-Integral-Derivative (PID) feedback controller. The input process variable for this PID loop is the digital temperature signal from up to two type K thermocouples embedded in the shear cell. An Analog Devices 5B-37-K-02 module converts the voltage signals from these thermocouples to digital temperature data. These temperatures are compared with a user defined set-point temperature to determine the appropriate output response to the generator. In the event that the signal from the thermocouples is not available as an input, the generator current can also be manually defined.

Perhaps the most significant limitation of the original device was its incapability of controlling temperatures below 900 K. This arose from an inability to properly send a zero signal to the inductive generator. Although the output signal was zero amperes, the generator maintained a minimum power that was substantial enough to heat the shear cell. This minimum power signal can be temporarily disabled by toggling the state of the generator between a standby mode and back to operating mode. Therefore, to circumvent this limitation, additional programming logic was included with the PID controller that switched the generator to the standby mode in the event of a zero signal. As a result,the present device is capable of accurate temperature control from room temperature up to about 1400 K, which is the maximum rated temperature of the type K thermocouples.

Optimization of the PID controller is necessary not only for changes to the shear cell but also for the desired temperature range. Within the LabVIEW environment, the absolute value of the gains themselves are unimportant. Instead, the maximum output signal is defined and the gains relative to each other dictate the response of the generator. Initial tuning of the PID gains was performed according to the Ziegler-Nichols method [181]. First, the derivative and integral gains are left at zero while the proportional gain is adjusted until the temperature signal oscillated at a constant amplitude about the set-point. At this point the proportional gain has reached some critical value, P_c, which, combined with the period of the oscillations, t_c, can be used together to define the Ziegler-Nichols gains:

$$P = 0.60P_c \tag{3.33}$$

$$I = 2P_c/t_c \tag{3.34}$$

$$D = P_c t_c/8 \tag{3.35}$$

Although the Ziegler-Nichols gains are useful as a starting point, they typically require additional manual fine-tuning because of their propensity for overshoot. Increasing the proportional gain will, quite unsurprisingly, result in a larger generator output response for any given change in the temperature. The integral gain accounts for steady state error and will increase the rate at which the process variable will rise towards the set-point. Unfortunately, this can also lead to overshoot. Finally, changing the derivative gain can be used to adjust the time at which oscillations in the response decay (settling time). In practice, the Couette system response is most sensitive to changes in the proportional and derivative gains, while the integral term remains small to minimize overshoot.

In addition to the changes to the PID controller and generator communications, additional techniques were included to allow precise adjustment of heating and cooling rates as well as a fully defined set-point profile system tied to the user interface. During operation in PID mode, the user can toggle between isothermal and a set-point profile modes. Isothermal mode simply uses the PID controller to maintain a constant user-defined temperature. The set-point profile mode consists of an array of times and temperatures. Linear extrapolation between each adjacent point in the array allows the rapid automatic definition of complete thermal protocols for a given experiment. This mode is useful for constant rate experiments as well as the automatic cycling between isothermal steps.

Motor Control

To rotate the upper shaft and bob of the shear cell, the viscometer uses a Pk264-01B unipolar stepper motor manufactured by Oriental Motors. This motor has 2000 steps per revolution and a maximum speed of 12000 steps/s (360 rpm). The LabVIEW controller for this motor has not required significant changes. Essentially, the program allows for the definition of constant velocity and linear acceleration profiles. The only modifications to this program were made to the manner in which the reversing profile is defined. Now, controls for exact definition of the profile are provided on the user interface. Loops of any desired motor profile can also be defined.

One critical part of the motor control program is an emergency overload switch that protects the torque sensor from harm. When the torque sensor exceeds 90% of its maximum rated torque the program sends a *kill* signal to the motor, completely shutting off its power supply such that the bob is free to rotate. Under normal circumstances, reducing the motor velocity to zero via a *halt* signal applies a braking torque to the shaft. This braking torque remains when the motor is stopped, which would exacerbate the overloading of the sensor. Therefore, a *kill* signal is necessary to immediately unload the

torque sensor. For debugging purposes, a manual override switch of the kill signal is included. However, the emergency override should always be active during an actual experiment.

Torque Sensor Communication

The inclusion of a new sensor required a complete overhaul of the section of the program that handled torque measurement. Communication with the sensor is enabled through the COM1 port of the computer at a rate of 10 samples per second. Raw sensor voltage data is read from the GSV-2AS amplifier. Additionally, the sensor can be zeroed on-the-fly through the program. This zeroing is accomplished by sending a specific command line to the amplifier. However, while zeroing, the read value is undefined (not a number) and may trigger the emergency overload switch that shuts off the motor. Therefore, additional logic is included to the prevent this from occurring.

Data Handling

As a measurement is running, the LabVIEW program is continuously writing the data to the hard disk of the computer. In the original program, data was first saved to a .dat file, which had to then be converted to a proprietary .ty1 file. This .ty1 file only existed to add blank columns of data that were required by the final conversion to .txt data. A detailed explanation of this process is included in [122]. Aside from frustrating users with its complexity, this data conversion achieved very little, in fact. Normally .dat files are saved as binary data in order to reduce file sizes. Instead, the .dat files were simply .txt data that with the extension renamed. The new program does away with this conversion process and instead directly saves raw data as readable .txt data.

The saved file only includes the data necessary for analysis and removes redundant information. Raw torque (mV), temperatures from both thermocouples (°C), motor speed (steps/s), motor direction (boolean), generator output (mA), and sensor zeroing status (boolean) are saved. A header is included to provide the user with a record of the experimental protocol and calibration information at the time of the measurement.

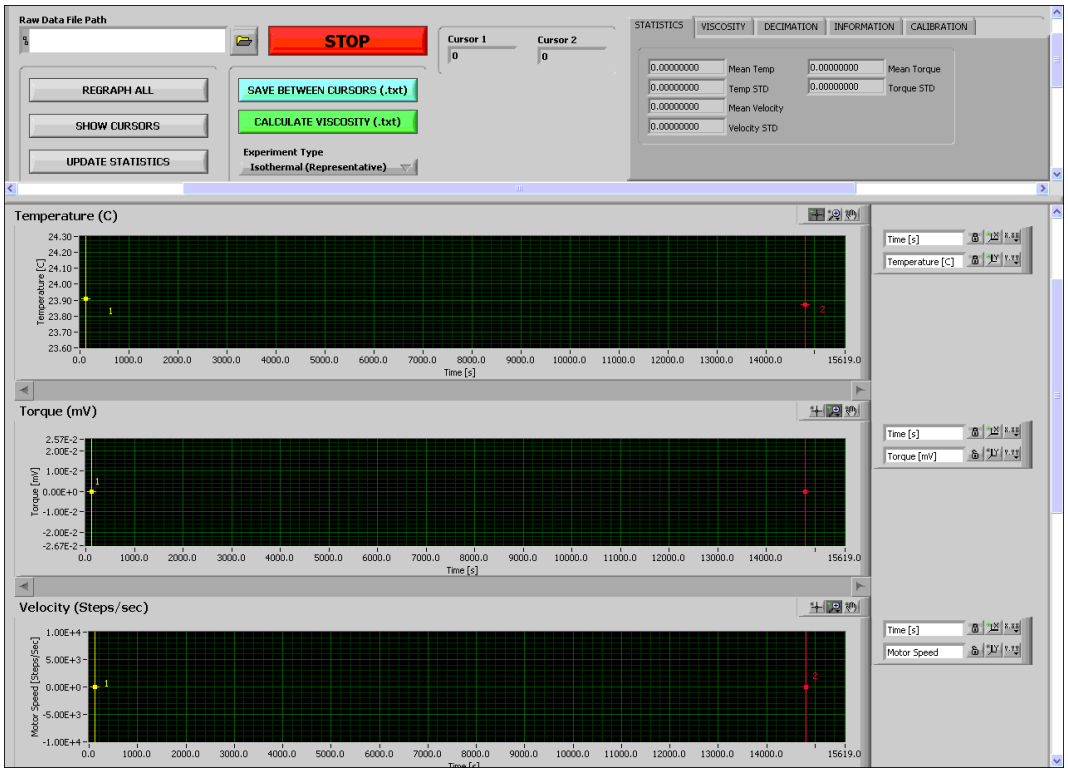

Figure 3.6: The front panel display of the graphical data analysis program. Controls are located in the upper panel, while the raw data from an experiment is plotted on graphs in the lower panel. Using the yellow and red cursors, one can select regions of data to analyze.

Due to the extremely large data sizes after a typical measurement, direct analysis in programs such as Microsoft Excel or Origin are impractical or even impossible. Therefore, a graphical program was developed to reduce the data sets to more reasonable sizes and perform additional analysis when necessary. The front panel of the analysis program is shown in figure 3.6. Upon loading the raw data file into this program, plots of torque, temperature, and motor speed for the entire measurement are provided. With the help of cursors on each plot, the user can then select regions of data to save as separate files. These regions can also be analyzed according to the desired method, either as direct statistical analysis or viscosity analysis. The latter case can be switched between modes for calculating viscosity according to simple Newtonian, representative (Mooney-Ewart), or power law methods. Calibration information must be entered to ensure proper calculation of viscosities.

The block diagram of the data analysis program is shown in figure 3.7. In part (a), the program prompts the user to select a data file for analysis. Additionally, it initializes the cursors for selecting regions of data on each plot. Part (b) is actually three separate loops that coordinate the cursor locations between each plot, ensuring that they update properly upon being moved. Part (c) is the most cumbersome part of this program, as it loads the entire

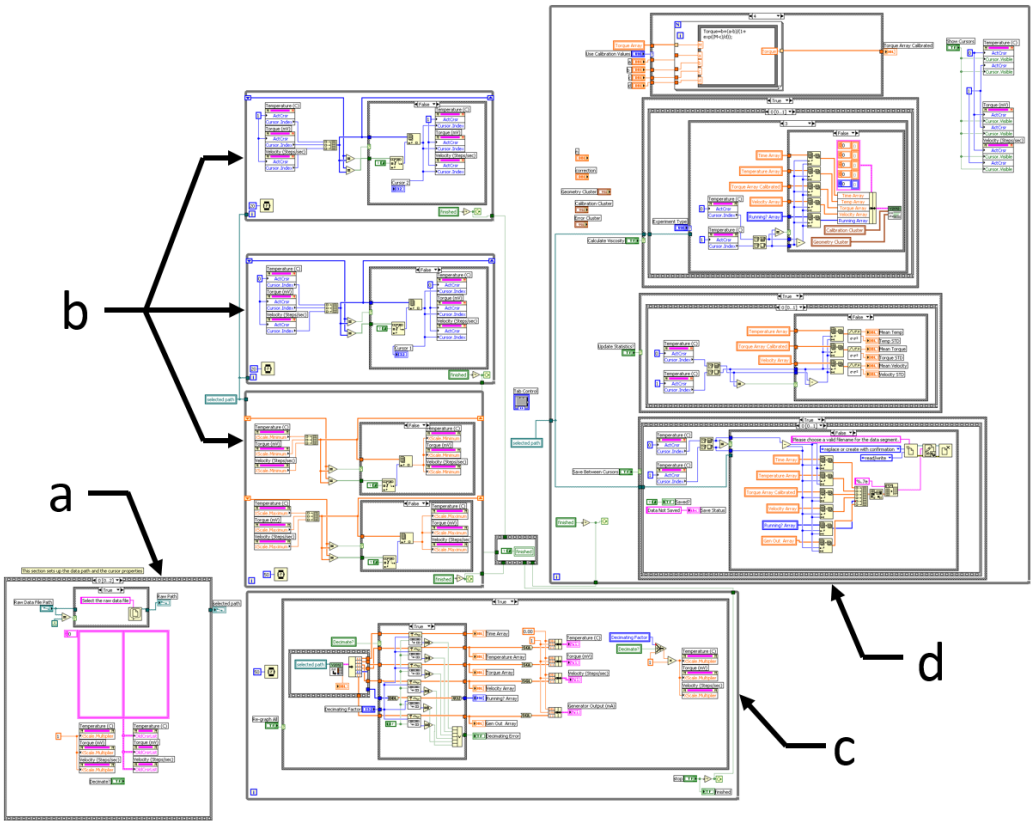

Figure 3.7: The block diagram of the graphical data analysis program. (a) gets the name of the data file and initializes the cursors. (b) reads the position of the cursors and ensures that they are the same on each plot. (c) loads the data file and plots the relevant information. (d) performs all of the desired analysis.

data file that is selected before plotting each relevant data set. This step alone may take up to three hours to complete. Finally, part (d) is actually several analysis programs that can be called upon once part (c) is complete. This final part can perform simple statistical analysis as well as complex viscosity calculations with independent file saving options.

Chapter 4

Methods and Materials

This chapter outlines the theoretical and technical aspects of the experimental methods applied, including a brief overview of the sample production and characterization.

4.1 Materials selection and preparation

All compositions chosen for this study were Zirconium-based alloys with varying degrees of compositional complexity and glass forming ability. Several belong to the Vitreloy family, including $Zr_{58.5}Cu_{15.6}Ni_{12.8}Al_{10.3}Nb_{2.8}$ (Vitreloy 106a), $Zr_{57.0}Cu_{15.4}Ni_{12.6}Al_{10.0}Nb_{5.0}$ (Vitreloy 106), $Zr_{52.5}Cu_{17.9}Ni_{14.6}Al_{10.0}Ti_{5.0}$ (Vitreloy 105), and $Cu_{47.0}Ti_{34.0}Zr_{11.0}Ni_{8.0}$ (Vitreloy 101). Additionally, two alloys based off of Vitreloy 106a that were recently developed by J. Heinrich [121] were included in this study, namely $Zr_{59.3}Cu_{28.8}Al_{10.4}Nb_{1.5}$ (AMZ4) and $Zr705_{60.8}Cu_{28.8}Al_{10.4}$ (AMZ4 705), the latter of which substitutes high purity Zirconium and Niobium with an industrial grade Zr-R60705 pre-alloy. Finally, $Zr_{65.0}Cu_{17.5}Ni_{10.0}Al_{7.5}$ and $Zr_{60.0}Cu_{25.0}Al_{15.0}$ were studied, both of which were originally discovered by Inoue et al. [42]. The relevant material properties of all compositions are summarized in Table X.

Crystalline ingots of master-alloy were prepared in an electric arc-melting furnace using high purity elements (with the exception of the Zr-R60705 used in AMZ4 705) under Titanium-gettered high purity Argon (99.9999% pure). These ingots were cast into amorphous samples by subsequent re-melting and pressure assisted gravity casting into water cooled copper molds of appropriate geometry (e.g. plates for three point beam bending).

4.2 Principles of calorimetric analysis

Calorimetry is the measurement of heat associated with chemical or physical changes. The change in heat ΔQ necessary to raise the temperature of a substance by ΔT is determined by the heat equation

$$\Delta Q = mc\Delta T \tag{4.1}$$

where m and c are the mass and specific heat capacity of the substance, respectively. Calorimeters are classified based on the measurement principle, mode of operation, and principle of construction [60].

4.2.1 Differential scanning calorimetry

Based on the operating principle, differential calorimeters are commonly categorized into either *power compensation* or *heat flux* techniques. In the former case, the sample and reference each have separate temperature sensors and heaters. The power of the furnaces is regulated in order to eliminate any temperature difference arising between the sample and reference and this thermal power is the instrument signal. In contrast, heat flux calorimeters provide the same heat to the sample and reference within a single furnace and the temperature difference between the two is the measurement signal. Schematic illustrations for both are shown in Figure 4.1. Heat flux calorimeters are also known as *calorimetric* DTA or *Boersma* DTA.

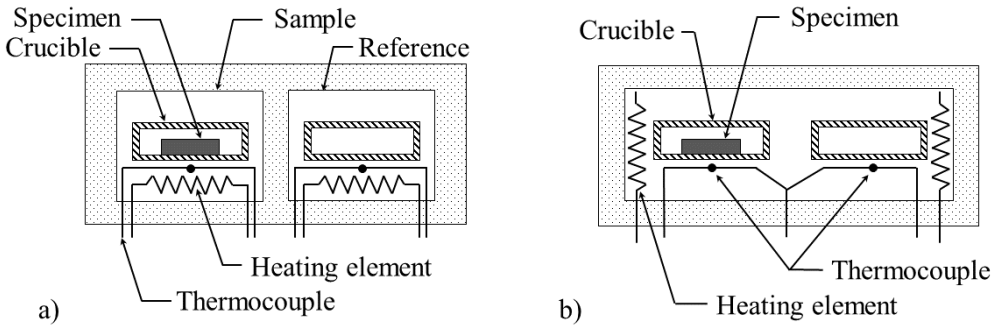

Figure 4.1: A power compensated differential scanning calorimeter (a), showing the sample and reference furnaces with identical temperature sensors and heating elements. An empty crucible is shown in the reference furnace. A heat flux calorimeter (b), where both sample and reference are contained within the same furnace. The thermocouples are shown in a compensating arrangement.

The equation for the heat flow between the sample and thermal energy source was derived by Gray [116]

$$\frac{dQ}{dt} = \underbrace{-\frac{dh}{dt}}_{\text{I}} + \underbrace{(C_S - C_R)\frac{dT}{dt}}_{\text{II}} - \underbrace{RC_S\frac{d^2Q}{dt^2}}_{\text{III}} \tag{4.2}$$

where term I is the evolution of heat from the sample (e.g. from a chemical reaction or phase transition), term II is the heat capacity displacement from the sample and its crucible (C_S) and the reference and its crucible (C_R), and term III describes the lag arising from the thermal impedence between the sample and source of thermal energy, R . Thermal impedence should be minimized as much as possible by using small samples, slow heating or cooling rates, and ensuring good contact between the sample and crucible and between the crucible and temperature sensor. For power compensated DSC measurements the thermal resistance can be assumed to be zero. If an empty reference is used and both crucibles are identical, $C_R = 0$ and equation 4.2 simplifies to

$$\frac{dQ}{dt} = m_S c_S \frac{dT}{dt} \tag{4.3}$$

In practice, the actual heat flow is related to the experimental signal $(dQ/dt)_{exp}$ through a proportionality constant k, which is derived from calibrations with standard materials of known melting temperature and enthalpies of transformation. The integral of the experimental melting peak with respect to time is proportional to the enthalpy of fusion.

4.2.2 Differential thermal analysis

Differential Thermal Analysis (DTA) allows for the qualitative identification of changes in a substance by measuring the temperature differences between a sample and a known reference under equal heat flow conditions. The measurement signal ΔT_{SR} is proportional to the difference in sample temperature T_S and reference temperature T_S

$$\Delta T_{SR} = T_S - T_R \tag{4.4}$$

4.2.3 Specific heat capacity measurements

In this work, the specific heat capacities for $Zr_{65.0}Cu_{17.5}Ni_{10.0}Al_{7.5}$ and $Zr_{60.0}Cu_{25.0}Al_{15.0}$ were investigated calorimetrically using a power-compensated Perkin-Elmer HyperDSC 8500 equipped with a three stage Intracooler III. Amorphous samples (approx. 50 mg) were cut from suction cast plates and ground on at least one side to ensure good contact with the DSC crucible. The active cooling system ensured accurate measurements from -100 to 750°C and the heat flow in this range was calibrated according to the melting transitions of *n*-Decane and elemental In, Sn, and Zn. All experiments were conducted in Al_2O_3 pans under flowing high purity Argon (99.9999%) at 20 mL min^{-1}.

Samples were subjected to a step-wise thermal program, where they were heated to a desired temperature at a rate of 20 K min^{-1} and then held isothermally until the signal equilibrates (180 s). These steps were repeated at 10 K temperature increments until the entire temperature interval was measured. The heat flow rate for any given step corresponds to the difference between the measured heat flow rate at the beginning of the step ($T = 0$) and after the heat flow rate has equilibrated ($T \neq 0$) and is equal to $\dot{Q} = \dot{Q}_{T\neq 0} - \dot{Q}_{T=0}$. This process was conducted for empty crucibles, then a reference material of known specific heat capacity (sapphire), and the specimen of interest. This specimen was measured twice; first for the amorphous sample and second for the crystalline state. In order to ensure the accuracy of the technique, it is necessary to use the same crucible across all three measurements and to minimize displacement of the crucibles within the DSC chamber.

The differential form of equation 4.1 is used to relate the heat flow rate to the mass and specific heat capacity of the sample and reference furnaces of the DSC

$$\frac{dQ}{dt} = (m_S - m_R)(c_S - c_R)\frac{dT}{dt} \tag{4.5}$$

where the subscript S refers to the DSC sample furnace setup and not to any particular specimen, which are distinguished henceforth as *specimen* or *sapphire*. If an empty reference crucible is used, equation 4.5 simplifies to $\dot{Q}_S = m_S c_S \dot{T}$. Furthermore, it is necessary to account for the baseline contribution to heat flow arising from the crucibles themselves, $\dot{Q}_0$, resulting in separate expressions for the specimen and sapphire:

$$\dot{Q}_{specimen} = m_{specimen} c_{specimen} \dot{T} + \dot{Q}_0 \tag{4.6}$$

$$\dot{Q}_{sapphire} = m_{sapphire} c_{sapphire} \dot{T} + \dot{Q}_0 \tag{4.7}$$

Combining equations 4.6 and 4.7 allows the calculation of the specific heat capacity of the specimen

$$c_{specimen} = \frac{\dot{Q}_{specimen} - \dot{Q}_0}{\dot{Q}_{sapphire} - \dot{Q}_0} \cdot \frac{m_{sapphire}}{m_{specimen}} \cdot c_{sapphire} \tag{4.8}$$

or in terms of molar specific heat capacity,

$$c_p(T)_{specimen} = \frac{\dot{Q}_{specimen} - \dot{Q}_0}{\dot{Q}_{sapphire} - \dot{Q}_0} \cdot \frac{m_{sapphire} \cdot \mu_{specimen}}{m_{specimen} \cdot \mu_{sapphire}} \cdot c_p(T)_{sapphire} \tag{4.9}$$

where μ is the molar mass of the specified material. Literature values [54] for the specific heat capacities for sapphire $c_p(T)_{sapphire}$ were used.

4.2.4 High temperature calorimetric measurements

High temperature calorimetric measurements were performed in a Netzsch STA 449/C/6/MFC/G Jupiter DTA using the DSC-c_p sample holder. The graphite crucibles used were manufactured from the material used in the shear cells of the viscometer. Prior to an experiment, these crucibles were ultrasonically cleaned in an ethanol bath and then subjected to a heat treatment at 1200 °C (the same maximum temperature as the Couette measurements) for approximately ten hours. The heat capacity was measured in continuous heating mode under flowing Argon atmosphere (99.9999% pure). To obtain the baseline necessary for equation 4.9, a measurement with an empty crucible was first conducted, followed by a measurement with a sapphire disc of similar mass to the sample. Finally, the sample was measured with the same experimental parameters as those used for the empty and sapphire measurements.

4.3 Principles of thermomechanical analysis

Thermomechanical analysis (TMA) is the study of the temperature dependence of mechanical properties of materials and includes dilatometry, viscosity, and creep measurements. In general, a small load acts on the specimen and the mechanical response (i.e. displacement) is measured as a function of temperature. The measured displacement is the sum of several components, such as load dependent deformation and thermal expansion of the testing apparatus. This necessitates careful control of sample and probe geometry as well as accounting for thermal expansion of the device within the investigated temperature range.

For this work, the selected Zr-based BMGs were investigated with a Netzsch TMA 402. In this particular instrument, the modular construction allows for three-point beam bending as well as dilatometry measurements. A weight of known mass is set upon the top of a push rod, which transmits the load to the specimen (see Figure 4.2). The push rod is made from fused-Si in order to minimize thermal expansion and its geometry can be varied depending on the measurement type. The specimen itself rests upon a fused-Si sample holder and the entire test chamber is enclosed within a quartz glass tube. The push rod displacement is measured by a linear variable differential transformer (LVDT). This type of transducer is a linear solenoid with a electromagnetic core whose movement induces a voltage change that is directly proportional to its displacement. In this particular instrument, the push rod shank contains the electromagnetic core of the LVDT. A three-zone resistance furnace surrounds the quartz glass test chamber and the temperature is monitored using a thermocouple placed as close to the specimen as possible without actually disturbing it. The furnace temperature is regulated with a PID-controller and is calibrated using melting standards of Indium, Tin, and Zinc. Both the TMA head and furnace are water cooled in order to protect the sensitive electronics. Experiments in the TMA were conducted under Argon (99.999% pure) flowing at 50 mL min^{-1}.

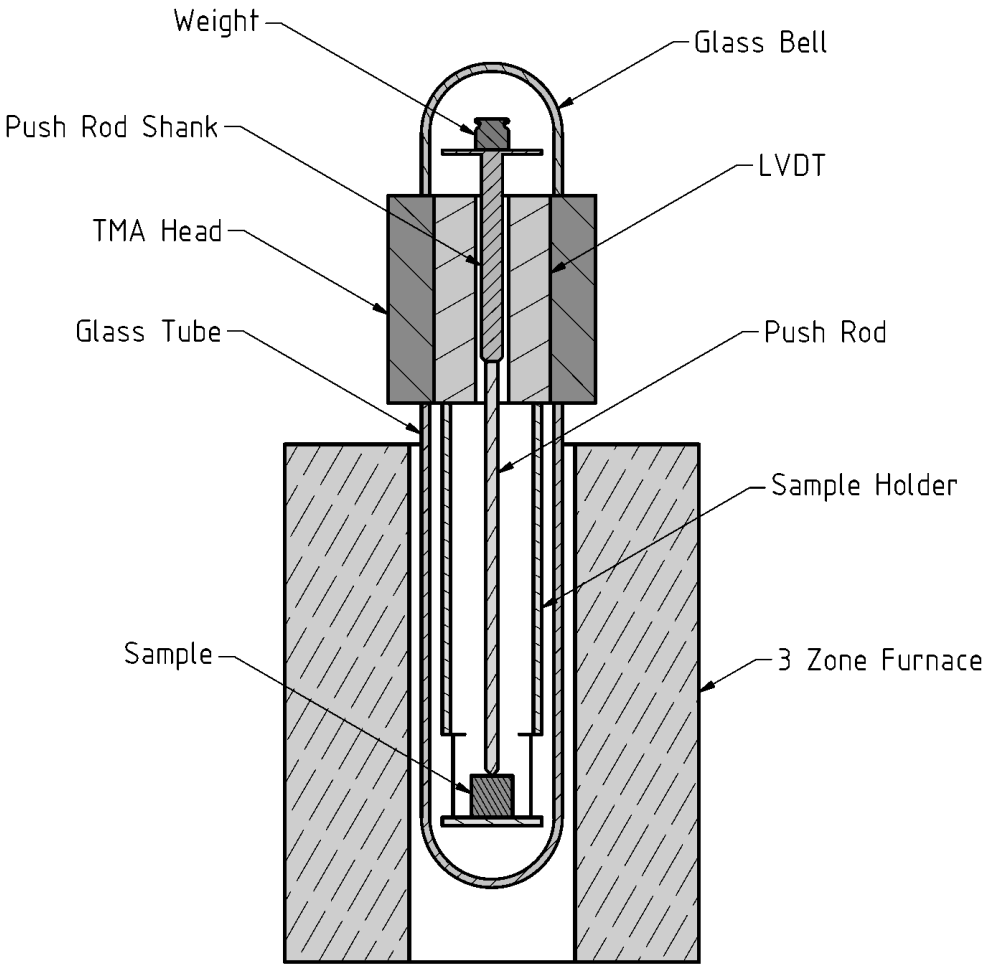

Figure 4.2: Schematic cross section of the Netzsch TMA 402

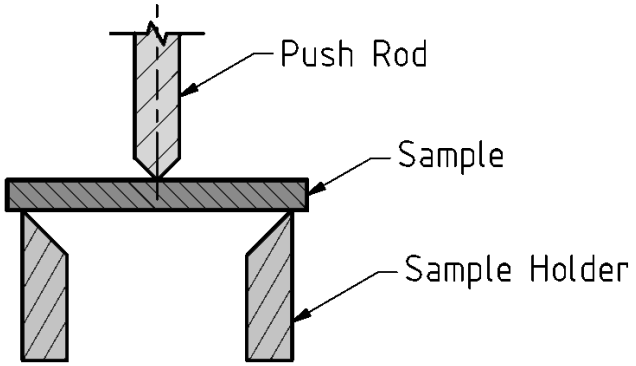

Figure 4.3: Schematic three-point beam bending setup

4.3.1 Three point beam bending

In three-point beam bending experiments, a beam made from the material of interest is simply supported on both sides and a central load is applied with a wedge shaped push rod as seen in figure 4.3. The deflection of the beam under its own distributed weight u_w is

$$u_W = \frac{5mgL^3}{384EI_c} \tag{4.10}$$

where g is the gravitational acceleration constant (m/s^2), the span length L is the distance between the supports ($L = 1.196 \times 10^{-2}$m for the apparatus used), E is the Young's modulus (N/m^2), and I_c is the second area moment of inertia of the beam (m^4) and m is the mass of the section of the beam between the supports contributing to the distributed load (kg). The deflection due to the central load u_M is

$$u_M = \frac{MgL^3}{48EI_c} \tag{4.11}$$

where M is the applied load (kg). The total deflection is determined through the superposition of equations 4.10 and 4.11

$$u_{tot} = \frac{gL^3}{48EI_c}\left(M + \frac{5m}{8}\right) \tag{4.12}$$

In 1906 Trouton investigated beams of pitch sagging under their own weight in order to determine their viscoelastic properties, namely the coefficient of viscous traction λ [165]. He observed that the deflection rate v and viscous traction λ show analogous behavior to the deflection u and Young's modulus E. Additionally, because $3\eta = \lambda$, a direct calculation of the viscosity is enabled by substitution of $u \Rightarrow v$ and $E \Rightarrow 3\eta$ in equation 4.10. Hagy [120] later expanded Trouton's work to account for the contribution of an additional load, resulting in the following expression for viscosity in three point beam bending conditions

$$\eta = -\frac{gL^3}{144 I_c v}\left[M + \frac{\rho A L}{1.6}\right] \tag{4.13}$$

where ρ is the density of the specimen (kg/m^3) and A is the cross section area (m^2). The second area moment of inertia with respect to the neutral fiber of a simply supported rectangular beam is $I_c = bh^3/12$, where b is the width and h is the thickness of the beam (both in m). This calculation has been adopted as a NIST standard [145] for three point beam bending experiments.

Equation 4.13 was used to determine the viscosity of the metallic glass alloys under both isothermal conditions and at a constant heating rate (0.33 K/s). Rectangular beams were cut from as-cast amorphous plates using a diamond saw and subsequently ground to the desired thickness and parallelism. As a general rule, sample thicknesses should be chosen to utilize the entire measurable range of the TMA (2.5×10^{-3}m for the Netzsch TMA 402). For isothermal experiments, thin beams (approx. 2×10^{-4}m) are necessary in order to improve the signal-noise ratio. For constant heating rate scans, thicker beams (8×10^{-4}m) were used to extend the measurement range into the supercooled liquid region. At higher temperatures (i.e. lower viscosities), the beam thickness can be increased accordingly. A constant load of $m = 10$g was used for all of the experiments.

4.4 Containerless experiments

Containerless techniques are invaluable for the processing of liquids and can be combined with non-invasive measurement methods to perform highly accurate investigations of the thermophysical properties and structure. By isolating the sample, it is possible to eliminate heterogeneous nucleation sites that would otherwise occur between the melt and crucible, thereby permitting significantly larger undercooling and in-situ vitrification in some cases. Furthermore, the absence of a crucible drastically reduces the risk of contamination of the sample, which can be further diminished with an appropriate processing atmosphere.

Sample isolation can be accomplished either through transient or steady-state methods, where the former relies typically on free falling droplets and the latter on supplying a controlled force to counteract gravity [177]. There are a wide variety of steady state techniques available, including acoustic, aerodynamic, electromagnetic, electrostatic, gas film, and magnetic levitators. Depending on the method, additional forces can be supplied in order to control the position and shape of the liquid droplet. The magnitude of the levitating force and the surface tension of the liquid limit the maximum droplet size.

Droplet size is also a critical factor for undercooling experiments because it governs the maximum cooling rate. The total heat that must be extracted upon cooling is directly proportional to the sample volume (refer to equation 4.1). This heat must be extracted from the core of the sample and dissipated through convective or emissive heat transfer at the free surface. The smaller the droplet is, the faster the cooling rate will be. Furthermore, it has been shown that the size of the droplet under terrestrial conditions has a large impact on the determination of viscosity under terrestrial conditions. Large droplets tend to have irregular deformations during oscillation, which violates the key assumptions behind the calculations used.

As part of an ongoing cooperation between the German Aerospace Center (Deutsches Zentrum für Luft und Raumfahrt, DLR), the viscosities of the highly-reactive Zr-based melts were measured using electromagnetic levitation (EML) and electrostatic levitation (ESL) techniques. The ESL work was conducted in tandem with the Isabell Jonas and Dr. Fan Yang at the DLR.

4.4.1 Electromagnetic levitation

Electromagnetic levitation has been used extensively since the 1960's for containerless research of the thermophysical properties of liquid metals [17, 63, 89, 155]. This technique relies on the fact that an alternating current electromagnetic field will induce eddy currents in a conductive sample. According

to Lenz's law, these currents create a magnetic field opposing the primary field, leading to the repulsive Lorentz forces necessary for levitation whose magnitude can be expressed as [35]

$$F_L = -\frac{2\pi \nabla B^2 r^3 L(s)}{3\mu_0} \tag{4.14}$$

where F_L is the Lorentz force, B is the magnetic field, μ_0 is the magnetic permeability, r is the radius of the sample, and s is a dimensionless quantity that depends on the electrical conductivity of the sample, σ, and the frequency of the alternating magnetic field, ω according to

$$s = r\sqrt{\frac{\omega\sigma\mu_0}{2}} \tag{4.15}$$

and the function $L(s)$ is defined as

$$L(s) = \frac{3}{4}\left(1 - \frac{3}{2s}\frac{sinh(2s) - sin(2s)}{cosh(2s) - cos(2s)}\right) \tag{4.16}$$

Simultaneously, ohmic dissipation of the eddy currents heats the sample and the absorbed power is given by

$$P = \frac{2\pi B^2 \omega r^3 H(s)}{3\mu_0} \tag{4.17}$$

where the function $H(s)$ is given by

$$H(s) = \frac{9}{4s^2}\left(s\frac{sinh(2s) + sin(2s)}{cosh(2s) - cos(2s)} - 1\right) \tag{4.18}$$

To achieve stable levitation, the sample must be positioned within a potential well generated by electromagnetic fields from appropriately shaped coils. In terrestrial EML, the primary field coil is wound conically along the vertical axis

such that the magnetic field is stronger towards the bottom. From equations 4.16 and 4.18, it is clear that the Lorentz force and dissipated power depend differently on the field frequency, which leads to a limited range of frequencies for which temperature control is possible [55]. Temperatures can be controlled by varying the vertical position of the sample within the conical section of the primary field coil. The maximum temperatures are achieved where the magnetic field and power absorption are highest, which occurs in sections where the winding diameter is smallest.

In ultra-high vacuum conditions, samples levitating in the EML will approach an equilibrium temperature given by a balance of the absorbed power P with the heat radiated from the sample to the environment according to Planck's law

$$P = \dot{Q}_r = -4\pi r^2 \sigma_{SB} \epsilon_T \left(T^4 - T_E^4\right) \tag{4.19}$$

where r is the sample radius, σ_{SB} is the Stefan-Boltzmann constant (5.6705×10^{-8} W/m^{2}K^4), ϵ_T is the total hemispherical emissivity, and T_E is the absolute temperature of the surrounding environment. Due to the intrinsically coupled levitation force and power absorption, large undercoolings are extremely challenging without forced convection of a cooling gas.

TEMPUS Microgravity EML

The principles of EML can be applied to microgravity conditions but require a completely different construction. Stable sample positioning is possible with much lower field magnitudes because gravitational forces are more than three orders of magnitude smaller than in earthbound conditions. Furthermore, these gravitational forces are statistically distributed, meaning that the electromagnetic Lorentz forces are used strictly for positioning rather than levitation. Microgravity EML has several advantages over terrestrial applications. The strong inhomogeneous magnetic fields in terrestrial EML can deform a liquid metal droplet, drastically complicating frequency spectra analysis used in surface tension and viscosity measurements. In contrast, the relatively weak positiong field strength makes it possible to attain nearly spherical quiescent droplets. Furthermore, low field strengths minimize turbulent flow due to induced convection. These experiments can also operate under a wider temperature range because the power dissipated by the positioning field is negligible.

This technique is used in the TEMPUS (Tiegelfreies ElektroMagnetisches Prozessieren Unter Schwerelosgkeit) facility, which was constructed by

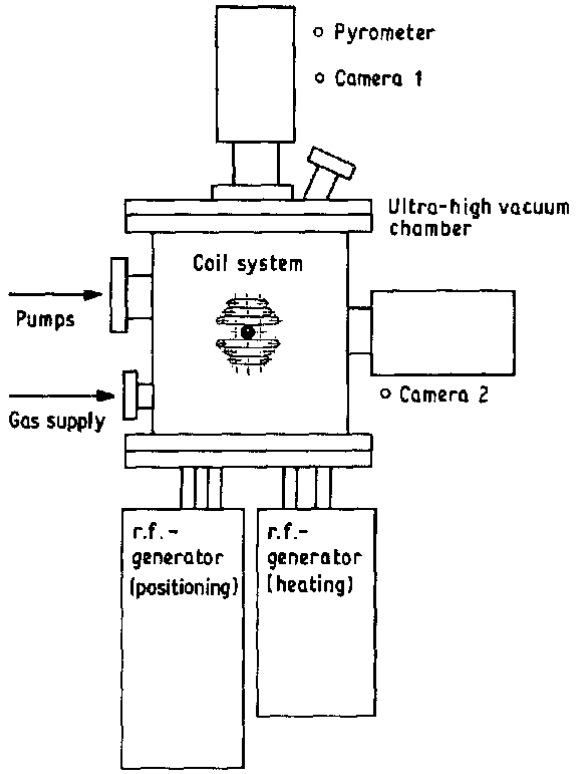

Figure 4.4: Schematic of the TEMPUS EML device showing the recipient, generators, RF-coils, and camera positions. Figure adapted from [33].

Daimler-Benz Aerospace under contract from the German space agency (at the time, Deutsche Agentur für Raumfahrtangelegenheiten, DARA) to be used in the Second International Microgravity Laboratory (IML-2). The TEMPUS facility is currently operated by the DLR in conjunction with Novespace parabolic flight campaigns that are sponsored by the French space agency (Centre national d'études spatiales, CNES). Each campaign consists of up to five days of parabolic flights with thirty parabolas flown every day. Approximately twenty five seconds of weightlessness are experienced with each parabola.

Figure 4.4 shows a schematic illustration of the TEMPUS-EML device used in this study. The TEMPUS facility uses independent positioning and heating coils. Two pairs of parallel positioning coils with a phase shift of 180°create an axisymmetric quadrupole field. This field has a central potential well whose strong gradients lead to very stable sample positioning. Meanwhile, the low magnitude of the positioning field does not efficiently heat the sample, which accommodates measurements at lower temperatures than can be realized in earthbound EML. Therefore, a separate heating coil is wound equatorally around the sample and parallel to the positioning coils. This is wound in a Helmholtz configuration in order to provide a homogeneous dipole field that minimizes displacement of the sample from its stable central position while

maintaining a high heating efficiency.

Sample temperatures are monitored in the TEMPUS facility using infrared pyrometry and two cameras (each operating at 50 Hz) monitor the sample position. One camera views the radial sample position from above, and the other monitors vertical displacement from the side of the chamber. Additionally, a high frequency camera (200 Hz) is used for precise measurement of the sample shape with the help of image processing software.

High temperature surface tension and viscosity measurements were conducted on $Zr_{59.3}Cu_{28.8}Al_{10.4}Nb_{1.5}$ (AMZ4) and $Zr705_{60.8}Cu_{28.8}Al_{10.4}$ (AMZ4 705) in the TEMPUS EML facility. Samples with diameters of approximately 7 mm were prepared by cutting appropriate masses from ingots of master alloy and subsequently melting them with an arc-furnace under high purity Argon. The molten droplets were allowed to cool into approximately spherical samples within the hemispherical indents of the water cooled copper crucible of the arc-melter. Cylindrical Alumina (Al_2O_3) sample holders were used with cross shaped windows for optical monitoring and perforated bases for gas flow. Forced convective cooling with Helium gas was used in order to solidify the samples before the end of the parabola.

Samples were preheated to 700°C before each parabola and subsequently heated to a maximum temperature of 1200°C as soon as the microgravity phase started. The initial heating pulse caused significant turbulence in the samples, requiring several seconds to reach quiescence. To perturb the sample, brief pulses from the heating coil were triggered at approximately 1100°C and 1000°C. Analysis of the high speed video data was performed using the TeVi software package developed specifically for these measurements.

4.4.2 Electrostatic levitation

In 1993, Rhim and coworkers first pioneered [99] the application of electrostatic levitation for the study of thermophysical properties of undercooled liquids. Coulomb forces are used to levitate and position a charged sample in an electrostatic field. There are several key advantages to using ESL versus EML for high temperature material research. Most importantly, heating and levitation are independent in ESL experiments, allowing for access to a much broader range of experimental temperatures. Heating is supplied with lasers or lamps that are focused on the sample. Another advantage is that electrostatic forces do not subject a liquid droplet to strong convective currents that may otherwise distort the shape of the sample, unlike in strong magnetic fields. Furthermore, ESL samples are not restricted to electrically conductive materials. All of these advantages make ESL an invaluable technique for

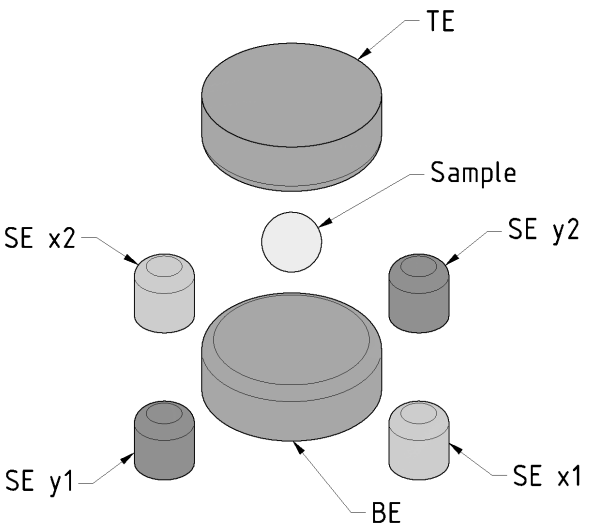

Figure 4.5: Illustration of a typical arrangement of electrodes used in terrestrial ESL. Sample position is controlled vertically (z direction) with the top and bottom electrodes (*TE* and *BE*, respectively) and lateral positioning (x and y directions) with the side electrodes (*SE x1*, *SE x2*, *SE y1*, and *SE y2*).

the investigation of the thermophysical properties of high temperature and undercooled liquids.

Gravitational forces are countered by a pair of electrodes located above and below the sample (z-electrodes) and lateral positioning is controlled by two pairs of electrodes (x- and y-electrodes) on either side of the bottom electrode (see figure 4.5). The levitation force required to position a sample between two parallel electrodes is

$$mg = QV/L \tag{4.20}$$

where m is the mass of the sample having a charge Q and V is the voltage difference between the two electrodes that are separated by some distance L. According e to Earnshaw's theorem [99], no equilibrium position exists in three dimensions for an electrostatically positioned point charge, therefore necessitating the use of feedback positioning control. A series of orthogonally arranged expanded lasers cast the shadow of the sample onto position sensitive photodetectors (PSDs), which measure the sample displacement and provide the feedback signal for the position control algorithm [94].

In order for electrostatic positioning and levitation, sufficient (positive) surface charge must be generated through capacitive, photoelectric, and thermionic charging [99]. Capacitive charging is used at the very beginning of an ESL experiment to launch the sample and is achieved by increasing the (negative) potential of the top-electrode until electrical contact between the sample and the bottom-electrode is broken.

Once a sample has been successfully launched, surface charge is maintained at low temperatures through photoelectric charging with ultraviolet (UV) irradiation. The photoelectric effect was described by Einstein in terms of the kinetic energy of an emitted electron as

$$\epsilon_m = hf - \phi \tag{4.21}$$

where h is Planck's constant, f is the frequency of the incident radiation, and ϕ is the work function. Emission of photoelectrons occurs when incident electromagnetic radiation overcomes the binding energy (work function) of the electrons at the surface. UV radiation with photon energies of 20 eV are sufficient for charging of metallic samples, which typically have work functions on the order of several eV [94].

At high temperatures, thermionic emission begins to dominate the process of charging the sample. The rate of emission of electrons due to thermal excitation is described by Richardson's law

$$J = A_R T^2 exp\left(-\frac{\phi}{k_B T}\right) \tag{4.22}$$

where J is the electron current density (A), A_R is Richardson's constant ($A_R \approx 120$ A cm^{-2}K^{-2}), T is the absolute temperature, ϕ is the work function, and k_B is Boltzmann's constant [26, 94].

Samples in the ESL are heated with an infrared ($\lambda = 808$ nm) Nd:YAG laser beam focused on the sample. Temperatures are measured with a single color pyrometer with an estimated error of ± 10 K. Meanwhile, sample cooling in the ESL is governed purely through radiative heat transfer to the surroundings as described by Planck's law

$$mc_p \frac{dT}{dt} = -4\pi r^2 \sigma_{SB} \epsilon_T \left(T^4 - T_E^4\right) \tag{4.23}$$

where r is the sample radius, σ_{SB} is the Stefan-Boltzmann constant (5.6705×10^{-8} W/m^{2}K^4), ϵ_T is the total hemispherical emissivity, and T_E is the absolute temperature of the surrounding environment [102]. If the cooling rate dT/dt is known, it is possible determine the ratio of specific heat capacity to the total hemispherical emissivity c_p/ϵ_T from the experimental cooling curve.

All of the alloys in this study were measured in the ESL facilities at the DLR by Isabell Jonas. Samples with diameters up to 2 mm were prepared by cutting appropriate masses from master alloy ingots and subsequently re-melting them in an electric arc-furnace under high purity Argon. Spherical samples were created by solidifying the molten droplet in hemispherical indents of water-cooled copper crucible.

4.4.3 Oscillating droplet measurements

With the help of containerless processing, it is possible to accurately measure the viscosity and surface tension of liquid metals over a wide range of temperatures by observing the surface oscillations a levitated droplet. In the TEMPUS EML, radial contractions of the droplet are induced through pulses of the heating field. Similarly, in the ESL facility, pertubations of the droplet are a result from pulses of the vertical positioning electrodes. The surface tension is derived directly from the resonant frequency of the oscillations while its damping yields the viscosity.

In the simplest case, the shape of a liquid droplet will be spherical absence of external forces. By subjecting such a droplet to small oscillations, the radius will vary with time according to

$$r = r_0 \left[1 + \delta cos\left(\omega t\right) e^{-\Gamma t}\right] \tag{4.24}$$

where r_0 is the quiescent radius, ω is the frequency, and Γ is the damping constant. If viscous damping is the only dissipation mechanism (e.g. no turbulence, surface layers, or external forces), then the viscosity can be related to the damping constant with Lamb's formula

$$\Gamma = \frac{20\pi}{3}\frac{\eta r_0}{m} \tag{4.25}$$

where m is the mass of the droplet. In order to determine the surface tension, it is necessary to decompose the oscillation signal into its frequency spectra using a Fourier transform. The presence of a single peak in the spectra corresponds to the resonant frequency, ω_R. The damping constant is related to the full width at half maximum of the resonant frequency peak $\Delta\,\omega_R|_{1/2}$ according to the following expression [33, 64]

$$\Gamma = \frac{\pi}{\sqrt{3}}\Delta\,\omega_R|_{1/2} \tag{4.26}$$

and the surface tension is related to the resonant frequency according to

$$\gamma = \frac{3\pi}{8}m\omega_R^2 \tag{4.27}$$

Unfortunately, equation 4.24 is only a special case that is difficult to realize under normal laboratory conditions. In reality, the frequency of a droplet will be influenced by aspherity, gravity, external forces, and sample rotation [33]. Cummings and Blackburn [27] have shown that these disturbances manifest in a splitting of the fundamental oscillation mode into up to five sidebands. This splitting be understood by examining the most generalized form of the oscillations of the radius, given by

$$r_{l,n} = cos\left(\omega_{l,n}t\right)e^{-\Gamma_{l,n}t}P_l^n\left(cos\theta\right)cos\left[n\left(\phi-\phi_0\right)\right] \tag{4.28}$$

where θ is the angle with respect to the symmetry axis, P is a Legendre polynomial describing the spherical harmonics, ϕ_0 is an arbitrary symmetry direction, $l \geq 2$ is a label indicating the normal modes, and $|n| \leq l$. The general relationship between the resonant frequency and surface tension were derived by Rayleigh as

$$\omega_l^2 = \frac{4\pi}{3}\frac{\gamma}{m} l\,(l-1)\,(l+2) \tag{4.29}$$

which is identical to equation 4.27 when only considering the fundamental mode $l = 2$. The Legendre function associated with $l = 2$ are

$$P_2^0\,(cos\theta) = \frac{1}{4}\,(3cos2\theta + 1) \tag{4.30}$$

$$P_2^1\,(cos\theta) = -\frac{3}{2} sin2\theta \tag{4.31}$$

$$P_2^2\,(cos\theta) = \frac{3}{2}\,(1 - cos2\theta) \tag{4.32}$$

The aspherical distortion of a non-rotating droplet shape causes splitting of the fundamental frequency into three distinct peaks $n = 0, \pm 1, \pm 2$. To make matters even more complicated, rotation of a droplet will display two additional peaks that influence only the $n \neq 0$ modes [27, 33]. The frequency contribution from this rotation is given by

$$\omega_{l,n}^r = \omega_{l,n}^0 + \frac{m}{2}\Omega \tag{4.33}$$

where Ω is the rotational frequency about the z-axis. Furthermore, translational oscillations will influence all of the frequencies according to

$$\omega_2^2 = \frac{1}{5}\sum_{n=-2}^{+2} \omega_{2,n}^2 - 2\omega_t^2 \tag{4.34}$$

where ω_t is the translational frequency. In order to determine the resonant frequency, therefore, it is necessary to calculate the total contributions from all of the external forces, rotation, and translational effects.

Each mode must be identified and correlated with a peak in the frequency spectra. If the sample is viewed from the side (as they are in these experiments), then the $l = 2$ modes can be identified according to figure 4.6. In both ESL and EML techniques, the droplet is perturbed via an excitation of the $l = 2$, $m = 0$ mode, whereby the droplet is vertically elongated. In

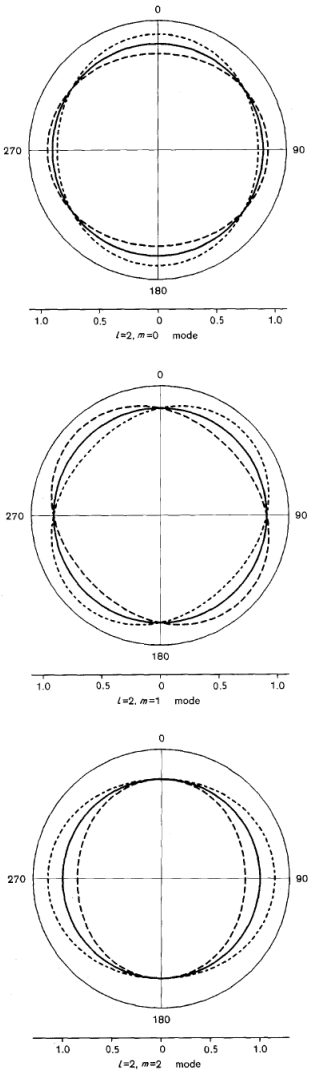

Figure 4.6: Schematic illustration of the $l = 2$ modes viewed from the side of an oscillating droplet, (top) $m = 0$, (center) $m = 1$, and (bottom) $m = 2$. Figure adapted from [33].

the absence of other external forces and instabilities, the release of the heating pulse will allow the droplet to return to equilibrium shape, driven by the surface tension. The resulting oscillations under ideal conditions should be readily identifiable. However, under realistic laboratory conditions the oscillations may be disturbed, necessitating the identification of the modes before analysis can be performed. In this work, the identification of multi-modal oscillations is used to assess the viability of Lamb's formula and a more detailed and quantitative analysis of turbulent oscillations was not attempted.

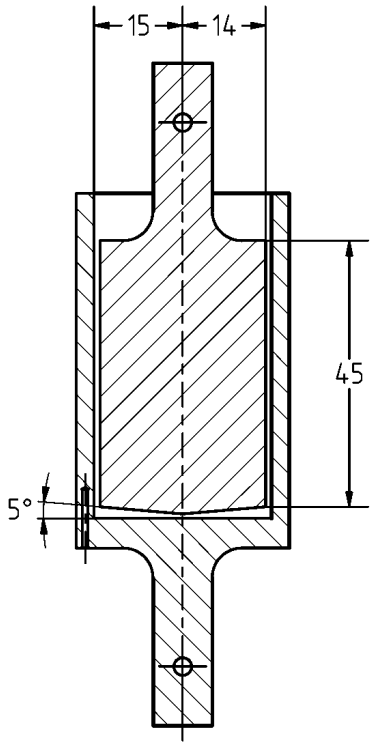

Figure 4.7: Technical drawing of the Mooney-Ewart conicylinder used in this work, with the relevant dimensions shown $R_o = 15$mm, $R_i = 14$mm, L= 45mm, and $\phi = 5°$.

4.5 Couette rheometry

This section will focus on the experimental procedures used in this work because the fundamentals of Couette rheometry have been covered in a preceding chapter. Using the high temperature concentric cylinder rheometer, the viscosities of all compositions in this study were investigated above their respective liquidus temperatures. Both the temperature and shear rate dependent flows were assessed using a variety of procedures.

All of the concentric cylinder viscosity measurements in this study were conducted with DIN 53019 compliant Mooney-Ewart shear cells as shown in figure 4.7. One practical advantage of using this conicylinder type shear cell is that the tapered bob prevents the entrapment of bubbles that may otherwise disturb the measurement. These shear cells were machined in-house out of low porosity graphite (see appendix A.2). Prior to an experiment, these shear cells must be ultrasonically cleaned in an ethanol bath.

The viscometer recipient must first be pumped to a vacuum of 5×10^{-5}mbar and subsequently filled to a pressure of 500 mbar with high purity Argon (99.9999%). This inert environment is necessary for reducing evaporation

during an experiment and to reduce contamination of the melt. It should be noted that the sealant flanges of this viscometer are only functional when the recipient pressure is less than atmospheric pressure. Expansion of the gas upon heating must therefore be considered when filling the chamber with Argon. Furthermore, contaminants in the inert gas are reduced using a pair of titanium getters that are located above and below the shear cell.

Up to 6 cm^3 of liquid metal is required to fill the shear cell, amounting to about three crystalline master-alloy ingots of appropriate mass (depending on the composition). Once the recipient has been filled with protective gas, these ingots are melted together directly in the cup of the viscometer. Once the ingots have completely melted, the bob is lowered slowly into the melt. Simultaneously, it is necessary to rotate the bob slowly by hand in order to assist in maintaining concentricity as well as to push out any Argon bubbles that may get trapped. Once the bob is fully immersed and the temperature has equilibrated, the experiment can begin.

The first step in any of the concentric cylinder rheometer measurements is to determine the maximum range of temperatures, or more specifically, to determine the point at which the liquid freezes. Starting at the maximum temperature ($T_{max} \sim 1100°$ C), a low shear rate ($\dot{\gamma} = 228\ s^{-1}$) is applied in the counter clockwise direction using a stepwise profile. The sample is then cooled continuously at ± 20 K min^{-1} until the sensor overload is triggered, and the temperature at which this occurs is noted as T_{OL}. The lowest temperature that should be used is $T_{min} = T_{OL} + 10$K, which provides a buffer for higher shear rates (i.e. higher torque) while extending the measurement as far as possible. The sample is then reheated to T_{max} in preparation for the main measurement.

The temperature dependent flow behavior was investigated principally with continuous heating and cooling experiments. In this type of experiment, the sample is subjected to a stepwise shear profile at a given rate and direction and then the temperature is cycled twice between T_{max} and T_{min} at ∓ 20 K min^{-1}. This heating and cooling cycle is then repeated for different shear rates and directions ($\dot{\gamma}_1 = 228\ s^{-1}$, $\dot{\gamma}_2 = 332\ s^{-1}$, $\dot{\gamma}_3 = 456\ s^{-1}$ each repeated in counterclockwise and clockwise directions). The timing of the stepwise profile is set such that the motor dwell time and pause (zeroing) time are both five seconds and the motor accelerates at 15.7 rad s^{-2} (5000 Steps s^{-2}).

Isothermal experiments were also conducted for a wider range of shear rates. The melt was sheared using a stepwise shear rate profile similar to the DIN 51309[1] standard that was used to calibrate the TD70 torque sensor. In this procedure, any given shear rate is repeated three times before moving on

[1]This is not a typo, but rather a pure coincidence that the standard for torque sensor calibration is an anagram of the standard for concentric cylinder viscosity measurements.

to the next rate and all rates in a single direction are grouped together. At the very beginning and upon reversal of directions, at least three high speed steps in the direction of the following steps are applied to mitigate possible sensor hysteresis effects.

Upon completion of an experiment, the raw data must be converted into viscosities with the custom built LabVIEW program as described in the preceding chapter. This program parses the torque due to viscous shearing on the cup for each motion step and then calculates the viscosity based on narrow gap concentric cylinder rheometer standards. According to DIN 53019, the maximum allowable gap ratio to be classified as a narrow gap system is

$$\delta_{cc} = R_o/R_i \leq 1.0847 \tag{4.35}$$

where R_o and R_i are the outer and inner radii, respectively. The gap ratio for the shear cell used in this study is $\delta_{cc} = 1.0714$, which satisfies the conditions for classification as a narrow gap. The average shear stress in the annulus is given by

$$\tau_{ave} = \left(\frac{1+\delta_{cc}^2}{2\cdot\delta_{cc}}\right)\frac{M}{2\pi L R_i^2 c_L} \tag{4.36}$$

where M is the torque on the cup and c_L is a correction factor for the torque contribution of the conical apex of the bob. The correction factor can be determined through calibrations using measurements of standard oils as described in detail in [122]. The average shear rate in the annulus is

$$\dot{\gamma}_{ave} = \left(\frac{1+\delta_{cc}^2}{\delta_{cc}^2-1}\right)\omega \tag{4.37}$$

where ω is the angular velocity of the bob (rad s^{-1}). If Ω is the angular velocity in steps/sec, then $\omega = 2\pi\Omega/2000$ radians/s. The representative shear viscosity for a Newtonian fluid is then

$$\eta_{rep} = \frac{\tau_{ave}}{\dot{\gamma}_{ave}} \tag{4.38}$$

or in its expanded form

$$\eta_{rep} = \frac{R_o^2 - R_i^2}{4\pi L R_o^2 R_i^2 c_L} \cdot \frac{\bar{M}}{\omega} \tag{4.39}$$

Concentric cylinder viscosity measurements were the principle method used in this study and were conducted for all of the relevant Zr-based compositions. After the conclusion of these measurements, cross sectional slices of the cup and bob were prepared for *ex-situ* Energy-dispersive X-ray spectroscopy analysis of the interface between the melt and graphite.

Chapter 5

Results and Discussion

In this chapter, the experimental results will be presented and discussed for the methods outlined in chapter 4. Keeping in theme with the eventual discussion of the Strong-Fragile transition, the presentation of the results is separated into the low and high temperature regimes.

In the former regime, viscosities measured by isothermal three point beam bending in the TMA near the glass transition will be presented for two variants of the AMZ4 alloy as well as $Zr_{65.0}Cu_{17.5}Ni_{10.0}Al_{7.5}$ and $Zr_{60.0}Cu_{25.0}Al_{15.0}$. These results are compared to previously published results for Vit106a, Vit106, Vit105, and Vit101 from [100, 101, 103].

In the latter regime, viscosities measured using Couette, ESL, and EML rheometry will be presented for all eight of the aforementioned alloys. Due to complexity of these high temperature measurements, additional clarification of the analysis will be provided where necessary. This work was done in conjunction with the group of Prof. Meyer at the Institute of Material Physics in Space in Köln, Germany.

5.1 Kinetics near the glass transition

Conventional three point beam bending methods were applied to investigate the viscosity of the alloys near the glass transition temperature. Both isothermal and continuous heating experiments were conducted in the Netzsch TMA 402. In the former method, the samples are heated to the goal temperature at a rate of 0.33 K s^{-1} (20 K min^{-1}) and held until the sample reached equilibrium. In the former method, a constant heating rate of 0.33 K s^{-1} was applied until either the onset of crystallization or until the full range of the technique was reached (2.50 mm maximum deflection). This annealing time was shorter for higher temperatures. Viscosities were calculated according to

the Hagy equation 4.13 and the time evolution of structural relaxation was studied. Using these methods, structural relaxation can be readily characterized with a stretched exponential function such as the ubiquitous Kohlrausch-Williams-Watts (KWW) function [130, 180]

$$\phi(t) = \phi_a + \Delta\phi_{eq-a}\left(1 - exp\left[-\left(\frac{t}{\tau}\right)^{\beta}\right]\right) \tag{5.1}$$

where $\phi(t)$ is the relaxing quantity (e.g. viscosity), ϕ_a is the initial value of the relaxing quantity in the glassy state, $\Delta\phi_{eq-a}$ is the change in the relaxing quantity as equilibrium is approached (as $t \to \infty$), τ is the characteristic relaxation time, β is the stretching exponent (typically $0 < \beta < 1$), and t is the time. Mathematically, this function represents the sum of a distribution of simple exponential decays. During isothermal annealing below T_g, the viscosity increases from its initial glassy value until settling at equilibrium. Equilibrium viscosities are determined from the sum $\eta_{eq} = \eta_a + \Delta\eta_{eq-a}$.

Figure 5.1 shows results of three measurements at three select temperatures below T_g for $Zr_{59.3}Cu_{28.8}Al_{10.4}Nb_{1.5}$ (AMZ4). With increasing temperature, the equilibrium viscosities were reached at shorter times and the shape of the relaxation curve became sharper, which is reflected in the changes in the characteristic relaxation times τ and stretching exponent β as shown in figure 5.2. As $T \to T_g$, relaxation times approach the laboratory timescale and the stretching exponent tends towards unity.

Fitting with the KWW function becomes particularly challenging near T_g when relaxation times approach the laboratory timescale. Likewise, the viscosity remains at η_a longer, causing β to tend towards values greater than unity. In order to avoid over-interpretation of noise or phase separation effects, particular care must be taken when selecting the fitting constraints. Eventually, the value of η_a becomes a good approximation for the equilibrium viscosity close to T_g. Continuous heating rate scans can be useful for approximating the viscosity all the way into the supercooled liquid region. The viscosities measured during the scan below T_g correspond to the values of η_a from isothermal annealing experiments.

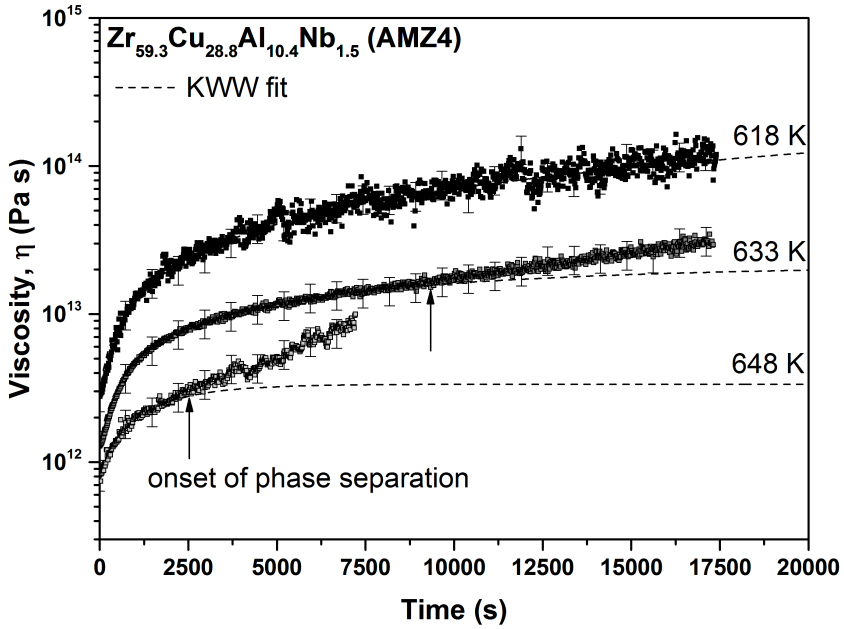

Figure 5.1: Example isothermal three point beam bending results and KWW-fitting for $Zr_{59.3}Cu_{28.8}Al_{10.4}Nb_{1.5}$ (AMZ4) at select temperatures. Arrows show the onset of phase separation. Error bars represent the instrument uncertainty (see appendix A.3)

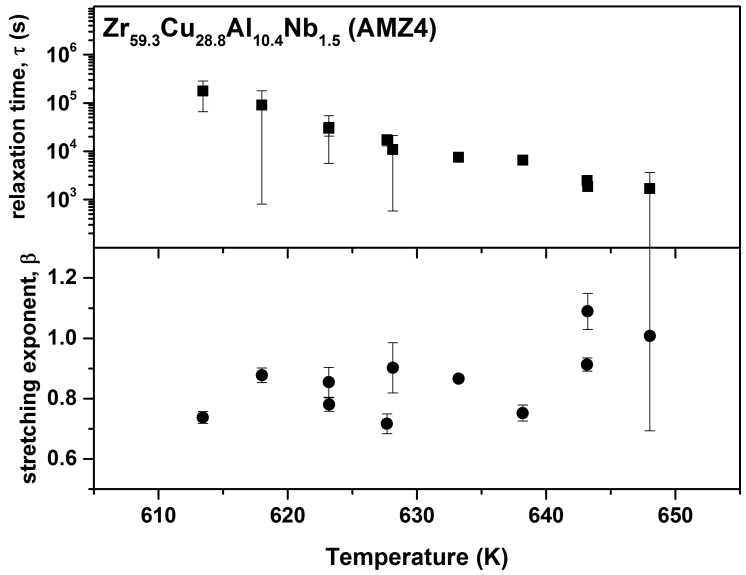

Figure 5.2: Plot of the KWW stretched exponent β and characteristic relaxation time τ for $Zr_{59.3}Cu_{28.8}Al_{10.4}Nb_{1.5}$ (AMZ4). Error bars represent fitting uncertainty.

5.1.1 Phase separation and crystallization

Investigations of the micro-structural evolution of other zirconium based BMGs near the glass transition has shown that they decompose into multiple amorphous phases which may crystallize upon further incubation. In 1997, Liu and coworkers investigated the decomposition of $Zr_{41.2}Ti_{13.8}Cu_{12.5}Ni_{10.0}$-$Be_{22.5}$ (Vit 1) during annealing below T_g using atom-prove field-ion microscopy (APFIM), small-angle neutron scattering (SANS), and transmission electron microscopy (TEM) [71]. Similarly, Löffler and coworkers investigated the decomposition of $Zr_{57.0}Cu_{15.4}Ni_{12.6}Al_{10.0}Nb_{5.0}$ (Vitreloy 106) and $Zr_{52.5}Cu_{17.9}$-$Ni_{14.6}Al_{10.0}Ti_{5.0}$ (Vitreloy 105) [69] and then later Glade and coworkers studied the copper based alloy $Cu_{47.0}Ti_{34.0}Zr_{11.0}Ni_{8.0}$ (Vitreloy 101) [70]. In all of these BMG forming alloys, clear structural evidence was found for the decomposition into different amorphous phases during annealing below the glass transition. Subsequent nano-crystallization was facilitated by the increased driving force for nucleation and crystallization in at least one of the phases. In contrast to Vit106 and Vit105, the measurements of Vit101 showed the presence of nano-crystals in the as-cast state.

Due to the compositional similarities between the alloys in this study and those in the aforementioned works, it is very likely that decomposition occurs during the isothermal annealing in the TMA and may explain some of the anomalous behavior that is observed. In all of systems studied in this work, the onset of decomposition and crystallization manifests as a deviation from equilibrium behavior up to values several orders of magnitude higher and is marked with an arrow on 5.1. This behavior is consistent with other viscosity measurements on Vitreloy 106, 106a, 105, and 101 [100, 103].

Einstein's equation for the flow of mixtures can be used to approximate the effective viscosity of some medium with a certain percentage of solid particles, given by $\eta^* = \eta\,(1 + 2.5\phi)$, where η^* is the effective viscosity of the mixture, η is the viscosity of the fluid medium, and ϕ is the volume fraction of the particles [37]. Accordingly, for a 50% volume fraction of crystals, one would expect a 225% increase in viscosity. This indicates that the measured increase in viscosity of several orders of magnitude must arise from significant compositional changes within the amorphous matrix as well as the presence of a crystalline fraction [95, 100].

5.1.2 Equilibrium viscosity

Figure 5.3 shows the summary of the three point beam bending viscosity results on an Arrhenius type plot. The open circles represent the viscosities at η_a in the glassy state, which match very well with the continuous heating scan below T_g shown as gray points. During the scan, the deflection of the beam extends beyond the limitations of the device (2.50 mm) as indicated by the "out of range" arrow on figure. The onset of the calorimetric glass transition as measured in the DSC at 0.33 K s^{-1} correlates well with the glass transition measured in the TMA. Over the course of the structural relaxation below T_g, the viscosity follows the gray arrows from the values at η_a until reaching the equilibrium liquid as indicated by the closed black squares. Fitting the equilibrium viscosity with the empirical Vogel-Fulcher-Tammann (VFT) equation yields parameters $D^* = 24.8$ ($m = 39.8$) and $T_0 = 395$ K.

Similar measurements were conducted for $Zr705_{60.8}Cu_{28.8}Al_{10.4}$ (AMZ4 705), $Zr_{65.0}Cu_{17.5}Ni_{10.0}Al_{7.5}$ and $Zr_{60.0}Cu_{25.0}Al_{15.0}$ and are shown in figures 5.4, 5.5, and 5.6, respectively. Stefan Gärtner made significant contributions to the latter two measurements and his master's thesis covers them in greater detail [110]. The results from these measurements are summarized along with those from Evenson and coworkers [100] in table 5.1. Included are the values for T_g^*, which correspond to the temperatures at which the respective VFT-fits are equal to $\eta\left(T_g^*\right) = 10^{12}$ Pa s. The values shown in this work use the corrected moment of inertia and therefore differ from those reported by Evenson et al. However, the

All of the alloys show moderately strong kinetics near the glass transition with fragility parameters of about $20 < D^* < 26$. The only two exceptions to this are Vit106 and Vit101. First, Vit106 is significantly stronger than the other alloys studied, with a $D^* = 36.9$, which is in good agreement with the value of $D^* = 35.2$ reported by Evenson [100]. Second, the Cu based Vit101 alloy is considerably more fragile than the rest of the Zr based compositions with $D^* = 16.1$, which also agrees well with the previously reported value of $D^* = 14.9$ from [100]. In contrast, all of the other alloys have remarkably similar kinetics despite notable compositional differences. Although the variant of AMZ4 made with industrial grade zirconium has a slightly lower glass forming ability and smaller supercooled liquid region than its high purity variant, both have nearly identical fragility. The fitting uncertainty of the fragility parameter is about $D^*\pm$. All values of η_0 are calculated according to $\eta_0 = hN_A/v_m$ for each alloy, where h is Plank's constant, N_A is Avogadro's number, and v_m is the atomic volume [143].

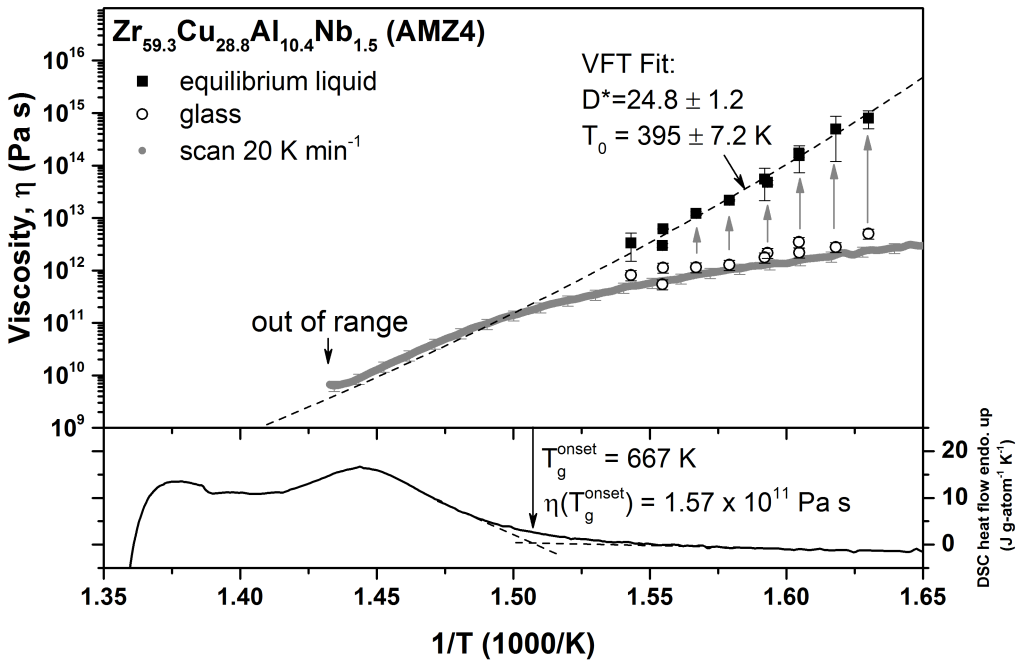

Figure 5.3: (upper) Three point beam bending viscosities and VFT-fit for $Zr_{59.3}Cu_{28.8}Al_{10.4}Nb_{1.5}$ (AMZ4); (lower) DSC scan at 0.33 K s^{-1}. The arrows show the direction of relaxation from the glass towards equilibrium.

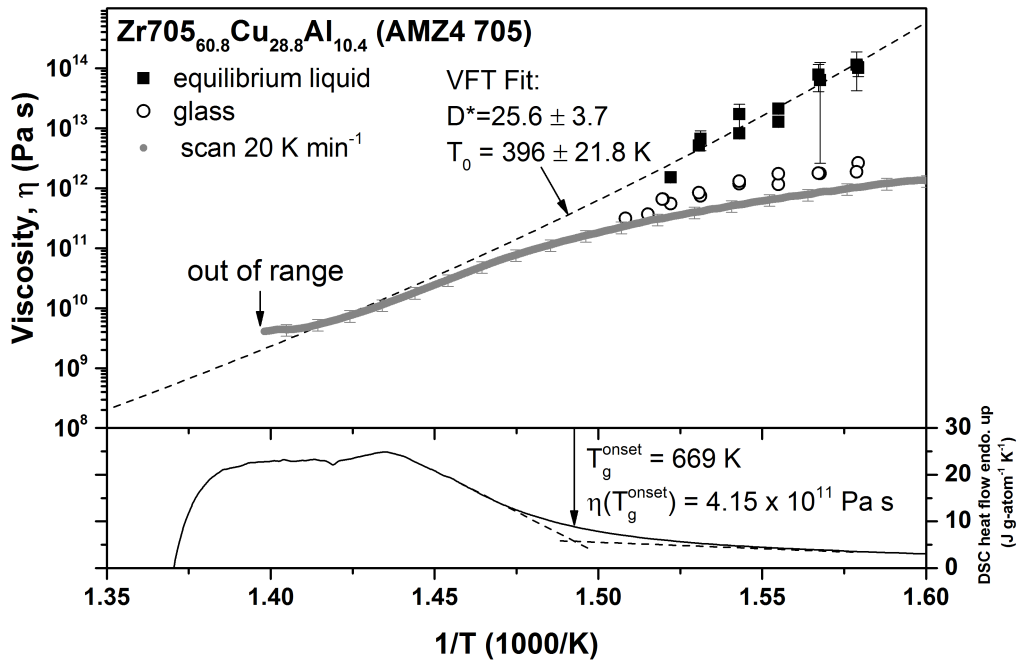

Figure 5.4: (upper) Three point beam bending viscosities and VFT-fit for $Zr705_{60.8}Cu_{28.8}Al_{10.4}$ (AMZ4 705); (lower) DSC scan at 0.33 K s^{-1}.

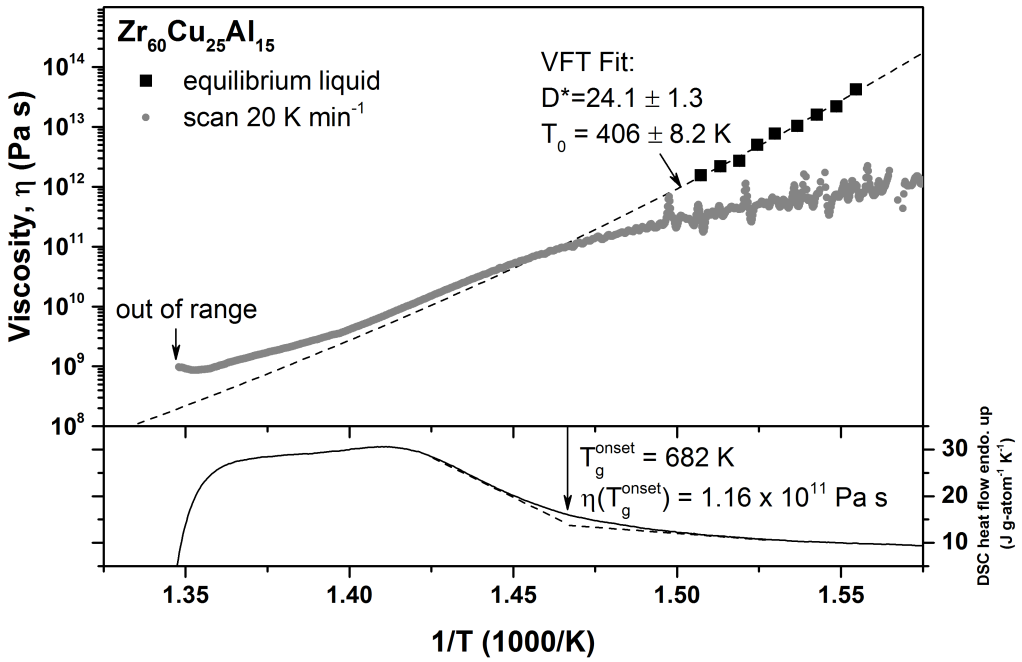

Figure 5.5: (upper) Three point beam bending viscosities and VFT-fit for $Zr_{60.0}Cu_{25.0}Al_{15.0}$; (lower) DSC scan at 0.33 K s^{-1}. Data from [110].

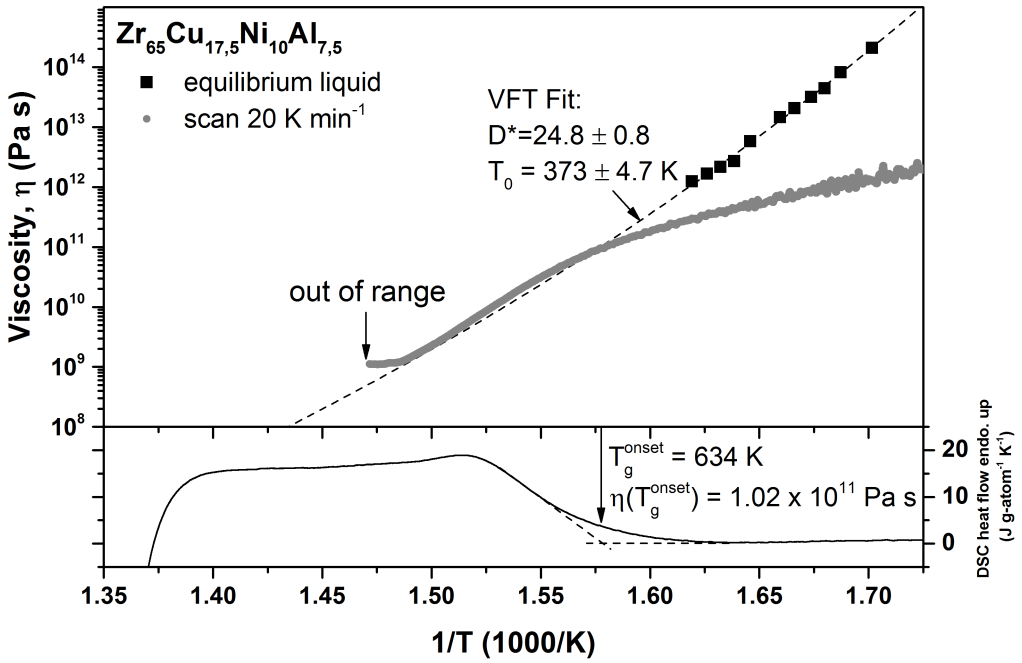

Figure 5.6: (upper) Three point beam bending viscosities and VFT-fit for $Zr_{65.0}Cu_{17.5}Ni_{10.0}Al_{7.5}$; (lower) DSC scan at 0.33 K s^{-1}. Data from [110].

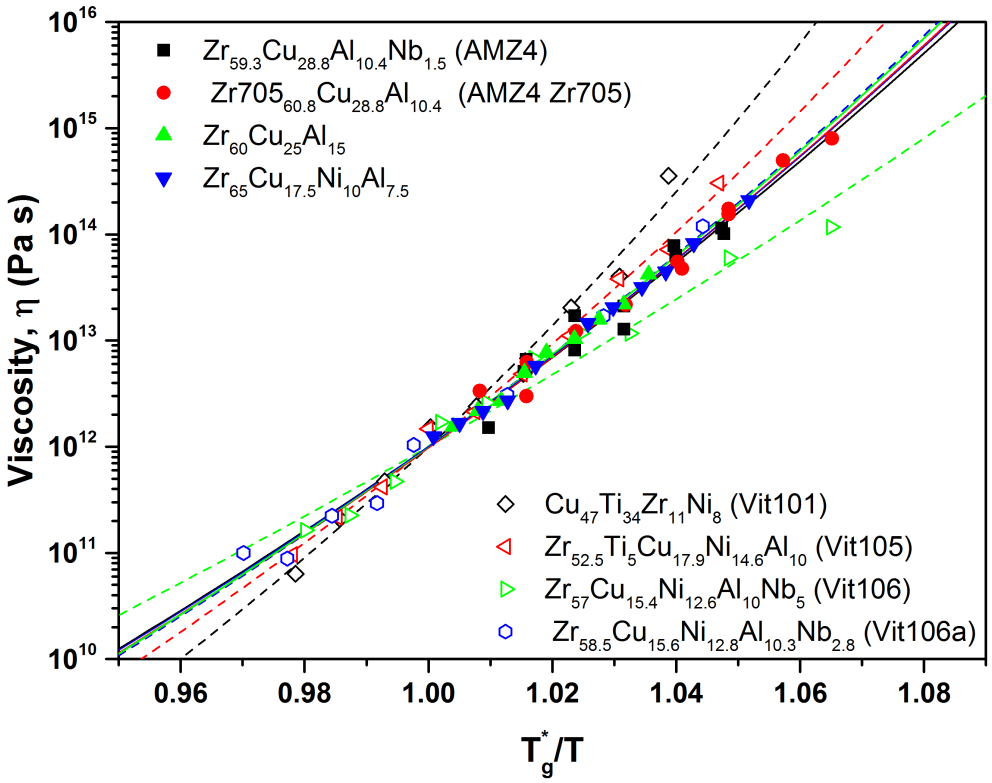

Figure 5.7: (upper) Three point beam bending equilibrium viscosities and VFT-fit for all alloys in this work. Solid symbols and full lines represent data measured in this work, and open symbols and dashed lines are corrected data from [103].

Table 5.1: TMA Vogel Fulcher Tammann fitting parameters

Composition (at%)	D*	T_0 (K)	m	T_g^* (K)	T_g^{cal} (K)
$Zr_{59.3}Cu_{28.8}Al_{10.4}Nb_{1.5}$ (AMZ4)	24.8	395	39.8	653	667[a]
$Zr705_{60.8}Cu_{28.8}Al_{10.4}$ (AMZ4 705)	25.6	396	39.0	663	669[a]
$Zr_{60.0}Cu_{25.0}Al_{15.0}$	24.1	406	40.5	665	682[a]
$Zr_{65.0}Cu_{17.5}Ni_{10.0}Al_{7.5}$	24.8	373	39.8	618	634[a]
$Zr_{58.5}Cu_{15.6}Ni_{12.8}Al_{10.3}Nb_{2.8}$ (Vit106a)	24.1	409	40.5	669	671[b]
$Zr_{57.0}Cu_{15.4}Ni_{12.6}Al_{10.0}Nb_{5.0}$ (Vit106)	36.9	343	32.0	676	673[b]
$Zr_{52.5}Cu_{17.9}Ni_{14.6}Al_{10.0}Ti_{5.0}$ (Vit105)	20.5	435	44.8	670	675[c]
$Cu_{47.0}Ti_{34.0}Zr_{11.0}Ni_{8.0}$ (Vit101)	16.1	473	52.6	674	673[c]

(a) This work, $q_H = 0.333$ K s^{-1}
(b) [103] $q_H = 0.25$ K s^{-1}
(c) [93] $q_H = 0.333$ K s^{-1}

5.2 Kinetics near the melting point

In this section, the results from the high temperature rheological measurements will be presented along with a brief explanation of the analysis. All eight of the alloys in this study were investigated using high temperature Couette rheology as well as with the oscillating droplet technique in EML and ESL facilities. Viscosities were measured near T_{liq} for all of the samples according to the methods outlined in chapter 4.

5.2.1 Couette rheometer

Investigations of the temperature dependent viscosities above T_{liq} are greatly expedited by the changes to the program and apparatus as described in chapter 3. Due to the improvements to the PID-temperature controller, it is now possible to take measurements in controlled cooling and heating and as a result, a much greater number of data points can be collected as a function of temperature.

Figure 5.8 shows example raw data for a Couette measurement of Vit106a to highlight the standard measurement protocol in this apparatus. The sample is first melted and heated to some maximum temperature (1373 K in this case). After ensuring that the temperature equilibrates and that samples are free of bubbles or solid obstructions (e.g. slag), the motor is operated in an stepwise profile with a pre-defined maximum shear rate and acceleration. The torque sensor automatically records the reaction moment on the cup and zeros the signal after every complete motor step.

At very high temperatures, the recorded torque is very small compared to the shear rate, corresponding to an extremely low viscosity (figure 5.8a). Once the temperature approaches T_{liq}, the increase in viscosity manifests as a directly proportional rise in the measured torque (figure 5.8b). The torque signal noise can be attributed to mechanical vibrations from the motor and remains nearly constant at any given maximum shear rate. At low viscosities, however, this noise is larger than the magnitude of the reaction moment due to viscous shearing and should not be neglected.

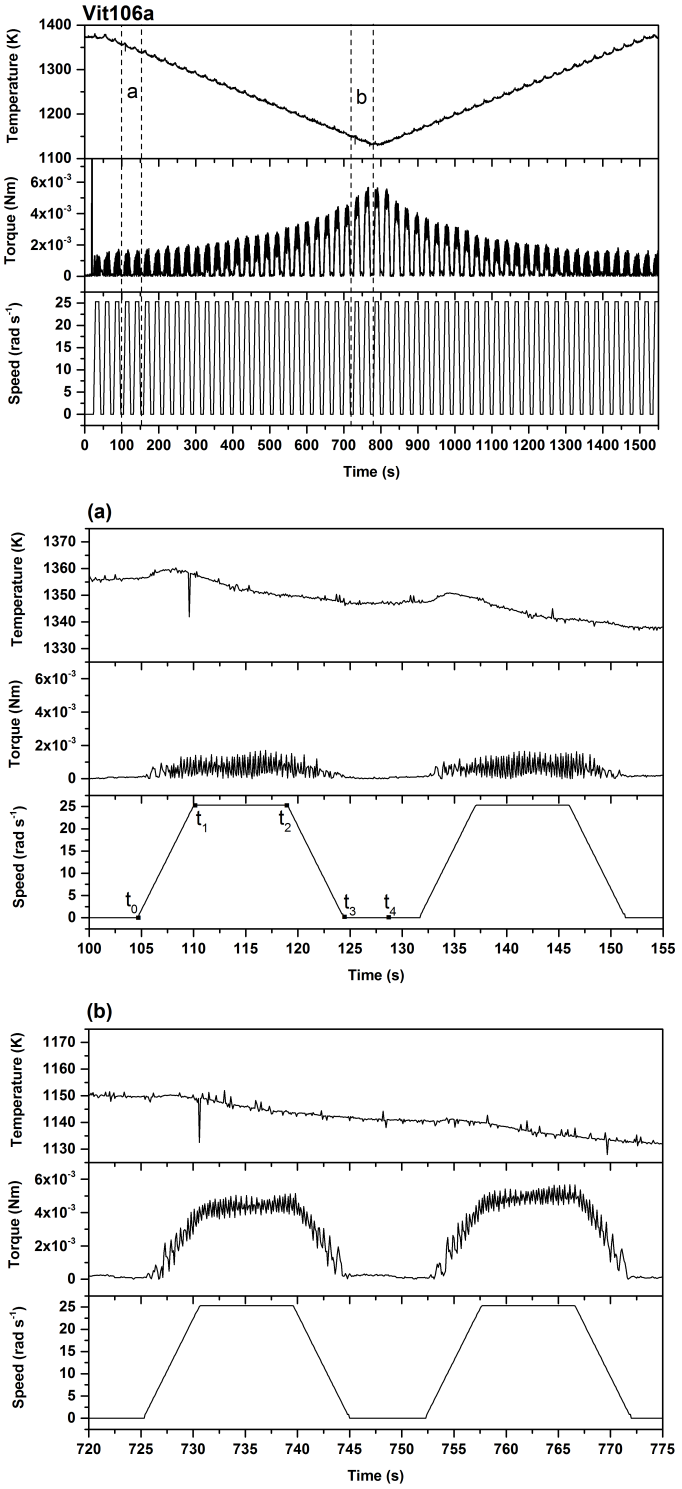

Figure 5.8: (upper) example plot of the measured temperature, torque, and speed of a full cycle in the Couette rheometer for Vit106a with $|q_H| = |q_C| = 20$ K min^{-1} and a maximum shear rate of $\dot{\gamma} = 456$ s^{-1}. (a) expanded view of the high temperature regime showing the time indices t_{0-4} required for the LabVIEW program to calculate the viscosity, (b) expanded view of the low temperature regime.

The time indices for the viscosity calculation are shown in figure 5.8a as points t_{0-4}. These indices correspond to the points at which the motor status is set to *running* and has velocities that are initially zero t_0, non-zero with no acceleration t_1, non-zero with deceleration t_2, zero after deceleration t_3, and the last index before the sensor zeros itself t_4. At any given step, the reaction moment is calculated as

$$\bar{M} = \bar{M}|_{t_1}^{t_2} - \bar{M}|_{t_3}^{t_4} \tag{5.2}$$

Note that the index t_0 is not used in this calculation but is still necessary for defining the measurement start as well as for programmatically determining the shear thinning exponent. Similarly, the temperature is averaged between indices t_1 and t_2. Uncertainty in the temperature is determined from the standard deviation from the average at each step within the bounds of the respective time indices. By doing so, this includes any rise due to shear heating that typically manifests as a slight temperature increase during acceleration. Meanwhile, uncertainty in the viscosity is calculated according to the instrumental error as summarized in appendix A.2 and as explained in [122].

From the raw data, the representative viscosity is then calculated according to

$$\eta_{rep} = \frac{R_o^2 - R_i^2}{4\pi L R_o^2 R_i^2 c_L} \cdot \frac{\bar{M}}{\omega} \tag{5.3}$$

where R_o is the interior radius of the cup, R_i is the radius of the bob, L is the immersion depth, c_L is a correction length that accounts for the tapered end of the bob ($c_L = 1.015$ for this study), and ω is the radial velocity of the bob in $rads/s$. The left fraction can be considered a geometric constant if all of the relevant variables remain the same for an experiment and the fluid behaves in a Newtonian manner.

This method produced very reliable and reproducible measurements of the viscosity, as demonstrated in figure 5.9 for three separate measurements of Vit106a at shear rates of $\dot{\gamma}_3 = 452\ \mathrm{s}^{-1}$. These results show remarkable agreement despite the coming from different batches and from using different sensor calibrations. The only notable difference comes from the measurement on 10.04.14, which was cooled all the way down to below T_{liq} and showed a pronounced increase in apparent viscosity which was reversible upon subsequent reheating above T_{liq}.

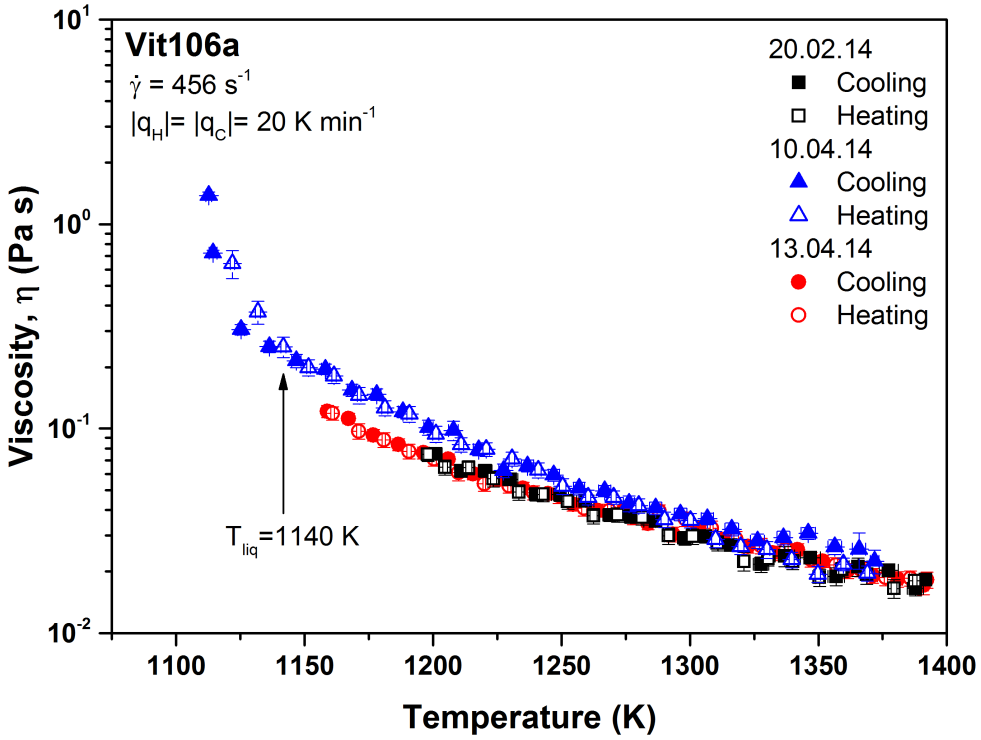

Figure 5.9: Couette results from three separate measurements at $\dot{\gamma} = 452$ s^{-1} using the same method as shown in figure 5.8. In the second experiment, undercooling was limited to approx. 30 K below T_{liq}, which was accompanied by a pronounced increase in apparent viscosity. The two experiments that never dropped below T_{liq} showed no anomalous behavior.

The high temperature viscosities measured in the Couette rheometer are summarized for all eight alloys in this study in figures 5.11 through 5.18. Each data set is plotted together with the VFT-fit of the viscosities at shear rates of $\dot{\gamma} = 452$ s^{-1}, and the parameters are summarized in table 5.2. These fits ignore the data points where the apparent viscosity increases due to crystallization and are constrained at high temperatures close to T_g in accordance with the method used previously [101, 103].

Large measurement errors are evident in Vit101 (figure 5.14) and $Zr_{65.0}$-$Cu_{17.5}Ni_{10.0}Al_{7.5}$ (figure 5.18). These liquids have relatively low viscosities near the nominal sensor resolution. This is exacerbated at low shear rates, where the viscous forces insufficient for stabilization of the bob under eccentric conditions. As it stands, this is the most significant remaining design flaw in the Couette rheometer. The mechanical instabilities of the current apparatus will severely inhibit attempts to gain access to lower viscosities. This is discussed in further detail at the end of this section.

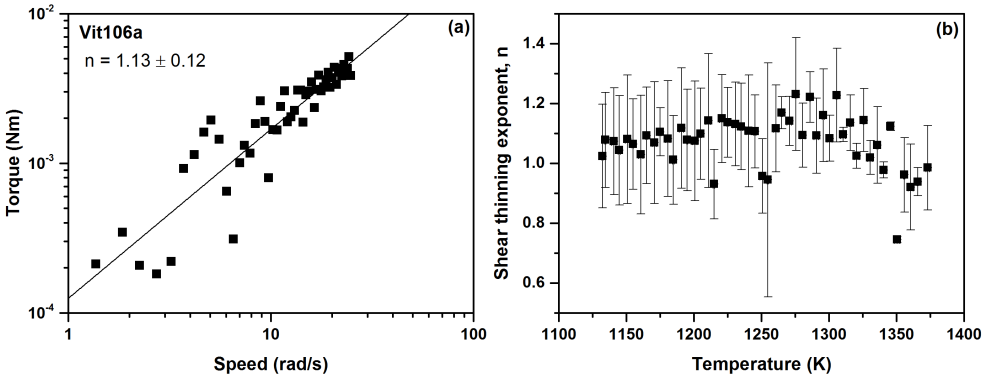

Figure 5.10: (a) The shear thinning exponent is determined from the slope of a linear fit of the double logarithmic plot of torque versus bob speed. (b) Summary of the shear thinning exponent for Vit106a using this method.

The results agree very well with previous investigations of the same alloy systems, where the fragility parameter is $D^* \approx 10$ for the Zr-based alloys and slightly lower for the Cu-based Vit101, which has a $D^* = 6.3$. These liquids behave as fragile liquids above the melting point, which is not only in good agreement with previous investigations but supports the idea of the Strong-Fragile transition. However, no direct observation of the the transition was observed.

Contrary to Couette viscosity experiments on Vit1 [47], no evidence for shear-thinning was found in any of the alloys. The deviation seen in the shear rates is within the experimental uncertainty and cannot be attributed to the destruction of order within the melt or the onset of a Strong-Fragile transition. A closer investigation of the shear thinning exponent n across a wider range of shear rates is shown as an example for Vi106a in figure 5.10. The shear thinning exponent is determined programmatically within LabVIEW by finding the slope of a linear fit of the logarithmic torque versus logarithmic bob speed. The results show that the value of $n \approx 1$ remains nearly constant across the entire measurement range. This method, however, is significantly hindered by instabilities at low shear rates which cause large errors and a tendency to shift n to higher values. Similar observations are made for the other alloys in this study. This is in good agreement with the findings of Evenson and coworkers [101].

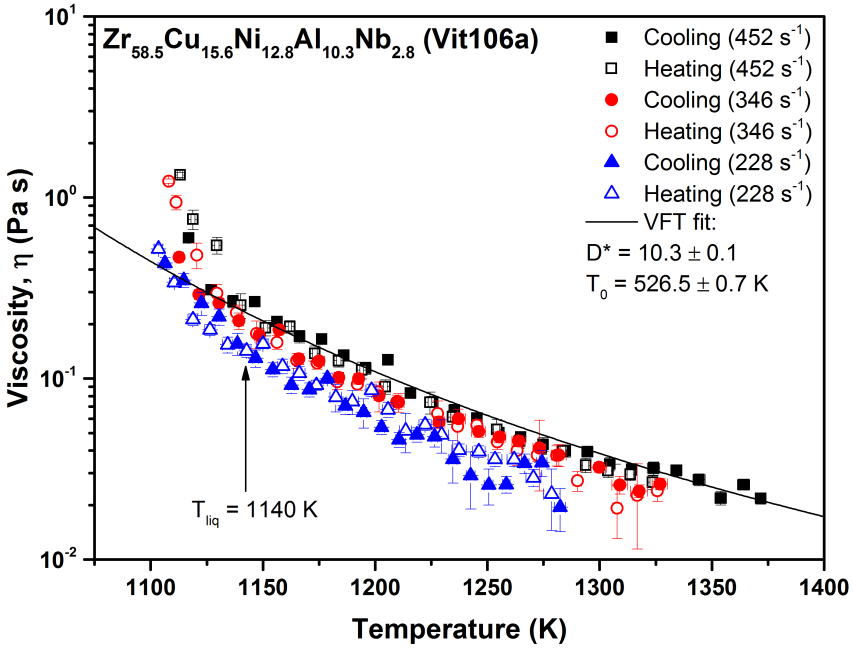

Figure 5.11: Couette viscosity results and the corresponding VFT-fit for Vit106a at three shear rates and $|q_H| = |q_C| = 20$ K min^{-1}

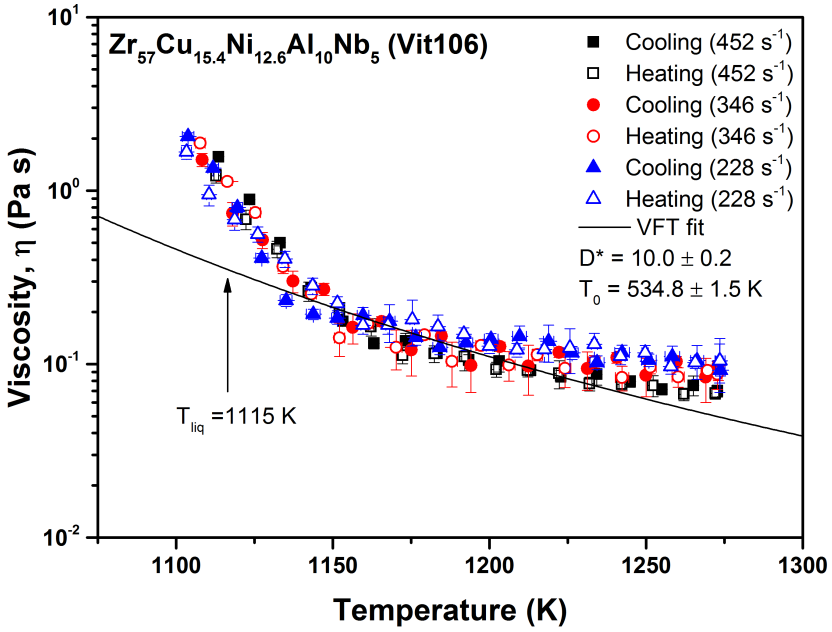

Figure 5.12: Couette viscosity results and the corresponding VFT-fit for Vit106 at three shear rates and $|q_H| = |q_C| = 20$ K min^{-1}

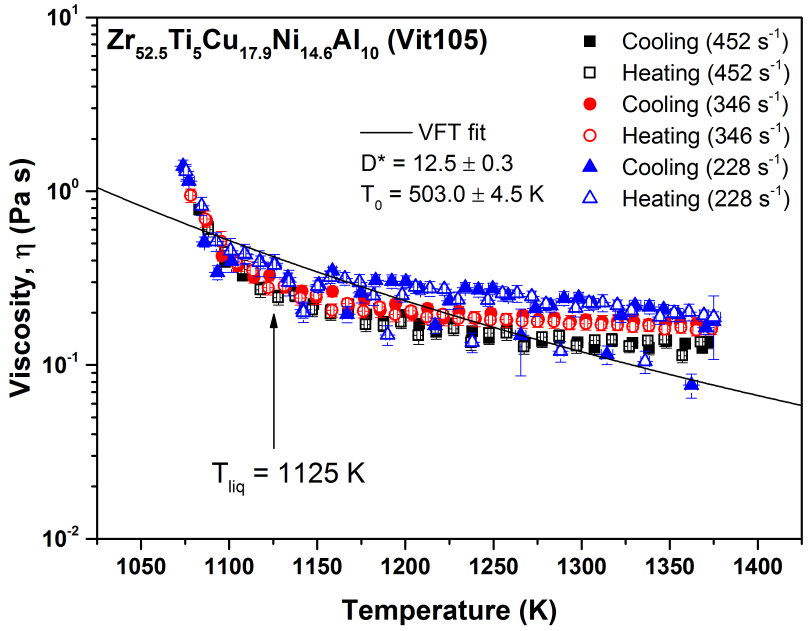

Figure 5.13: Couette viscosity results and the corresponding VFT-fit for Vit105 at three shear rates and $|q_H| = |q_C| = 20$ K min^{-1}

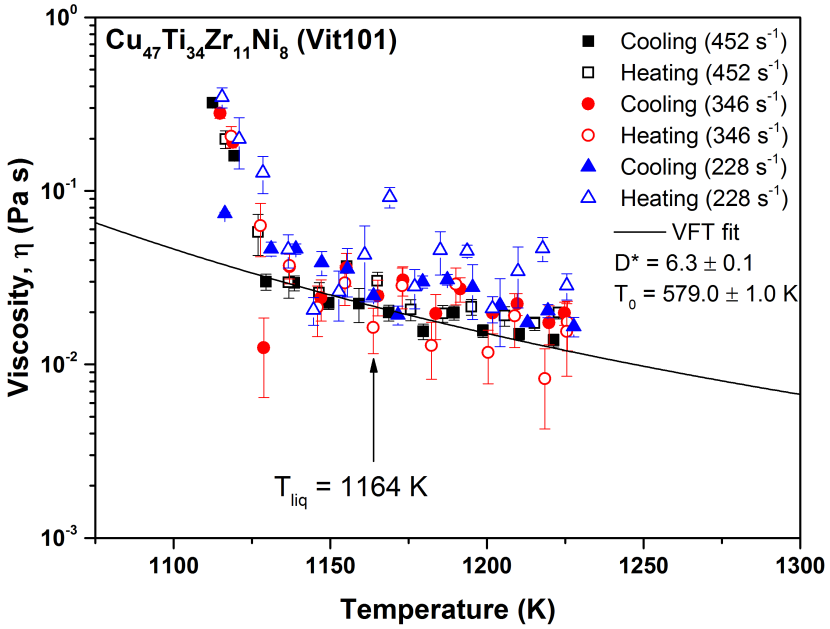

Figure 5.14: Couette viscosity results and the corresponding VFT-fit for Vit101 at three shear rates and $|q_H| = |q_C| = 20$ K min^{-1}

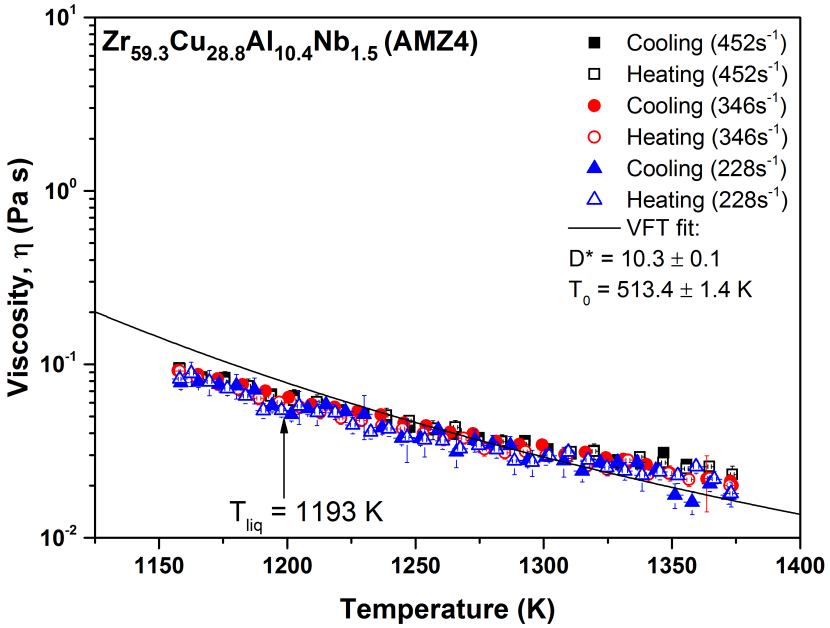

Figure 5.15: Couette viscosity results and the corresponding VFT-fit for AMZ4 at three shear rates and $|q_H| = |q_C| = 20$ K min^{-1}

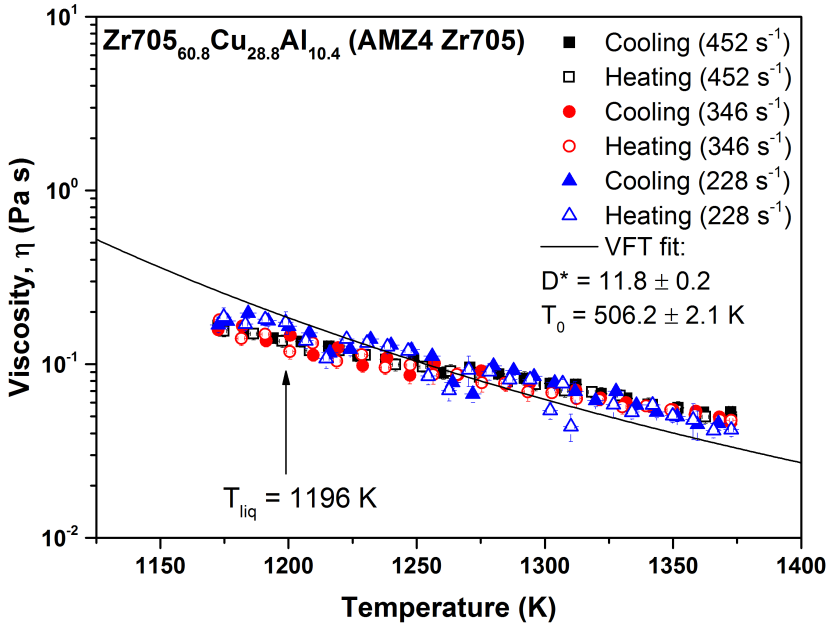

Figure 5.16: Couette viscosity results and the corresponding VFT-fit for AMZ4 Zr705 at three shear rates and $|q_H| = |q_C| = 20$ K min^{-1}

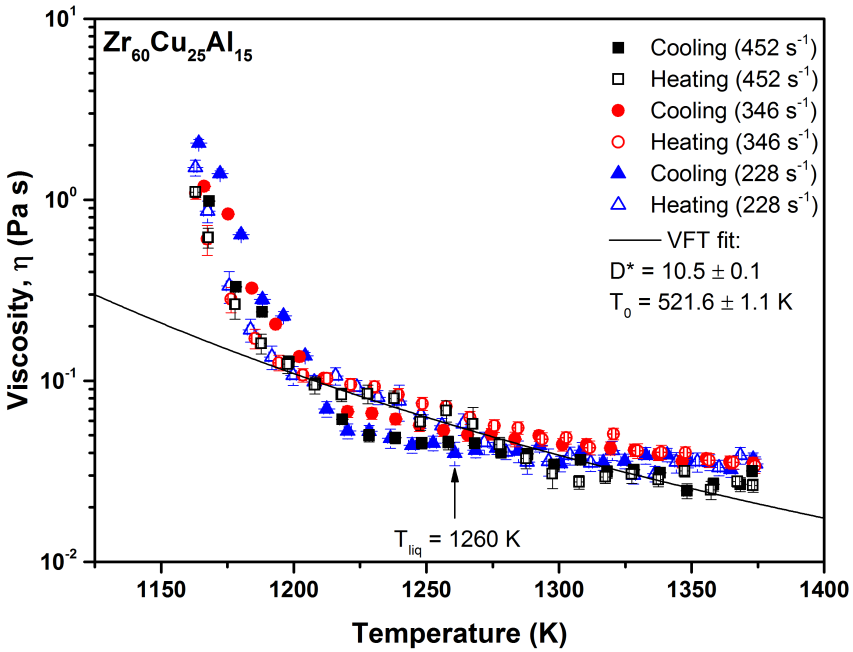

Figure 5.17: Couette viscosity results and the corresponding VFT-fit for $Zr_{60.0}$-$Cu_{25.0}Al_{15.0}$ at three shear rates and $|q_H| = |q_C| = 20$ K min^{-1}

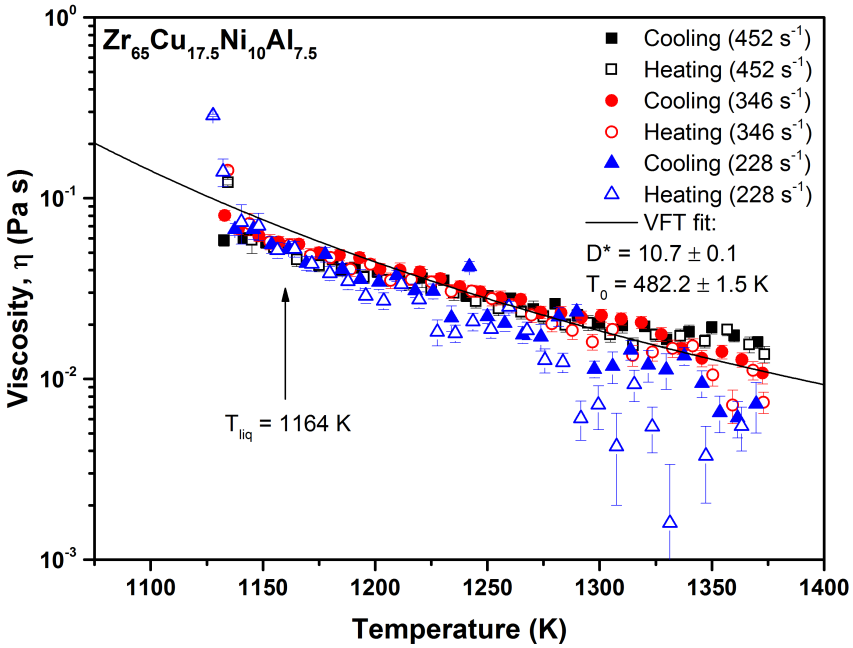

Figure 5.18: Couette viscosity results and the corresponding VFT-fit for $Zr_{65.0}$-$Cu_{17.5}Ni_{10.0}Al_{7.5}$ at three shear rates and $|q_H| = |q_C| = 20$ K min^{-1}

Table 5.2: High temperature viscosity parameters

Composition (at%)	D*	T_0 (K)	m	$\eta\,(T_{liq})$ (Pa s)
$Zr_{59.3}Cu_{28.8}Al_{10.4}Nb_{1.5}$ (AMZ4)	10.3	513	73.3	0.083
$Zr705_{60.8}Cu_{28.8}Al_{10.4}$ (AMZ4 705)	11.8	505.2	66.0	0.190
$Zr_{60.0}Cu_{25.0}Al_{15.0}$	10.5	521.6	72.2	0.057
$Zr_{65.0}Cu_{17.5}Ni_{10.0}Al_{7.5}$	10.7	482.2	71.1	0.066
$Zr_{58.5}Cu_{15.6}Ni_{12.8}Al_{10.3}Nb_{2.8}$ (Vit106a)	10.3	527	73.3	0.240
$Zr_{57.0}Cu_{15.4}Ni_{12.6}Al_{10.0}Nb_{5.0}$ (Vit106)	10.0	535	75.0	0.351
$Zr_{52.5}Cu_{17.9}Ni_{14.6}Al_{10.0}Ti_{5.0}$ (Vit105)	12.5	503	63.2	0.881
$Cu_{47.0}Ti_{34.0}Zr_{11.0}Ni_{8.0}$ (Vit101)	6.3	579	109.7	0.023

Figure 5.19 summarizes the measured viscosities from all eight compositions in an Angell plot. In the cases of Vit106a, Vit106, and Vit101, the data matches previous measurements from Evenson and coworkers [101] (shown as open symbols on the same plot). In the case of Vit105, however, the most recent measurement deviates significantly from the behavior expected from the rest of the compositions and has a nearly constant viscosity. Rather than being a physical effect, this is most likely due to experimental error during the measurement such as the entrapment of an Argon bubble under the bob. Despite this aberration, the absolute viscosity at the melting point is consistent with the expectations for these multicomponent metallic liquids. In the case of Vit101, measurements at higher temperatures were not feasible because the viscosity was very close to the lower limit of the sensor. The comparatively low viscosity of Vit101 is also reflected in the measurements from [101].

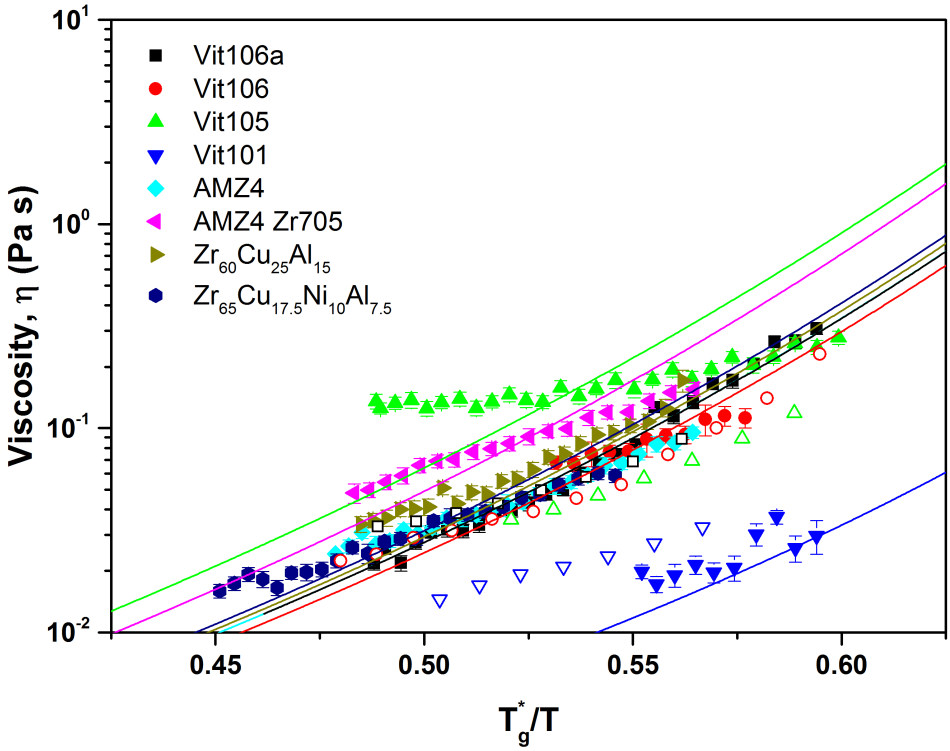

Figure 5.19: Couette viscosity results for the eight compositions in this study (solid symbols) and those measured from Evenson et al. (open symbols) [101]. The increase in apparent viscosity due to crystallization is not shown for clarity.

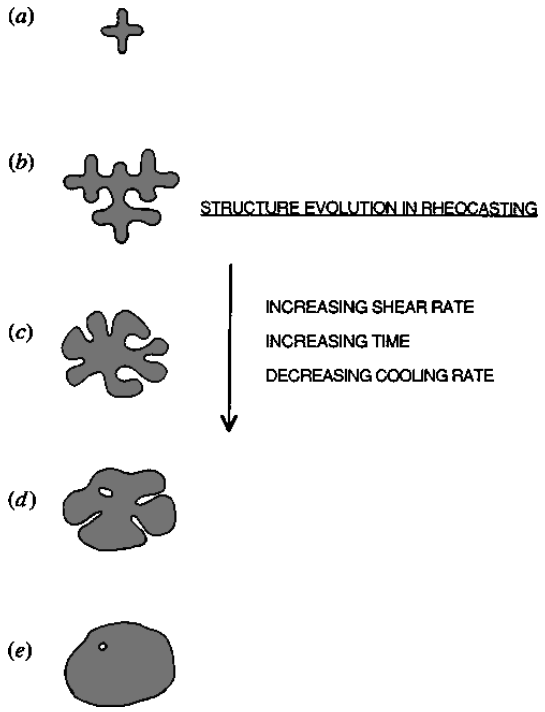

Figure 5.20: Illustration of the structural changes during solidification under shear agitation,(a) dendrite, (b) dendrite growth, (c) rosette, (d) rosette ripening, (e) spheroid. Figure adapted from [105].

Crystallization in the Couette rheometer

An increase in apparent viscosity of about one order of magnitude occurs after undercooling below T_{liq} for nearly all of the alloys in this study. The only exception to this was the two AMZ4 variants, whose crystallization immediately caused overloading of the sensor and are not shown. This is attributed to entering the liquid-solid zone and the onset of heterogeneous nucleation of crystals. Solidification of metallic alloys typically initiates either through dendritic or eutectic morphologies. Columnar dendrites tend to grow at the interface between the melt and the container walls, where the wall acts as the primary heat sink. Equiaxed dendrites form within the melt in the event that the liquid acts as the heat sink. In the case of dendritic solidification under sufficient shear stresses, the dendrites will break apart or deform into "rosette" structures. Further cooling allows the ripening of these rounded particles, which will form "spheroids" if the cooling rate is slow enough or the shearing is high enough [105]. This is shown schematically in figure 5.20.

The rheology of various semi-solid slurries has been studied by Spencer and Flemings using a toothed Couette rheometer [44, 105]. They found that under continuously cooling and constant application of shear stresses, the formation of dendrites in metallic alloys can be disturbed and the material behaves as

a liquid-like slurry. Industrially, this is useful for grain refinement in casting operations of conventional alloys and has been commercialized through so-called *rheocasting* alloys and operations.

The rest time between shearing increases the chance that the solid particles will agglomerate, resulting in a drastic increase in the apparent shear stresses required to break them apart [96]. In other words, the melt will exhibit both time-dependent (thixotropic) as well as shear rate-dependent (pseudoplastic) behavior under these conditions. Within this regime, the apparent viscosity is a function of the shear rate, solid fraction of particles, the morphology of the particles, and the degree of agglomeration [105].

Alloys that have been processed in this manner typically display some hysteresis on reheating because the distribution and size of the semi-solid fraction depends on the shearing and thermal history. This was independently corroborated by the works of Liu [96] and Spencer [44], who both used Couette devices. Similar behavior is seen in all of the alloys studied here. Typically, values on cooling below T_{liq} are lower than those after subsequent heating. Upon further heating, these values return to equilibrium above T_{liq}.

For dilute suspensions of spherical solid particles, the apparent viscosity η^* can be calculated according to Einstein's equation

$$\eta^* = \eta\,(1 + B\phi) \tag{5.4}$$

where ϕ is the volume fraction of the solid phase and B is the intrinsic viscosity or "Einstein coefficient", which was derived as $B = 2.5$ [36]. The precise value of B has been the subject of some debate, but is typically taken between $1.5 \leq B \leq 5$ [90]. It has been demonstrated that equation 5.4 is only valid for very dilute suspensions and offers a poor estimate of the viscosity at the higher solid fractions where particle-particle interactions dominate [90,149]. There have been several attempts to expand on Einstein's equation through polynomial expressions of the form $\eta^*/\eta = 1 + B_0\phi + B_1\phi^2 + \cdots$ by Guth and Gold [118], Vand [173], and Manley and Mason [136]. However, these predictions fail for values of $\phi > 0.25$ [149] where non-Newtonian behavior begins. Furthermore, as the suspensions reach a maximum packing density.

In the semisolid alloys studied by Spencer and Flemings, once the solid fraction reached approximately 40%, the apparent viscosity rapidly increased several orders of magnitude, deviating significantly from the predictions from equation 5.4. This is, however, consistent with the predictions according to the Krieger relation [98, 132]

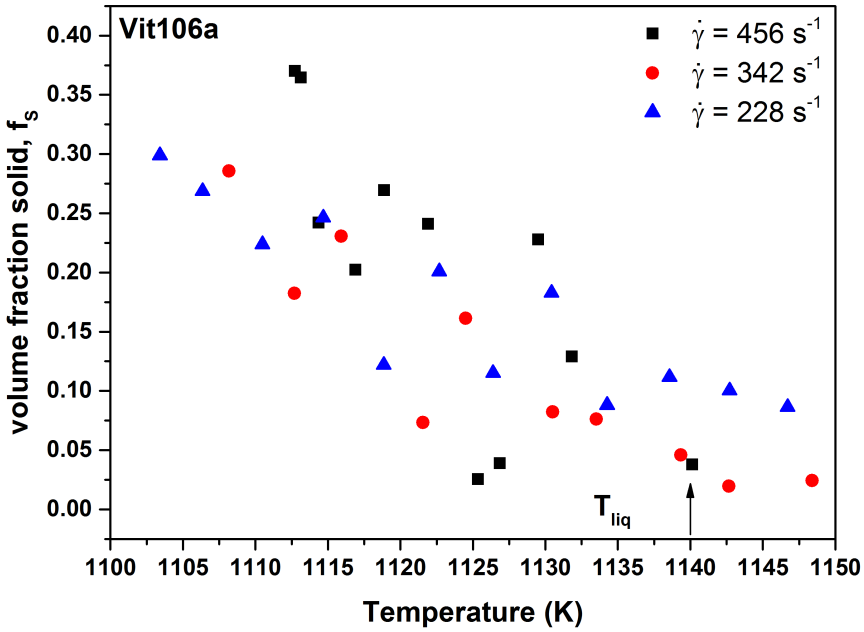

Figure 5.21: Plot of the solid fraction upon undercooling below T_{liq} for Vit106a obtained through the Krieger relation.

$$\eta^* = \eta_0 \left(1 - \frac{\phi}{\phi_c}\right)^{-B\phi_c} \tag{5.5}$$

where ϕ_c is the critical packing fraction ($\phi_c = 0.64$), η_0 is the viscosity of the medium, and B is once again defined as $B = 2.5$. In this model, the viscosity correctly approaches infinity in the limits as $\phi \to \phi_c$. By extending the equilibrium value of η_0 to the range of the anomalous rise in viscosity, the crystalline fraction can be estimated simply by rearranging equation 5.5 to solve for ϕ at any given data point where η^* is known. To estimate the value of eta_0 below T_{liq}, the fitting of the high temperature data with the Vogel-Fulcher-Tammann equation was extrapolated to low temperatures.

The results from applying this method to the data shown in figure 5.9 for Vit106a at three shear rates, $\dot{\gamma} = 228$ s^{-1}, 346s^{-1}, and 452s^{-1} are summarized in figure 5.21. A clear monotonic increase in the solid fraction with undercooling is observed at all three shear rates. The magnitude of the solid fraction does not differ significantly among the shear rates at any given temperature and remains within the scatter of the data available. The maximum solid fraction obtained is about 37% at 1113 K and a shear rate of $\dot{\gamma} = 452$s^{-1}, which is in good agreement with the observations from Flemings and coworkers [44, 105]. Applying this method to the other alloys in this study brings similar results.

One reservation with this method, however, is that the Krieger relation is only valid for monodisperse (i.e. one size) and perfectly spherical particles within an unchanging liquid. Various models have been made specifically for polydisperse and non-spherical particles but require knowledge about the distribution and shape of the dispersions [16, 98]. Ex-situ microscopy of the shear cell cross sections does not provide a reliable means of estimating the particle size and shape due to the likelihood of grain growth as the system cools to room temperature, which may take up to several hours after the conclusion of an experiment.

Yet another important consideration with this analysis is that it neglects the impact that compositional changes from solute diffusion within the melt below T_{liq} may have on the viscosity. For binary metallic solutions, the solid fraction f_S is related to the composition according to the Gulliver-Scheil equation,

$$f_S = 1 - \left(\frac{T_M - T_L}{T_M - T} \right)^{\frac{1}{1-k}} \tag{5.6}$$

where T_M is the melting temperature of the pure solvent, T_L is the liquidus temperature, and the partition coefficient $k = C_0/C_L$ is determined from the steady state solid composition C_0 and the composition of the liquid C_L. This relation, however, breaks down under transient conditions where melt convection and the motion of crystalline particles are non-trivial. Furthermore, accurate phase diagrams are a prerequisite for Scheil analysis for kinetic calculations and it does not accurately represent solute diffusion for multicomponent systems. However, as previously suggested [95, 100], it is very likely that any compositional changes within the melt will also have a direct influence on the viscosity.

Both the Einstein rule of mixtures and the Krieger relation assume that the particle size is negligible compared to the dimensions of the apparatus. Once this breaks down, then the interactions between the walls and the particles must also be accounted for. Due to the overload limit of the Couette apparatus in this study, if the particles exceed some critical size, they will obstruct the motion of the bob and overload the sensor.

Couette mechanical instabilities

If the eccentric motion of the bob is no longer stabilized by the restoring viscous forces, then the measurement uncertainty increases drastically and is prone to instrument bias. This typically occurs in materials with very low absolute viscosities, such as Vit101 and $Zr_{65.0}Cu_{17.5}Ni_{10.0}Al_{7.5}$. According to equation 3.27, a Newtonian fluid will exert a force normal to the bob that is coincident with the vertical axes of the bob and cup. In the event of eccentricities, these two axes are separated and a force that is linearly proportional to the angular velocity of the bob acts to reduce this distance. This is shown clearly in the Couette results for both of the aforementioned alloys as a large measurement scatter at 228 s^{-1} that becomes smaller at higher shear rates (figures 5.14 and 5.18, respectively).

The source of this mechanical instability is a design flaw which is only apparent at high temperatures. The cup, bob, cotter pins, and corresponding shafts adhere to H7/h6 tolerances according to the ISO-286-1:2010 standards. Accordingly, the maximum deviation in size between the shaft and hole dimensions are +0.015mm larger and −0mm smaller (see figure 5.22). During assembly at room temperature, this allows for adequate locational clearance and fits that are tight enough to minimize eccentricities. At high temperatures, however, the difference in thermal expansion of the graphite shear cell and stainless steel shafts causes the tolerances to loosen. The length change through thermal expansion is given by $\Delta L = L_0 \alpha \Delta T$, where L_0 is the initial dimension, α is the linear thermal expansion coefficient, and ΔT is the change in temperature. Accordingly, the diameter of the cup shank at 1293 K (or 1000 K above room temperature at 20°C) will expand by 0.047 mm ($\alpha_{graphite} = 4.7 \times 10^{-6}$ K^{-1}), while the hole in the austenitic stainless steel shaft will expand by 0.288 mm ($\alpha_{steel} = 28.8 \times 10^{-6}$ K^{-1}). Thus, in the measurement range of the systems investigated here, the space between the graphite and shaft will open up by 0.241 mm (0.226 mm, allowing for the maximum tolerance). Therefore, eccentricities at high temperatures are principally due to thermal expansion as a consequence of the design of the shear cell assembly.

The simplest solution to this problem is through a different choice in materials for the shaft. Molybdenum, for example, has a very similar thermal expansion coefficient compared to graphite ($\alpha_{Mo} = 5.0 \times 10^{-6}$ K^{-1}). Therefore, substituting the stainless steel shafts with Molybdenum shafts would result in an expansion of only 0.003 mm, which is still within acceptable tolerances. Therefore, there would be a minimal gap even at high temperatures.

If that method is not enough, a more complicated solution would be to use a high temperature split ring to fill the gap between the shear cell and shaft. In this method, an additional ring made from a material with a greater

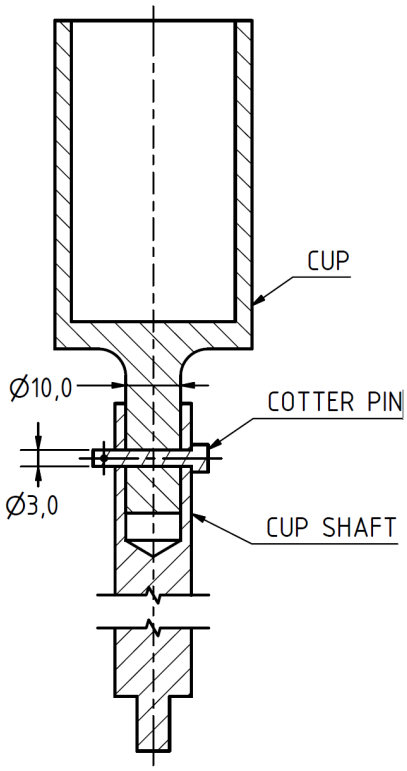

Figure 5.22: Technical drawing of the lower shear cell subassembly, with the cup, shaft, and cotter pin labeled.

thermal expansion coefficient than either the shaft or the shear cell is fitted between them. With a known inner radius, the outer radius of the ring can be calculated according to

$$r_{outer} = r_{inner} \left(\frac{\alpha_{shearcell} - \alpha_{ring}}{\alpha_{shaft} - \alpha_{ring}} \right) \tag{5.7}$$

Stainless steel is an ideal material for the ring since it has a relatively high thermal expansion coefficient. As previously demonstrated, substituting the shaft material with Molybdenum ensures a minimal expansion. For an inner diameter of 10 mm, the stainless steel ring should have an outer diameter of 10.126 mm. The hole in the Molybdenum shaft would have a H7/h6 hole to accommodate this ring. The ring should be split along its length in order to relieve stresses since it applies a pressure on both the shaft and shear cell shank. More information can be found in patent [154], which describes a similar invention for supporting a ceramic turbine rotor shaft.

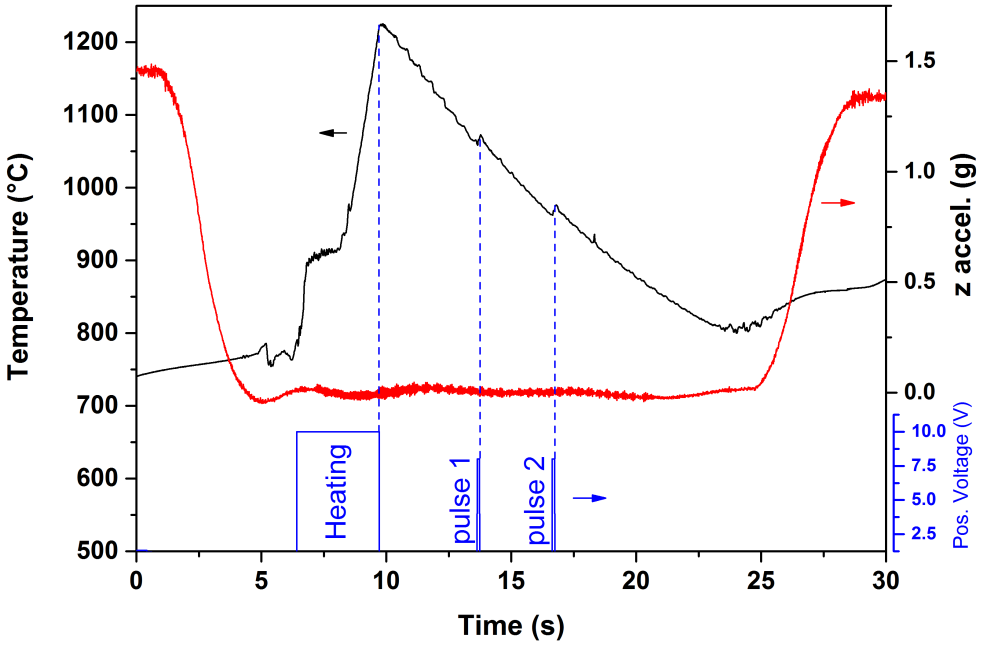

Figure 5.23: Plot showing the measured temperature, vertical acceleration, and heating field voltage for one of the parabolas flown for AMZ4.

5.2.2 Containerless measurements

In order to validate the Couette viscometer measurements, containerless viscosity measurements were performed in both an electrostatic levitation (ESL) and electromagnetic levitation (EML) devices. This section will summarize the results of those measurements as well as clarify some of the unique challenges and opportunities afforded by these techniques. Both measurements were part of an ongoing cooperation [19, 20] with the Institute of Material Physics in Space located in Cologne, Germany. The ESL results presented are provided courtesy of Isabell Jonas and more details can be found in her doctoral thesis [128]. Meanwhile, the EML measurements were conducted in the TEMPUS microgravity facility onboard the Novespace parabolic flight campaigns operated by Centre National d'Etudes Spatiales (CNES). This section will focus on the latter set of measurements, which were conducted for both variants of AMZ4.

These techniques rely on the oscillating droplet method for determining the viscosity. Recorded images of the sample projection serve as the primary raw data, which are synchronized along with the pyrometer temperature, magnetic field voltage, and data from the flight accelerometer. The high speed camera operates at 200 Hz and has a resolution of 590×600 pixels. Figure 5.23 shows the recorded secondary data for a single parabola. Each parabola consists of approximately 22 seconds of $a_z = 0 \pm 0.03$ g, during which the sample must

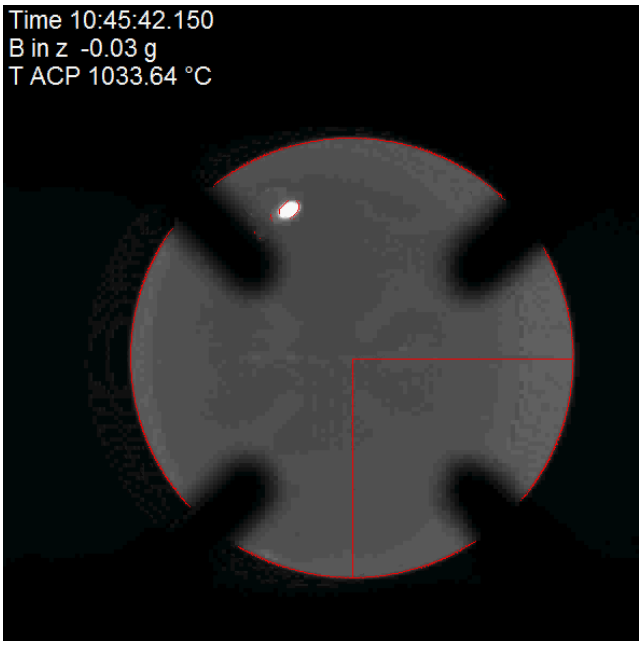

Figure 5.24: High speed camera image of a molten droplet of AMZ4 in the TEMPUS μg experiments. Using the TeVi software, the edge of the sample (red outline) and the x and z radii can be determined (red horizontal and vertical lines, respectively).

be first melted and stabilized before quenching under Helium. To facilitate the rapid melting of the sample, it was pre-heated to $T_{liq} - 200$K before the onset of the parabola. During the quench, two pulses from the heating coil perturb the oscillations necessary for the viscosity measurements. The first pulse was initiated after a pause of four seconds to allow the transient oscillations from the initial heating pulse to fully decay. Similarly, the second pulse was timed three seconds after the first. The increasing viscosity and proportionally decreasing decay time upon cooling allows the pulse timing to be shorter for the second pulse. Near the end of the parabola, the recalescence of the sample is clearly visible, signifying the onset of crystallization. This is interrupted by the rapid acceleration of the aircraft as the parabola ends, where the solidified droplet falls to the bottom of the sample holder and out of the direct line of sight of the camera. Due to the vertical positioning of the pyrometer, however, the temperature measurement continues (albeit no longer in containerless conditions). The sample must solidify before contacting the sample holder, otherwise it may stick to or damage the sample holder.

The recorded images must first be converted into radius data using the proprietary TeVi software. Figure 5.24 shows an example image that has been processed in TeVi, showing the red outline of the sample edge and horizontal and vertical lines corresponding to the respective radii. The software uses an edge-finding algorithm to define the sample projection based on contrast and

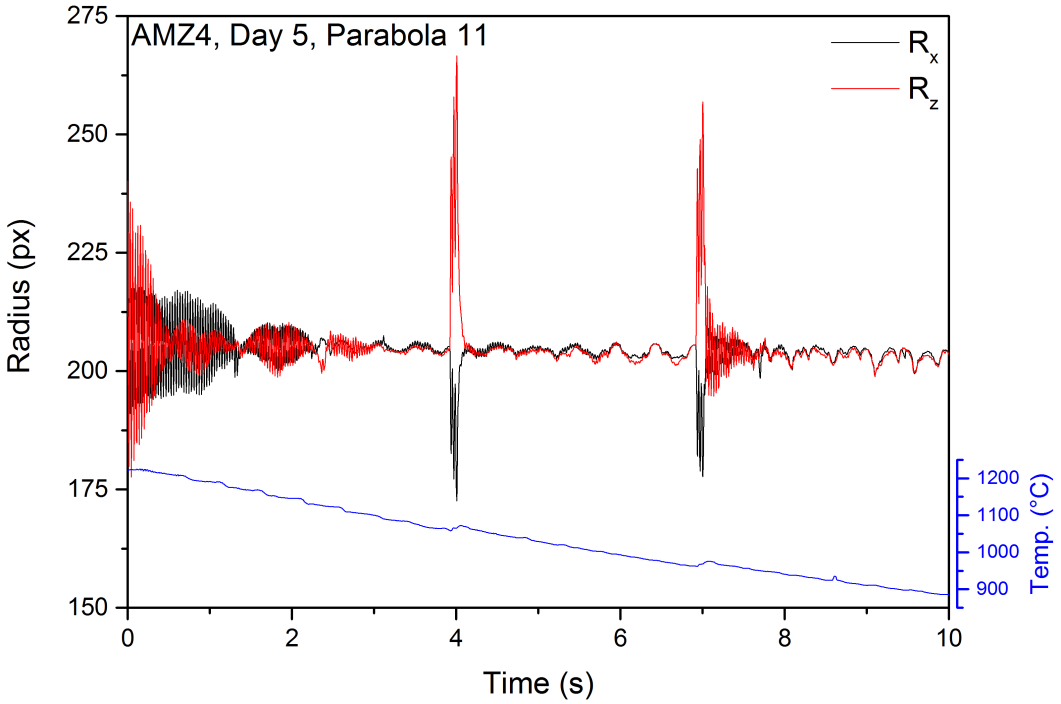

Figure 5.25: Horizontal (x) and vertical (z) radius oscillations for a single parabola of AMZ4. Recorded pyrometer temperatures are shown as a blue line.

the definition of so-called *Regions of Interest* (ROIs), which are used primarily to mask the sample holder window. This procedure is outlined in greater detail in the manual that is bundled with the software [1].

In this study, the contrast was set to 700 (arbitrary units) while the filter width and steepness parameters were left at their default values. This combination of parameters was found to best describe the actual the sample profile. The entire window was masked with two ROIs, one of which searched for edges from left-to-right, while the other scanned top-to-bottom. Using this method, it was found that the sample edge was accurately described and the out of focus edges of the sample holder were ignored. It is, however, important to note that this method is highly dependent on the quality of the images and the relative contrast between the sample and background. In the event that the image contrast is relatively poor, then the other parameters must also be tuned (i.e. filter width and steepness). Furthermore, each parabola video should be manually inspected to ensure that the sample remains within the bounds of the image window, at least during the pulses where viscosity must be calculated. If the sample drifts too far beyond the window, the program will calculate erroneous radius values.

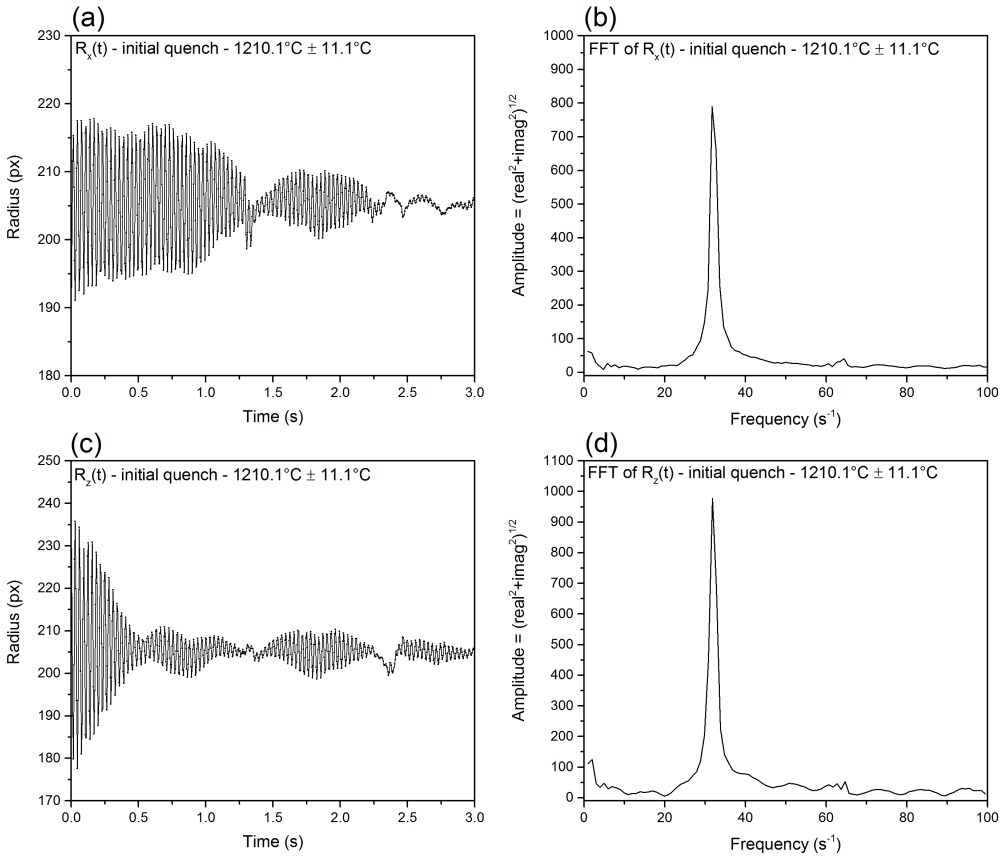

Figure 5.26: Oscillating droplet analysis of the initial quench for AMZ4 showing (a) the horizontal oscillations in R_x, (b) the FFT transformed R_x frequency spectra, (c) the vertical oscillations in R_z, (d) the FFT transformed R_z frequency spectra. Shifting and splitting of the resonant frequency are due to convective turbulence induced by the strong heating field required to melt the sample.

Subsequently, the resulting radii are then plotted as a function of time for analysis as shown in figure 5.25 for a single parabola from the measurement of high purity AMZ4 as an example. Starting at zero seconds, the sample is released after the initial heating pulse to approximately $1200°C$. After the four second delay, the first controlled pulse is given to the sample, and the second pulse follows shortly thereafter.

Significant turbulence is induced in the bulk of the sample due the relatively high field strength of the initial heating phase, which is observed from a manual inspection of the video. Therefore, care must be taken when interpreting this data. Direct fitting of these oscillations with an exponential curve produces spurious viscous damping coefficients. Additionally, this turbulence manifests as multi-modal oscillations, which can be identified through a fast-Fourier transform (FFT) of the radius data.

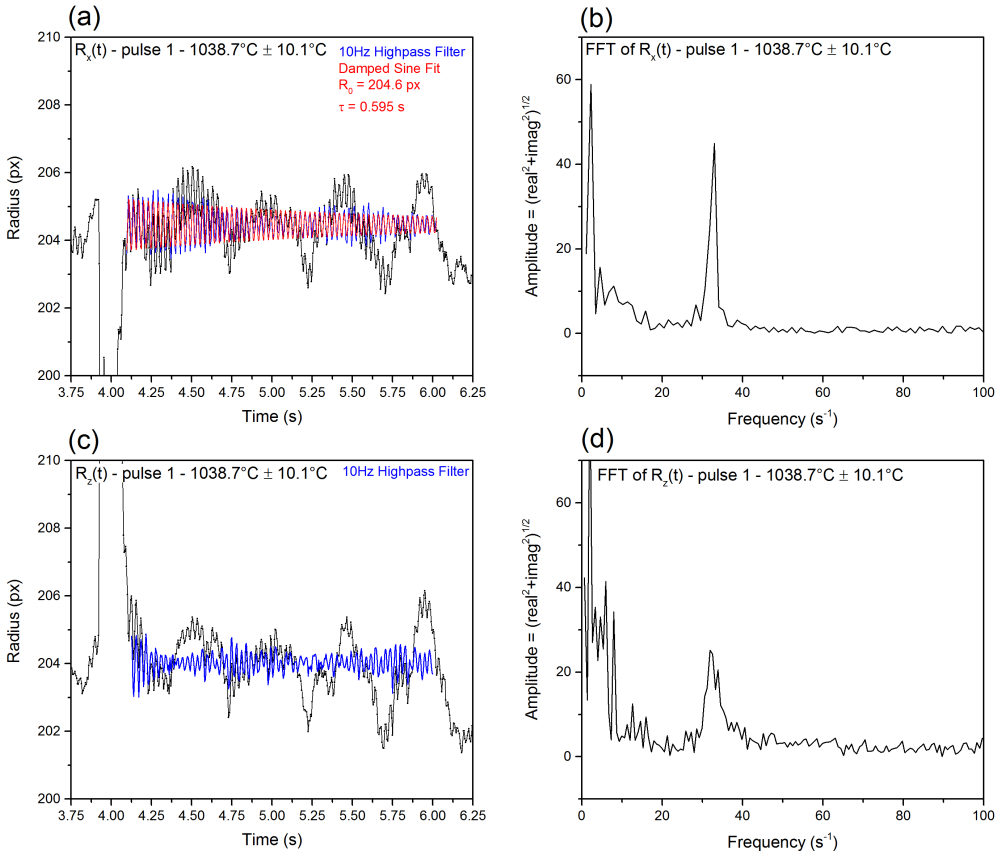

Figure 5.27: Oscillating droplet analysis of the first perturbation of AMZ4 showing (a) the horizontal oscillations in R_x, (b) the FFT transformed R_x frequency spectra, (c) the vertical oscillations in R_z, (d) the FFT transformed R_z frequency spectra. Blue curves show the data after applying a high pass filter with a cutoff frequency $\omega \geq 10$ s^{-1}, and the red curve shows the corresponding fit with a damped sine function.

Figure 5.26 shows the frequency spectra of the R_x and R_z data acquired during the first three seconds of damping after the melting pulse was released. In the absence of turbulent effects, the resonant frequency peak is defined by the $l = 2$, $m = 0$ mode considering the perspective of the camera in the TEMPUS device. This peak occurs at about 32 s^{-1} in the both AMZ4 variants. Depending on the modes that are present, turbulence will split and shift this peak. For example, an additional rotation of the sample about the y-axis (concurrent with the camera axis) manifested as the $l = 2$, $m = 1$ mode, evidenced by the high frequency peak at about 63 s^{-1}. Additionally, shoulders at 25 s^{-1} and 40 s^{-1} are apparent in the FFT of R_z(t). The low frequency (≤ 10 s^{-1}) peaks arose due to the slow translational oscillations of the droplet within the window. Similar behavior was observed in all of the TEMPUS experiments, including those performed on AMZ4 Zr705.

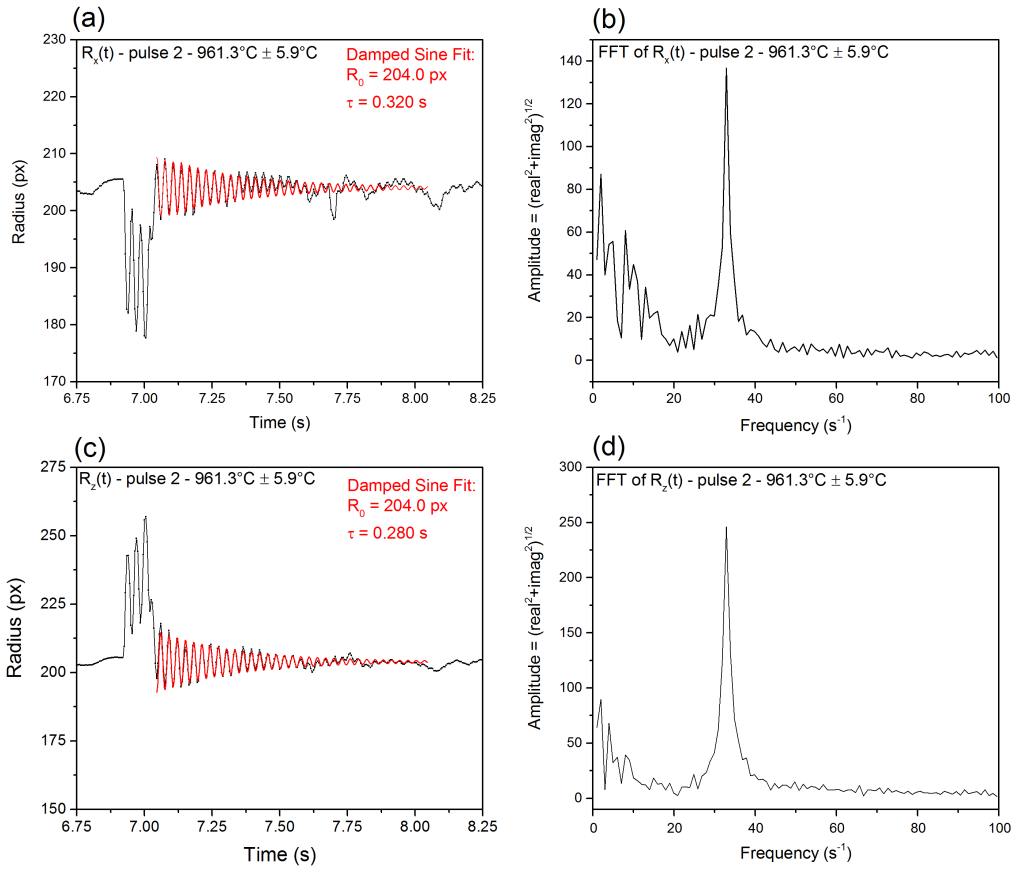

Figure 5.28: Oscillating droplet analysis of the second perturbation of AMZ4 showing (a) the horizontal oscillations in R_x, (b) the FFT transformed R_x frequency spectra, (c) the vertical oscillations in R_z, (d) the FFT transformed R_z frequency spectra. The red curves shows fitting with a damped sine function.

Figure 5.27 shows the horizontal and vertical radii and the corresponding frequency spectra for the first pulse of the same measurement shown before. This pulse was accompanied by the rotation of the sample such that extensional axis of the droplet was coincident with the camera axis, effectively concealing the amplitude of the oscillations behind the sample. Furthermore, the translational oscillations of the sample across the visible window are present. In the frequency spectra, these oscillations manifest as a pronounced low frequency group of peaks. Despite this, direct fitting of the radii with a damped sine curve was enabled in some cases by applying a high pass filter with a cutoff frequency of $\omega \geq 10$ s^{-1}. This cuts out the information from the translational and rotational oscillations. However, this was not always possible, as shown in figures 5.27c and 5.27d as an example. In these cases, the resonant peaks are clearly split and shifted due to turbulence. Fitting of that data was therefore rendered impossible, even with the high pass filter, as shown in figure 5.27c, which includes the filtered section of data.

The results from the second pulse showed significantly less turbulence, as shown in figure 5.28. As the temperature was reduced, the increasingly dominant viscous damping suppresses turbulence within the droplet. Although some transient oscillations were still present in the low frequency range, their amplitude was much smaller than the perturbed oscillations and fitting with the sine curve was possible without additional filters. The damped sine curve used to fit the data was of the form

$$r = r_0 \left[1 + \delta cos\left(\omega t\right) e^{-t/\tau}\right] \tag{5.8}$$

where r_0 is the quiescent radius, ω is the frequency, and τ is the damping time. The damping constant Γ can be used interchangeably with τ, where $\tau = \Gamma^{-1}$. Accordingly, the viscosity is determined according to Lamb's formula

$$\Gamma = \frac{20\pi}{3}\frac{\eta r_0}{m} \tag{5.9}$$

where m is the mass of the droplet and r_0 is the quiescent radius. The measured radius from the camera, however, is given in pixel rather than meters. A conversion can only be accomplished if the camera is calibrated with spheres of known size. Lacking this information, the measured radius of the solid sample serves as a good approximation. Similarly, the damping time can be calculated directly from the full width at half maximum (FWHM) of the resonant frequency peak according to [64],

$$\tau = \frac{\sqrt{3}}{\pi \Delta\omega} \tag{5.10}$$

where $\Delta\omega$ is the manually determined FWHM. The results from both types of calculations of the damping time are shown for AMZ4 in figure 5.29. Nearly identical values of the viscosity are obtained for both methods. Because of the turbulence induced peak splitting in the frequency spectra, fewer data points could be analyzed with the FWHM method. The temperature error is the standard deviation from the average recorded pyrometer temperature over the time that is fitted with the damped sine curve. For continuity, the same boundaries are used to define the FFT frequency spectra. The grouping of data about two high and low temperature regimes is a consequence of the automatic timing used by the TEMPUS device to determine the pulses.

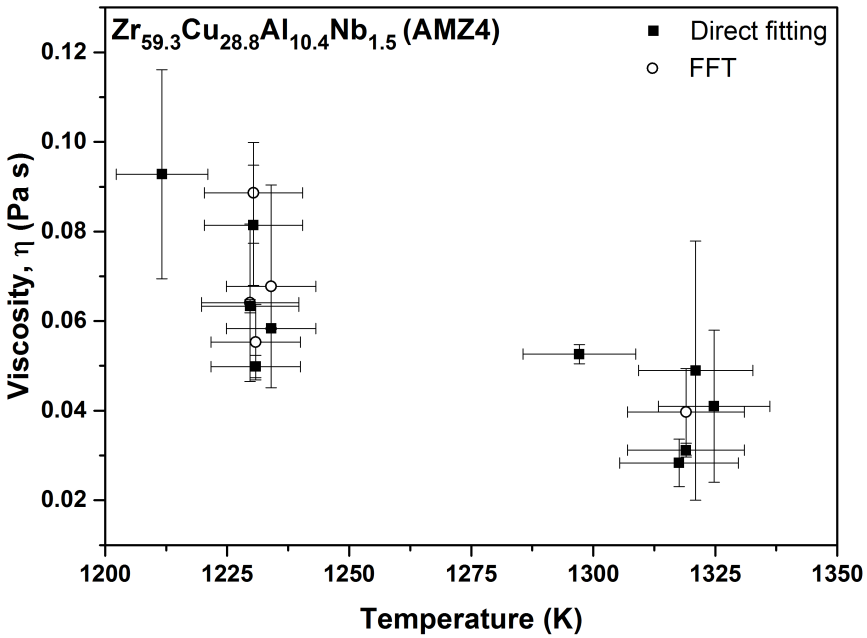

Figure 5.29: Calculated viscosities from the TEMPUS EML measurements of AMZ4 using both direct fitting with a damped sine curve (solid squares) and with the FWHM of the resonant peak (open circles).

The surface tension was calculated from the resonant frequency according to the relation [33]

$$\gamma = \frac{3\pi}{8} m\omega_R^2 \tag{5.11}$$

where ω_R is the resonant frequency peak obtained from the FFT analysis. Results for both variants of AMZ4 are shown in figure 5.30. AMZ4 manufactured with high purity Zr-crystal bar has a surface tension of about 1.6 Nm^{-1}, while the low purity variant of AMZ4 has a surface tension of about 1.4 Nm^{-1}. These values are consistent with the observations made in other liquid metal systems measured with the same technique, where typical values for the surface tension range between $1.0 \leq \gamma \leq 2.0$ Nm^{-1} [34, 72, 77, 134]. Furthermore, the difference in surface tension is also consistent with the observation that the surface tension is reduced for minor increases in soluble oxygen content, where even a few ppm can reduce the surface tension by about 10% [77]. The pre-alloy material Zircadyne R60705 contains up to 1 at% oxygen [121]. Using wet chemical analysis, Heinrich and coworkers [67] found that the high purity composition of AMZ4 has an oxygen concentration of 590 ppm while the industrial sample retains up to 4120 ppm. The oscillating droplet results shown here indicate that the oxygen content reduces the surface tension.

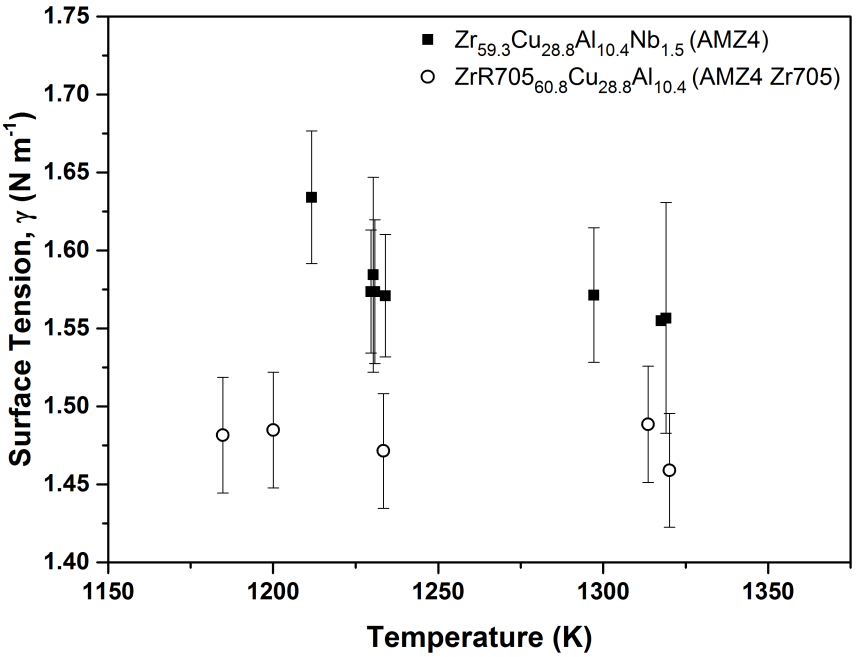

Figure 5.30: Surface tension of both the high purity (closed squares) and industrial (open circles) variants of AMZ4 measured by the oscillating drop technique

However, the difference in surface tension found here is small compared to the errors arising from instrumentation and fitting (approximately 5%). Because these measurement were conducted in separate flight campaigns, environmental differences (e.g. from the Helium atmosphere) in the TEMPUS-EML may also contribute to to the discrepancy in surface tension observed here. It is worth noting that the same quality of surface tension measurements is not possible in ESL due to disturbances rising from the electrostatic forces acting on the surface of the droplet. Such measurements typically show values of surface tension that are higher than those obtained through other methods [139].

Figures 5.31 and 5.32 compare the measured viscosities for Couette, ESL, and TEMPUS-EML experiments on both AMZ4 variants. The oscillating droplet method in both EML and ESL provide consistent results for both compositions, while a discrepancy is observed in the Couette measurements for AMZ4 with Zr705. The Couette viscosities for the industrial grade composition are more than a factor of two greater than those obtained with the oscillating droplet technique.

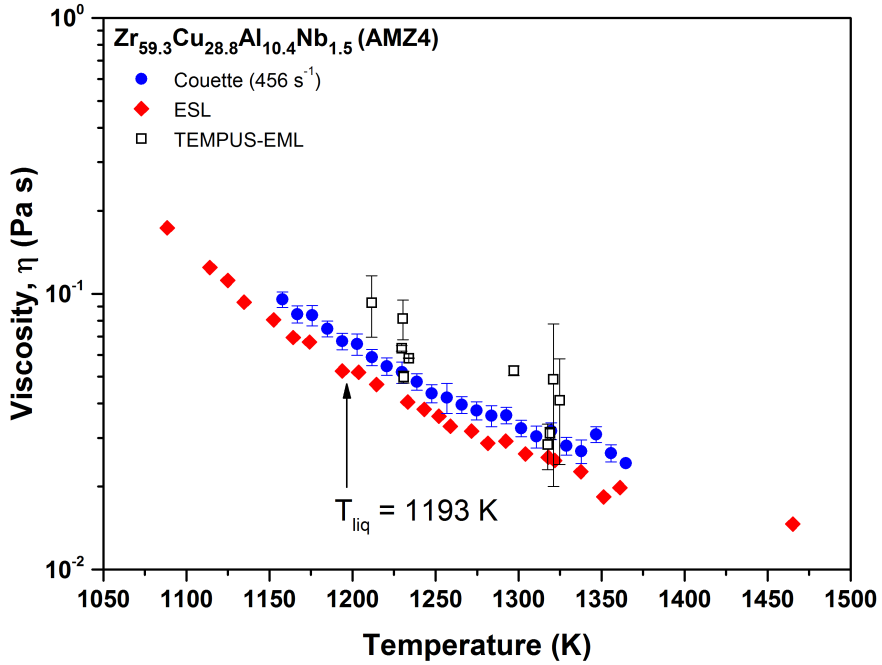

Figure 5.31: Viscosities measured for high purity AMZ4 with Couette, ESL, and EML direct-fitting methods.

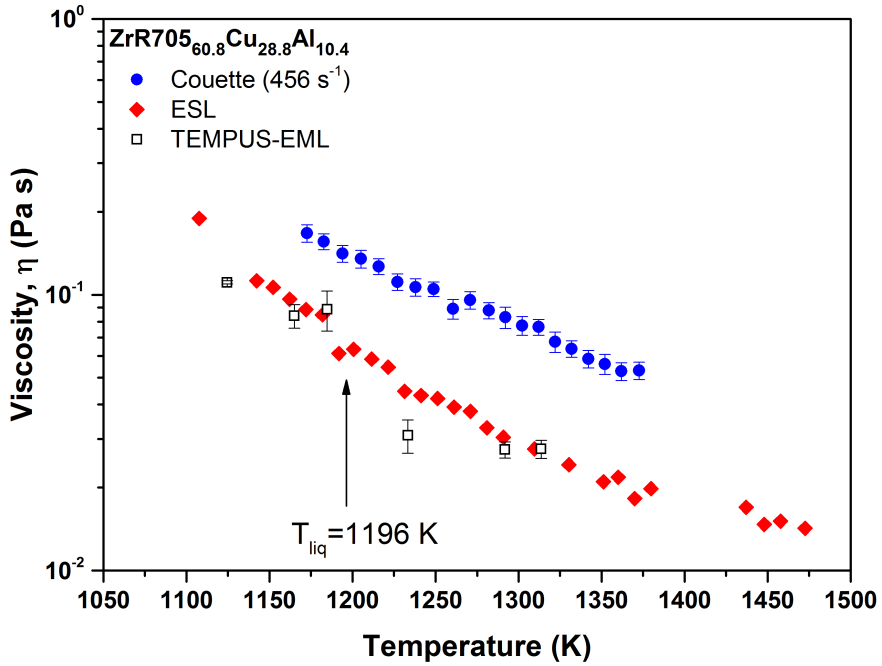

Figure 5.32: Viscosities measured for industrial AMZ4 with Couette, ESL, and EML direct-fitting methods.

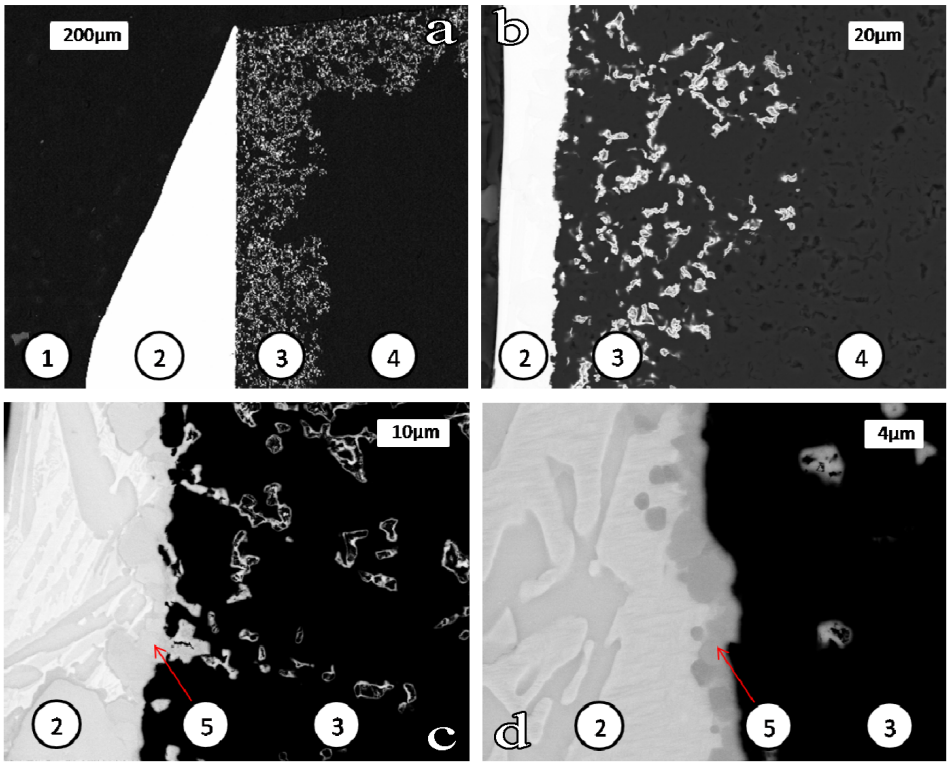

Figure 5.33: SEM backscattered electron images for the cross section of the Couette shear cell after an experiment. (a) Bob cross section for $Zr_{65.0}Cu_{17.5}Ni_{10.0}Al_{7.5}$, where (1) indicates the embedding material, (2) the bulk of the melt, (3) the infiltration of the melt into the pores, and (4) the graphite of the bob. (b) The infiltration layer for a measurement of $Zr_{60.0}Cu_{25.0}Al_{15.0}$. (c) A closer view, showing the ZrC layer (5) that formed for a measurement of $Zr_{60.0}Cu_{25.0}Al_{15.0}$. (d) A similar view showing the ZrC layer in a shear cell used for $Zr_{60.0}Cu_{25.0}Al_{15.0}$. Images courtesy of Stefan Gärtner [110].

The inconsistency in AMZ4 Zr705 is likely due to contamination of the melt and the formation of a slag very early in the measurement. The occurrence of such contamination seems to be the exception rather than the rule for these Zr based alloys, as shown by SEM investigations of the cross section of the shear cell after measurements. Stefan Gärtner made a large contribution to that work, focusing primarily on studies of $Zr_{65.0}Cu_{17.5}Ni_{10.0}Al_{7.5}$ and $Zr_{60.0}Cu_{25.0}Al_{15.0}$ [110], shown in figure 5.33. A stable zirconium carbide layer forms at the interface between the melt and graphite shear cell. This layer remains stable at thicknesses below 10µm over the course of an eight hour long experiment, which is in good agreement with the measurements of Way and coworkers for Vit1 [47].

Despite the stability of this layer, one possible contamination mechanism is through mechanical instability induced abrasion between the bob and cup. Evidence for this mechanism is supported by observation of pieces of ZrC

were found to be entrained within the melt after the experiment. Most of the ZrC within the melt was found in layers suggesting that it originally was floating at the surface of the melt during the experiment. At the end of an experiment, the bob must be extracted from the melt to prevent the risk of damaging the sensor and for ease of disassembly[1]. Due to the *ex-situ* nature of the SEM investigations, however, it is impossible to tell when this occurs during a measurement. There is no indication of a sudden rise in viscosity due to such abrasive contamination processes. Furthermore, the temperature and shear rate dependent behavior remain similar to the high purity AMZ4 over the duration of the experiment. The combination of these factors suggests that another mechanism is responsible for the discrepancy in viscosity observed for AMZ4 Zr705. One likely explanation is that a surface layer formed at the beginning of the experiment due to contaminants in the atmosphere of the chamber.

5.3 Phenomenology beyond VFT

In addition to analysis with the purely empirical Vogel-Fulcher-Tammann equation, the viscosity data was also analyzed with the Adam-Gibbs [2] configurational entropy and Cohen-Grest [25,117,170] free volume models. Unlike the VFT equation, these models describe the kinetic behavior of the system according to measurable physical quantities as described in section 2.3. The predictive ability of these models has been previously demonstrated for metallic glass forming systems such as $Zr_{44.0}Ti_{11.0}Cu_{10.0}Ni_{10.0}Be_{25.0}$ (Vitreloy 1b) [103]. Here, both models are applied to the low and high temperature viscosity data.

Starting with the Adam-Gibbs model, the primary physical quantity of interest is the configurational entropy $S_c(T)$, which describes the atomic packing configurations available at a given temperature. Accordingly, the viscosity is calculated with the expression

$$\eta = \eta_0 \exp\left(\frac{C}{TS_c}\right) \tag{5.12}$$

where C is the activation energy for cooperative rearrangements. While $S_c(T)$ cannot be directly measured, it can be estimated as the excess entropy of the liquid compared to the crystalline state at the same temperature, $\Delta S_c^{l-x} = S_{liquid} - S_{crystal}$. However, this method assumes a connection between the

[1]The only alternative is to completely disassemble the upper section of the viscometer while holding the upper shaft stationary. This poses an immense risk to the sensor and is therefore not suggested.

fragility of the liquid and the crystalline state, which may never be encountered in some glass formers. Thus, Gallino and coworkers [65] developed a method of determining the configurational entropy that is independent from the crystalline state. An additional term $S_c(T_m^*)$ is introduced that represents the configurational entropy of the liquid at a given temperature. Gallino arbitrarily defined T_m^* as the temperature at which the viscosity is equal to 1 Pa s. $S_c(T)$ can then be approximated by

$$S_c(T) = S_c(T_m^*) - \int_T^{T_m^*} \frac{\Delta c_p^{l-x}(T')}{T'} dT' \tag{5.13}$$

Equation 5.13 is then substituted into equation 5.12 and C and $S_c(T_m^*)$ are left as fitting parameters to the viscosity data. At temperatures above the Debye temperature, the integral term in equation 5.13 is determined from fitting calorimetric specific heat capacity of the liquid $c_p^l(T)$ and crystalline $c_p^x(T)$ states according to the following equations defined by Kubaschewski [84]

$$c_p^l(T) = 3R + aT + bT^{-2} \tag{5.14}$$

$$c_p^x(T) = 3R + cT + dT^2 \tag{5.15}$$

$$\Delta c_p^{l-x}(T) = c_p^l(T) - c_p^x(T) \tag{5.16}$$

where a, b, c, and d are fitting constants. For most of the alloys in this study, the heat capacity data and associated constants were found in previous publications. In this study, $Zr_{65.0}Cu_{17.5}Ni_{10.0}Al_{7.5}$ and $Zr_{60.0}Cu_{25.0}Al_{15.0}$ were both investigated with the calorimetric methods outlined in chapter 4. The step method in the DSC was used to obtain accurate heat capacity data near the glass transition temperature, while continuous scans in the DTA were used at high temperatures near the melting point. The heat capacity at high temperatures was estimated with the help from the difference in the enthalpies of fusion and crystallization, which is related to the integration of the heat capacity curves of the liquid and crystalline states in the defined temperature range, given by

$$\Delta H_f - \Delta H_x = \int_{T_x}^{T_{liq}} \Delta c_p^{l-x}(T') dT' \tag{5.17}$$

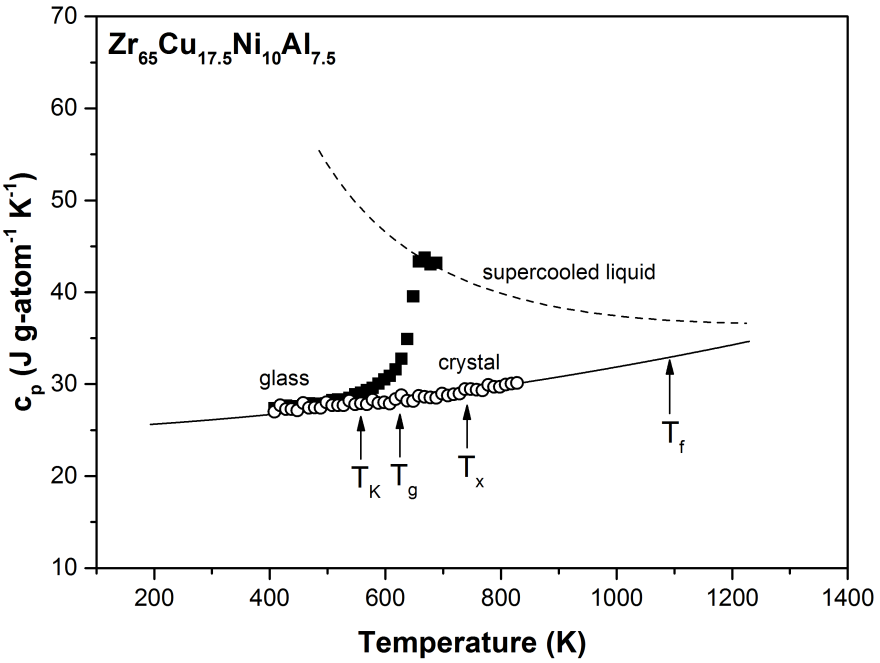

Figure 5.34: Specific heat capacity data for $Zr_{60.0}Cu_{25.0}Al_{15.0}$, where the initially glassy data are closed squares and initially crystalline samples are open circles. Fits of the crystalline data to equation 5.15 are solid lines while the fits of the supercooled liquid to equation 5.14 are dashed lines. $T_f = 1094$ K is the temperature of the peak of the heat of fusion.

where T_x is the crystallization temperature and T_{liq} is the liquidus temperature. The specific heat capacity data and corresponding fits to equations 5.14 and 5.15 are shown for $Zr_{65.0}Cu_{17.5}Ni_{10.0}Al_{7.5}$ in figure 5.34.

For $Zr_{65.0}Cu_{17.5}Ni_{10.0}Al_{7.5}$ the enthalpy of fusion is $\Delta H_f = 8.4$ kJ g-atom^{-1} and the Kubaschewski fitting parameters are $a = 6.02 \times 10^{-3}$ J g-atom^{-1} K^{-2}, $b = 6.48 \times 10^{6}$ J K g-atom^{-1}, $c = 2.68 \times 10^{-3}$ J g-atom^{-1} K^{-2}, and $d = 4.24 \times 10^{-6}$ J g-atom^{-1} K^{-3}. Meanwhile, for $Zr_{60.0}Cu_{25.0}Al_{15.0}$ the enthalpy of fusion is $\Delta H_f = 8.5$ kJ g-atom^{-1} and the Kubaschewski fitting parameters are $a = 7.33 \times 10^{-3}$ J g-atom^{-1} K^{-2}, $b = 7.82 \times 10^{6}$ J K g-atom^{-1}, $c = 4.66 \times 10^{-3}$ J g-atom^{-1} K^{-2}, and $d = 9.60 \times 10^{-7}$ J g-atom^{-1} K^{-3}. It should be noted that the quality of data for $Zr_{60.0}Cu_{25.0}Al_{15.0}$ was very poor in the supercooled liquid and the fits are dubious at best. For all of the alloys in this study, the Kubaschewski fitting parameters are shown in table 5.3 and the enthalpies of fusion and crystallization along with the relevant temperatures are summarized in table 5.4.

Table 5.3: Kubaschewski fitting parameters

Composition (at%) [ref]	a (J g-atom^{-1} K^{-2})	b (J K g-atom^{-1})	c (J g-atom^{-1} K^{-2})	d (J g-atom^{-1} K^{-3})
$Zr_{59.3}Cu_{28.8}Al_{10.4}Nb_{1.5}$ (AMZ4) [121]	5.23×10^{-4}	1.03×10^{7}	6.23×10^{-3}	-6.05×10^{-7}
$Zr705_{60.8}Cu_{28.8}Al_{10.4}$ (AMZ4 705) [121]	5.23×10^{-4}	1.03×10^{7}	6.23×10^{-3}	-6.05×10^{-7}
$Zr_{60.0}Cu_{25.0}Al_{15.0}$	7.33×10^{-3}	7.82×10^{6}	4.66×10^{-3}	9.60×10^{-7}
$Zr_{65.0}Cu_{17.5}Ni_{10.0}Al_{7.5}$	6.02×10^{-3}	6.48×10^{6}	2.68×10^{-3}	4.24×10^{-6}
$Zr_{58.5}Cu_{15.6}Ni_{12.8}Al_{10.3}Nb_{2.8}$ (Vit106a) [93, 103]	5.65×10^{-3}	5.70×10^{6}	-7.10×10^{-3}	1.37×10^{-5}
$Zr_{57.0}Cu_{15.4}Ni_{12.6}Al_{10.0}Nb_{5.0}$ (Vit106) [93, 103]	1.33×10^{-2}	6.32×10^{6}	-3.02×10^{-3}	8.37×10^{-6}
$Zr_{52.5}Cu_{17.9}Ni_{14.6}Al_{10.0}Ti_{5.0}$ (Vit105) [93, 103]	2.12×10^{-2}	6.43×10^{6}	-8.61×10^{-3}	1.68×10^{-5}
$Cu_{47.0}Ti_{34.0}Zr_{11.0}Ni_{8.0}$ (Vit101) [93, 103]	1.56×10^{-2}	2.83×10^{6}	-8.90×10^{-3}	6.82×10^{-6}

Table 5.4: Calorimetric data

Composition (at%) [ref]	T_{liq} (K)	ΔH_f (kJ g-atom^{-1})	T_x (K)	ΔH_x (kJ g-atom^{-1})	q_H
AMZ4 [121]	1193	8.6	742	-4.7	0.50
AMZ4 705 [121]	1196	8.6	742	-4.7	0.50
$Zr_{60.0}Cu_{25.0}Al_{15.0}$	1260	8.5	759	-4.1	0.33
$Zr_{65.0}Cu_{17.5}Ni_{10.0}Al_{7.5}$	1164	8.4	743	-7.2	0.33
Vit106a [93, 103]	1140	8.7	752	-6.4	0.33
Vit106 [93, 103]	1115	9.4	736	-5.5	0.33
Vit105 [93, 103]	1125	8.2	727	-6.8	0.33
Vit101 [93, 103]	1164	11.3	717	-7.5	0.33

The enthalpy and entropy difference between the crystal and liquid states can be calculated according to the following expressions

$$\Delta H^{l-x}(T) = \Delta H_f + \int_{T_f}^{T} \Delta c_p^{l-x}(T')dT' \tag{5.18}$$

$$\Delta S^{l-x}(T) = \Delta S_f + \int_{T_f}^{T} \frac{\Delta c_p^{l-x}(T')}{T'}dT' \tag{5.19}$$

Where T_f is the temperature of peak of the heat of fusion, where the Gibbs free energy of the liquid coincides with that of the crystal. Accordingly, the Gibbs free energy difference relative to the crystalline state can be calculated with

$$\Delta G^{l-x}(T) = \Delta H^{l-x} - T\Delta S^{l-x} \tag{5.20}$$

Plots of ΔH^{l-x} and ΔS^{l-x} for $Zr_{65.0}Cu_{17.5}Ni_{10.0}Al_{7.5}$ are shown in figures 5.35 and 5.36. In both plots, the glassy state is shown schematically as a dashed line. At the Kauzmann temperature T_K, the entropy of the liquid is equal to that of the crystalline state and subsequent extrapolation below this point would violate the third law of thermodynamics, resulting in the *Kauzmann paradox* [129]. The Kauzmann temperature is found to be $T_K = 556$ K for $Zr_{65.0}Cu_{17.5}Ni_{10.0}Al_{7.5}$, which is below its glass transition temperature. This is also consistent with the findings of other metallic glass formers. Figure 5.37 shows the calculated $\Delta G^{l-x}(T)$ curve for $Zr_{65.0}Cu_{17.5}Ni_{10.0}Al_{7.5}$.

From this information, the integral expression in equation 5.13 can be solved analytically and then used in conjunction with equation 5.12 to model the viscous behavior of these liquids. The temperature T_m^* is estimated from VFT-fits of the low temperature data from section 5.1. Meanwhile, C and $S_c(T_m^*)$ are left as fitting parameters.

This analysis was performed for all eight alloys in this study and the fitting results are summarized in table 5.5. Fitting was only performed on data obtained from isothermal three point beam bending experiments near the glass transition temperature. In all cases, the fitting is, for all intents and purposes, identical to the VFT-fits in the same range. At higher temperatures, the similarity breaks down along with the assumptions behind the model itself. As an example, figure 5.38 shows the results from the Adam-Gibbs fitting for $Zr_{65.0}Cu_{17.5}Ni_{10.0}Al_{7.5}$ along with fits of with the empirical VFT equation.

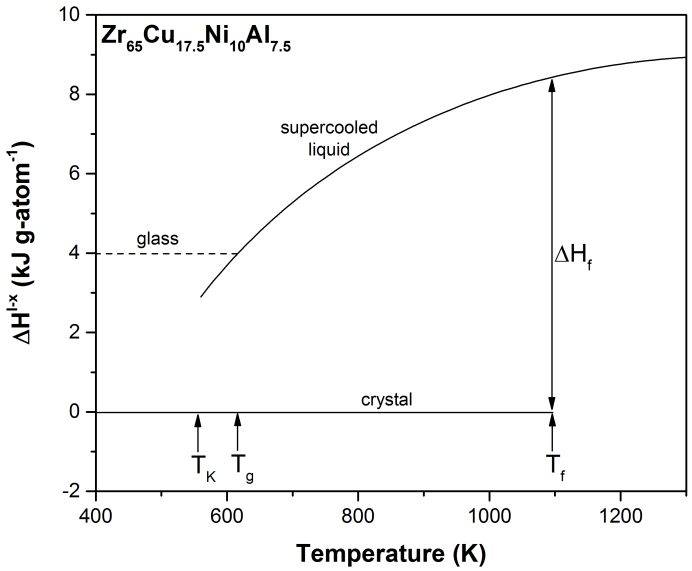

Figure 5.35: Enthalpy difference of liquid $Zr_{65.0}Cu_{17.5}Ni_{10.0}Al_{7.5}$ with respect to the crystal. The curved line is the calculated enthalpy difference according to equation 5.18 and the horizontal line at 0 kJ g-atom^{-1} represents the crystalline state.

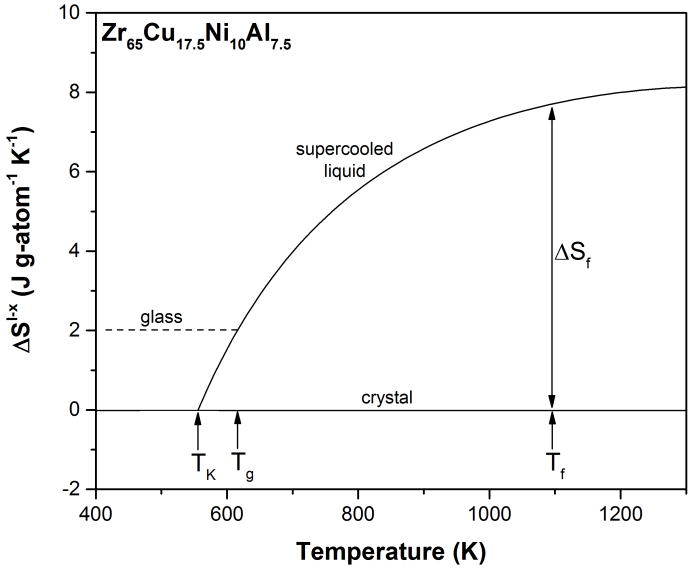

Figure 5.36: Entropy difference of liquid $Zr_{65.0}Cu_{17.5}Ni_{10.0}Al_{7.5}$ with respect to the crystal. The curved line is the calculated entropy difference according to equation 5.19 and the horizontal line at 0 kJ g-atom^{-1} K^{-1} represents the crystalline state. Additionally, the Kauzmann temperature is found when the entropy of the liquid is equal to that of the crystal, and is found to be $T_K = 556$ K.

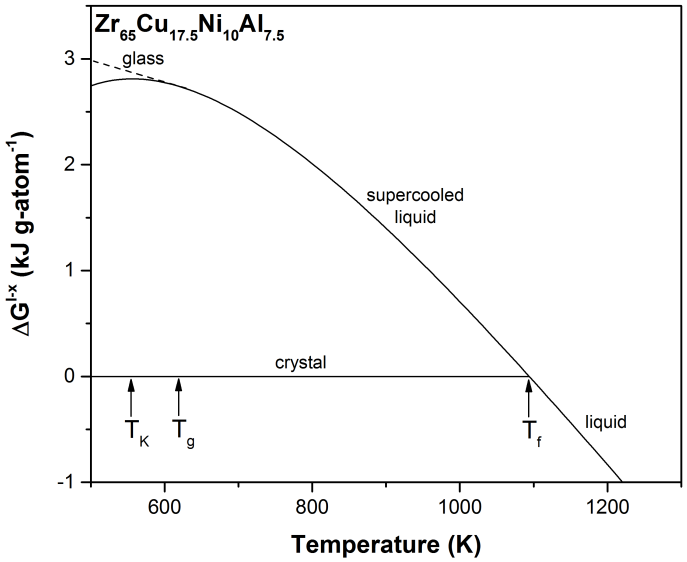

Figure 5.37: Gibbs free energy difference of liquid $Zr_{65.0}Cu_{17.5}Ni_{10.0}Al_{7.5}$ with respect to the crystal. The curved line is the calculated entropy difference according to equation 5.20 and the horizontal line at 0 kJ g-atom^{-1} K^{-1} represents the crystalline state.

Table 5.5: Adam Gibbs fitting results

Composition (at%)	$S_c(T_m^*)$ (J g-atom^{-1} K^{-1})	C (kJ g-atom^{-1})
$Zr_{59.3}Cu_{28.8}Al_{10.4}Nb_{1.5}$ (AMZ4)	19.63	345
$Zr705_{60.8}Cu_{28.8}Al_{10.4}$ (AMZ4 705)	17.76	310
$Zr_{60.0}Cu_{25.0}Al_{15.0}$	20.26	310
$Zr_{65.0}Cu_{17.5}Ni_{10.0}Al_{7.5}$	17.86	277
$Zr_{58.5}Cu_{15.6}Ni_{12.8}Al_{10.3}Nb_{2.8}$ (Vit106a)	13.56	243
$Zr_{57.0}Cu_{15.4}Ni_{12.6}Al_{10.0}Nb_{5.0}$ (Vit106)	32.36	522
$Zr_{52.5}Cu_{17.9}Ni_{14.6}Al_{10.0}Ti_{5.0}$ (Vit105)	28.18	364
$Cu_{47.0}Ti_{34.0}Zr_{11.0}Ni_{8.0}$ (Vit101)	13.76	155

Contrary to the reports for Vitreloy 1 [103], the Adam-Gibbs fit provides a poor prediction of the high temperature data. This may be caused by an intervening transition between two liquid phases with distinct kinetic fragilities. For Vitreloy 1, the Adam-Gibbs fitting is compared to the strong liquid, which was still present during the rheometric measurements performed by Way and coworkers [47]. However, in all of the alloys in the present study, the high temperature liquid was always fragile and was found to be several orders of magnitude less viscous than the extrapolation of both the Adam-Gibbs and low-temperature VFT fits.

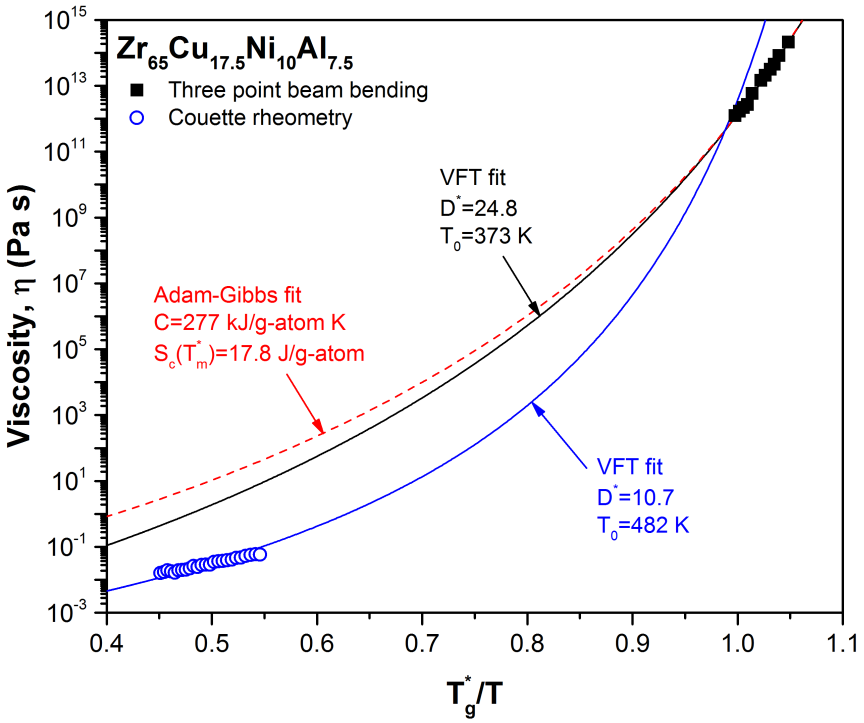

Figure 5.38: Plot of the viscosity normalized to the glass transition temperature for $Zr_{65.0}Cu_{17.5}Ni_{10.0}Al_{7.5}$. The solid squares represent equilibrium viscosity data obtained from isothermal three point beam bending relaxation experiments and the open circles are from high temperature Couette rheometry measurements. Fits of the low and high temperature data to the empirical VFT equation are shown as solid black and blue lines, respectively. A fit of the low temperature data to the Adam-Gibbs equation is shown as a dashed red line.

The value of $S_c(T_m^*)$ is larger than both the ideal entropy of mixing and the measured entropy of fusion for these systems. The ideal entropy of mixing is $\Delta S_{mix}^{id} = -R\Sigma\,(X_i ln X_i)$, where X_i is the gram-atomic fraction of the constituent elements. For $Zr_{60.0}Cu_{25.0}Al_{15.0}$, the ideal entropy of mixing is $\Delta S_{mix}^{id} = 7.80$ J g-atom^{-1} K^{-1} and the measured entropy of fusion is $\Delta S_f = 6.67$ J g-atom^{-1} K^{-1}. By contrast, the Adam-Gibbs configurational entropy is $S_c(T_m^*) = 20.26$ J g-atom^{-1} K^{-1}.

The apparent activation energy ranges between $155 \leq C \leq 522$ kJ g-atom^{-1} (1.61 to 5.41 eV). Faupel and coworkers [56] compiled a large quantity diffusion measurements for metallic glasses and observed that the activation enthalpy for self diffusion increases with increasing solute diameter. This size dependency is a consequence of elastic interactions between the diffusing solute and neighboring solvent atoms. Accordingly, the expected activation energy for Zr-solute atoms is approximately 3.0 ± 1.5 eV [56], which is in excellent agreement with the estimated apparent activation energy from Adam-Gibbs in the present work as well as previous studies on similar systems [65, 103].

5.4 Strong-Fragile transition

In all of the Zr-based BMGs in this study, clear differences between the high and low temperature fragilities were observed using a variety of independent measurement techniques. Near the glass transition, all of the alloys exhibit strong behavior, with fragility parameters of about $D^* = 25$. Meanwhile, all of the alloys show distinctly more fragile behavior at high temperatures in the melt, with fragility parameters of about $D^* = 10$. This can be summarized in an Angell plot of the data as shown for AMZ4 as an example in figure 5.39. These findings are congruent with other investigations of Zr-based alloys [47, 100, 103, 178]. However, contrary to the measurements for Vit1 by Way and coworkers [47], neither a direct transition nor shear thinning behavior were observed in any of the systems. A transition is expected to occur at intermediate temperatures. Unfortunately, this regime is inaccessible using the viscosity measurements presented here. Nevertheless, from this study, it can be inferred that these alloys fall into the intermediate case of Angell's "big picture" classification of S-F transitions.

Similar investigations of the high and low temperature viscosities were conducted by Zhang and coworkers for Gd-, Pr-, Sm- La-, Al-, and Ce- based alloys [49, 50]. Not only do their findings show similar trends in the fragility, but the authors also developed a simple metric for comparing the magnitude of the S-F transition. This metric is the ratio of the fragility parameters m from fits of the high and low temperature data, where for an alloy exhibiting a S-F transition has a ratio

$$f = \frac{m'}{m} \geq 1 \tag{5.21}$$

where m' is the slope of the fit extrapolated from the high temperature data to T_g^* and m is the same parameter from the low temperature data, and f is known as the transition factor. Higher values of f correspond to a greater difference in the kinetics between the high and low temperature liquids. The systems studied by Zhang and coworkers exhibit transition factors of about $3 \leq f \leq 8$ [49, 50]. Calculating the S-F transition ratio f for the Zr-based alloys shows values of about $f \approx 2$, the results of which are summarized in table 5.6 for all of the compositions in this study. The agreement between these results and those from Zhang et al. suggest that the S-F transition is not a unique feature of any single composition, but rather a universal aspect of metallic glass formers.

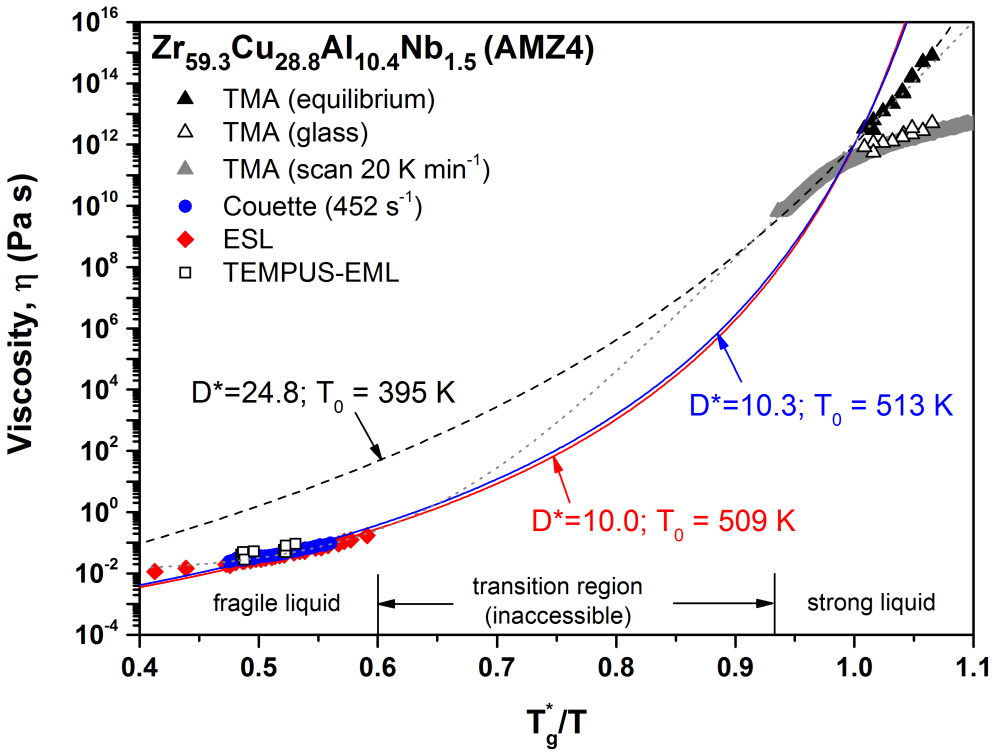

Figure 5.39: Angell plot for AMZ4 showing TMA three point beam bending (triangles), Couette (blue circles), ESL (red diamonds), and TEMPUS-EML (squares) viscosity results. VFT-fits of the high temperature data are shown as solid lines, while low temperature fits are the dashed line. The dotted line shows a hypothetical pathway between the strong and fragile liquids.

Table 5.6: Strong-Fragile transition ratio

Composition (at%)	m'	m	f
$Zr_{59.3}Cu_{28.8}Al_{10.4}Nb_{1.5}$ (AMZ4)	73.3	39.8	1.84
$Zr705_{60.8}Cu_{28.8}Al_{10.4}$ (AMZ4 705)	66.0	39.0	1.69
$Zr_{60.0}Cu_{25.0}Al_{15.0}$	72.2	40.4	1.79
$Zr_{65.0}Cu_{17.5}Ni_{10.0}Al_{7.5}$	71.1	39.7	1.79
$Zr_{58.5}Cu_{15.6}Ni_{12.8}Al_{10.3}Nb_{2.8}$ (Vit106a)	73.3	40.5	1.81
$Zr_{57.0}Cu_{15.4}Ni_{12.6}Al_{10.0}Nb_{5.0}$ (Vit106)	75.0	35.4	2.12
$Zr_{52.5}Cu_{17.9}Ni_{14.6}Al_{10.0}Ti_{5.0}$ (Vit105)	63.2	44.8	1.41
$Cu_{47.0}Ti_{34.0}Zr_{11.0}Ni_{8.0}$ (Vit101)	109.7	52.6	2.09

Chapter 6

Conclusions and Outlook

The primary focus of this work was to investigate the temperature dependent kinetic behavior of Zirconium based BMG-forming systems. To this end, the viscosity of eight different alloys were measured in both high and low temperature regimes using a variety of techniques. Before the high temperature measurements could even be started, however, a custom built rheometer was first developed and optimized for these particular experiments. Thus, this final chapter is divided into two sections. First, the engineering aspects of the Couette rheometer will be summarized. Second, the key experimental results and the corresponding conclusions drawn from them will be presented. These two sections will also include relevant discussions of future work and possibilities.

6.1 Development of the Couette rheometer

A large portion of this work was devoted to the development of a concentric cylinder rheometer that could accurately measure the viscosity of molten zirconium based alloys. To facilitate measurements at the LMW, a high temperature concentric cylinder rheometer was designed, built, and programmed using knowledge gleaned from the previous machine used by Way to characterize Vitreloy 1 [47, 48]. The device was redesigned to incorporate the new torque sensor and to minimize the mechanical instabilities arising from misalignment. With the exception of the upper bearing housing and stepper motor, the entire frame, vacuum chamber, and shear cell assembly were completely redesigned. Unlike the earlier iteration of the device, only minor realignments are now necessary prior to an experiment. The additional rigidity of the apparatus also mitigates instabilities which may arise during a measurement. Furthermore, the sensor housing is now protected from overheating with a water-cooled mounting plate.

Arguably the most critical change to the device is the new Mooney-Ewart conicylinder. This new design ensures a constant shear rate both at the bottom of the shear cell as well as within the annulus. Furthermore, the tapered end helps to reduce the entrapment of gas bubbles. These two effects have massively improved the reliability of the device during experiments.

In addition to the physical changes to the device, the LabVIEW data acquisition software was completely rewritten. Notable changes include the improved temperature controller, streamlined data handling, and reorganization of both the user interface and block-diagrams. Presently, the user can easily define heating and shear rate profiles that run automatically over the course of the entire experiment. Data analysis was simplified drastically by removing unnecessary intermediate file conversions.

Significant modifications to the shear cell must be considered for non-Zr based alloys. The shear cell material be selected to minimize the chance of reaction with the melt. Additionally, the mechanical instabilities present in the current device should be addressed before proceeding with more measurements. These instabilities arise from the thermal expansion of the steel shafts upon which the shear cell is mounted. To resolve this issue, new shafts with similar dimensions should be machined out of Molybdenum or a similar material that has a similar thermal expansion coefficient as the shear cell material. Because the shear cell material may change depending on the alloy family, an alternative design is suggested that utilizes an expanding intermediate ring as described in [154].

By comparing the measurements in the Couette rheometer to containerless techniques, it is possible to assess the reliability of the device. Under optimal operating conditions, it is found that the uncertainty relative to the ESL measurements is approximately 25% at the liquidus temperature. Suboptimal operating conditions were readily identifiable in $Zr705_{60.8}Cu_{28.8}Al_{10.4}$ (AMZ4 705), where the formation of a slag caused a significant deviation from the expected viscosities from containerless measurements. Likewise, the entrapment of Argon bubbles under the bob resulted in aberrations in $Zr_{52.5}$-$Cu_{17.9}Ni_{14.6}Al_{10.0}Ti_{5.0}$ (Vit105). Despite these two outliers, the rheometer has clearly demonstrated its ability to accurately measure viscosities within the range necessary to characterize the highly viscous metallic glass forming alloys. Furthermore, the current iteration can measure over a much wider range of temperatures than previous versions of the device. This opens up the possibility to measure systems with even deeper melting temperatures.

6.2 The kinetics of Zr-based BMGs

At temperatures near the glass transition, the standard three point beam bending method was used to investigate the relaxation behavior under isothermal and continuous heating conditions. In order to rule out systematic errors from any single technique at high temperatures, both concentric cylinder rheometry as well as the containerless oscillating droplet measurements were performed. The latter experiments were conducted at the DLR in both an Electrostatic levitation furnace as well as in the TEMPUS Electromagnetic levitation device.

In the low temperature regime, the alloys were all found to exhibit moderately strong liquid behavior with $D^* \approx 25$. Near the melting point, all of the alloys showed fragile liquid behavior, with fragility parameters of about $D^* \approx 10$. These observations are consistent with measurements of other bulk metallic glasses, strongly suggesting the presence of a liquid-liquid transition at intermediate temperatures.

However, direct observation of the S-F transition was obscured by the technical limitations of the experiments. The TMA three point beam bending experiments were limited both by the maximum deflection range and by the onset of crystallization and phase separation. Similarly, Couette viscosity measurements exhibited limited undercooling due to the heterogeneous nucleation of crystals at the crucible walls. The quality of the data was verified through independent measurements conducted in ESL and EML devices. In the absence of surface contaminants, the measurements agree well with those obtained using the oscillating droplet technique. Clear evidence was found for the onset of crystallization, which manifested as a sharp increase in the apparent viscosity upon undercooling. This should not be confused with the strong-fragile transition. The increase in apparent viscosity with crystallization could be clearly observed. In contrast, containerless measurements of the viscosity were not limited by crystallization due to the lack of heterogeneous nucleation sites. This enabled the successful in-situ vitrification of several of the alloys in this system. However, at viscosities greater than ≥ 250 mPa s, the determination of the damping coefficient was hindered by inability of the camera to resolve the oscillations in the droplet.

Despite the technical limitations encountered, the difference between high and low temperature fragility suggests the existence of liquid-liquid transitions in all of the compositions studied and further investigations are necessary to understand the precise nature of this phenomenon. Therefore, a follow-up research project has been established with the DLR to combine containerless ESL techniques with Synchrotron X-ray scattering [20]. This will allow for accurate *in-situ* monitoring of the structural changes in the deeply supercooled liquid state that are otherwise obfuscated by the technical limitations of kinetic

measurements. Similar work has already been performed on Vitreloy 1 [92] and has proven to be capable of identifying not only the structural changes associated with the S-F transition but also the thermodynamic signature, manifesting as a peak in the measured specific heat capacity to emissivity ratio, c_p/ϵ_T. As shown in the present work, containerless ESL measurements are ideal for studying deeply undercooled liquids due to the mitigation of the heterogeneous nucleation of crystals. Furthermore, any crystallization that does occur during a measurement can be readily identifiable via X-ray diffraction techniques. Combining the kinetic viscosity data from this work with knowledge of the underlying structural changes on short- and medium-range length scales will lead to a better understanding of polyamorphism in glass forming systems.

Appendix A

Appendix

A.1 Navier-Stokes Equations

The governing equations for Couette rheometry are simplifications of the Navier-Stokes equations and are based on a multitude of assumptions (as detailed in chapter 3). In this section, the Navier-Stokes equations themselves will be derived from the continuity equations for conservation of mass and momentum. This derivation is available in various forms and is summarized here from references [21, 113, 135, 138, 179].

Continuity equation

The derivation of the conservation equations for fluid motion are based on the changes in any intensive property for a system with a defined control volume. This is best summarized in Reynold's transport theorem, which states that the the total change in an intensive property is the sum of the flow through the boundary of the control volume and any sources or sinks of the property within the boundary, which is represented mathematically as

$$\frac{d}{dt}\int_V L dV = -\int_S L\mathbf{v}\cdot\hat{n}dA - \int_V Q dV \tag{A.1}$$

where left hand term describes the rate change of the intensive property L within the control volume V and the right hand terms describe how much L leaves the control volume, either through volume flux or through so called *sink* flux. The volume flux through a small surface area element dA is given by the product of the area and the velocity component normal to the surface

$\int_S \hat{n} \cdot \mathbf{v} dA$. Meanwhile, the sink flux $\int_V Q dV$ describes the amount of L leaving (or entering) the volume due to some sinks (or sources) within the body.

According to divergence theorem the flux across a closed surface is equivalent to the volume integral of the magnitude of the flow field at any point within the body (represented by ∇). Therefore, it is possible to express the surface flux from Reynold's transport theorem as a volume integral

$$\int_S L\mathbf{v} \cdot \hat{n} dA = \int_V \nabla \cdot (L\mathbf{v})\, dV \tag{A.2}$$

It follows then, that the transport theorem can be rewritten as

$$\frac{d}{dt} \int_V L dV = -\int_V \nabla \cdot (L\mathbf{v}) + Q dV \tag{A.3}$$

By applying Leibniz's rule, it is possible to bring the time derivative within the integral and simplify the expression to

$$\int_V \frac{d}{dt} L + \nabla \cdot (L\mathbf{v}) + Q dV = 0 \tag{A.4}$$

Since the control volume itself is arbitrary, the integrand can be reduced to zero and the result is the general form of the continuity equation

$$\frac{dL}{dt} + \nabla \cdot (L\mathbf{v}) + Q = 0 \tag{A.5}$$

Conservation of Mass

The intensive property that is relevant to the conservation of mass is the density. By substituting density into equation A.5, the general form of the conservation of mass is produced

$$\frac{d\rho}{dt} + \nabla \cdot (\rho\mathbf{v}) + Q = 0 \tag{A.6}$$

The sink term Q is only necessary if fluid is being added or removed from within the control volume (e.g. through a pump). Without any sources or sinks, $Q = 0$ and the equation for conservation of mass can be simplified to

$$\frac{d\rho}{dt} + \nabla \cdot (\rho \mathbf{v}) = 0 \tag{A.7}$$

This is often expressed as the material derivative of the density

$$\frac{D\rho}{Dt} = \frac{d\rho}{dt} + (\mathbf{v} \cdot \nabla)\, \rho = 0 \tag{A.8}$$

where a material derivative describes the temporal rate of change of an intensive property (e.g. $\frac{\partial \rho}{\partial t}$) within a velocity field ($\mathbf{v}$). Therefore, $(\mathbf{v} \cdot \nabla)\, \rho$ represents the derivative of the density along of the velocity vector. For incompressible fluids the density remains constant ($\frac{d\rho}{dt} = 0$) and the continuity equation simplifies further to

$$\nabla \cdot \mathbf{v} = 0 \tag{A.9}$$

The differential form of the continuity equation for an incompressible fluid in cylindrical coordinates is

$$\nabla \cdot \mathbf{v} = \frac{1}{r}\frac{\partial}{\partial r}(r v_r) + \frac{1}{r}\frac{\partial v_\theta}{\partial \theta} + \frac{\partial v_z}{\partial z} = 0 \tag{A.10}$$

Conservation of Momentum

The general form of the Navier-Stokes equations are derived through the conservation of momentum. Newton's second law ($\mathbf{F} = m\mathbf{a}$) can be expressed in terms of body forces $\mathbf{b}$ for a fixed control volume (i.e. fixed number of particles). As a result, Newton's second law for cylindrical coordinates becomes

$$\rho \frac{d}{dt}\mathbf{v}\,(r, \theta, z, t) = \mathbf{b} \tag{A.11}$$

Applying the chain rule to the acceleration term, the expression can be rewritten as

$$\rho\left(\frac{\partial \mathbf{v}}{\partial t}+\frac{\partial \mathbf{v}}{\partial r}\frac{dr}{dt}+\frac{\partial \mathbf{v}}{\partial \theta}\frac{d\theta}{dt}+\frac{\partial \mathbf{v}}{\partial z}\frac{dz}{dt}\right)=\mathbf{b} \tag{A.12}$$

once again, with the help of divergence theorem, this can be rewritten as

$$\rho\left(\frac{\partial \mathbf{v}}{\partial t}+\mathbf{v}\cdot\nabla\mathbf{v}\right)=\mathbf{b} \tag{A.13}$$

which can be rewritten in terms of the material derivative to yield a general expression for the equation of motion for conservation of momentum

$$\rho\frac{D\mathbf{v}}{Dt}=\mathbf{b} \tag{A.14}$$

In order to arrive at a more useful form of the Navier-Stokes equations, equation A.14 must be expanded further by assuming that the general body force term $\mathbf{b}$ is equal to the sum of the forces due to stresses acting on the fluid, $\nabla\cdot\sigma$), as well as specific body forces, ($\mathbf{f}$), such as gravity. The resulting expression is known as the Cauchy momentum equation

$$\rho\frac{D\mathbf{v}}{Dt}=\nabla\cdot\sigma+\mathbf{f} \tag{A.15}$$

in most circumstances, $\mathbf{f}$ can be replaced with $\rho\mathbf{g}$, which accounts for the body forces due to gravitational acceleration. Furthermore, it is necessary to distinguish the volumetric stresses (i.e. pressure) from the deformation stresses (i.e. from viscous shearing). To accomplish this, the second order tensor σ must be rewritten as

$$\sigma_{ij} = \begin{pmatrix} \sigma_{rr} & \tau_{r\theta} & \tau_{rz} \\ \tau_{\theta r} & \sigma_{\theta\theta} & \tau_{\theta z} \\ \sigma_{zr} & \tau_{z\theta} & \sigma_{zz} \end{pmatrix} = - \begin{pmatrix} p & 0 & 0 \\ 0 & p & 0 \\ 0 & 0 & p \end{pmatrix} + \begin{pmatrix} \sigma_{rr} + p & \tau_{r\theta} & \tau_{rz} \\ \tau_{\theta r} & \sigma_{\theta\theta} + p & \tau_{\theta z} \\ \sigma_{zr} & \tau_{z\theta} & \sigma_{zz} + p \end{pmatrix} \tag{A.16}$$

where the first term accounts for the pressure and the second is the deviatoric stress tensor, or simply

$$\sigma_{ij} = -pI + \mathbf{T} \tag{A.17}$$

substituting this into equation A.15 produces the general form of the Navier-Stokes equation

$$\rho \frac{D\mathbf{v}}{Dt} = -\nabla p + \nabla \cdot \mathbf{T} + \mathbf{f} \tag{A.18}$$

In order to expand the Navier-Stokes equation into a more useful form, the stress tensor can be reformulated with knowledge of the viscous behavior of the liquid. The simplest case is for a Newtonian fluid where the flow stress is linearly proportional to the flow velocity. The general form of the stress deviator tensor along a single dimension is then

$$\mathbf{T}_{ij} = \mu \left(\frac{\partial u_i}{\partial x_j} + \frac{\partial u_j}{\partial x_i} \right) + \delta_{ij} \lambda \nabla \cdot \mathbf{v} \tag{A.19}$$

where μ and λ are the first and second coefficients of viscosity and δ_{ij} is the Kronecker delta. It is important to note that this expression is based on the assumption that the deviator tensor is zero in the absence of flow. The second coefficient of viscosity accounts for the viscous strresses due to volume changes. Consequently, under the assumption for an incompressible fluid (i.e. no volume changes), the deviator tensor simplifies to

$$\mathbf{T}_{ij} = \mu \left(\frac{\partial u_i}{\partial x_j} + \frac{\partial u_j}{\partial x_i} \right) \tag{A.20}$$

Substituting equation A.20 into equation A.18 yields the Navier-Stokes equations of motion for an incompressible fluid. For the case of Couette rheometry, it is appropriate to express the equations of motion in cylindrical coordinates.

r-component:

$$\rho\left(\frac{\partial v_r}{\partial t}+v_r\frac{\partial v_r}{\partial r}+\frac{v_\theta}{r}\frac{\partial v_r}{\partial \theta}-\frac{v_\theta^2}{r}+v_z\frac{\partial v_r}{\partial z}\right)= -\frac{\partial p}{\partial r}+\mu\left(\frac{\partial}{\partial r}\left(\frac{1}{r}\frac{\partial\left(rv_r\right)}{\partial r}\right)+\frac{1}{r^2}\frac{\partial^2 v_r}{\partial \theta^2}-\frac{2}{r^2}\frac{\partial v_\theta}{\partial \theta}+\frac{\partial^2 v_r}{\partial z^2}\right)+\rho g_r \tag{A.21}$$

θ-component:

$$\rho\left(\frac{\partial v_\theta}{\partial t}+v_r\frac{\partial v_\theta}{\partial r}+\frac{v_\theta}{r}\frac{\partial v_\theta}{\partial \theta}+\frac{v_r v_\theta}{r}+v_z\frac{\partial v_\theta}{\partial z}\right)= -\frac{1}{r}\frac{\partial p}{\partial \theta}+\mu\left(\frac{\partial}{\partial r}\left(\frac{1}{r}\frac{\partial\left(rv_\theta\right)}{\partial r}\right)+\frac{1}{r^2}\frac{\partial^2 v_\theta}{\partial \theta^2}-\frac{2}{r^2}\frac{\partial v_r}{\partial \theta}+\frac{\partial^2 v_\theta}{\partial z^2}\right)+\rho g_\theta \tag{A.22}$$

z-component:

$$\rho\left(\frac{\partial v_z}{\partial t}+v_r\frac{\partial v_z}{\partial r}+\frac{v_\theta}{r}\frac{\partial v_z}{\partial \theta}+v_z\frac{\partial v_z}{\partial z}\right)= -\frac{\partial p}{\partial r}+\mu\left(\frac{1}{r}\frac{\partial}{\partial r}\left(r\frac{\partial v_z}{\partial r}\right)+\frac{1}{r^2}\frac{\partial^2 v_z}{\partial \theta^2}+\frac{\partial^2 v_z}{\partial z^2}\right)+\rho g_z \tag{A.23}$$

equations A.21, A.22, and A.23 together with equation A.10 are the basis for deriving the working equations for Couette rheometry. For an incompressible Newtonian fluid, these can be summarized (for some general body force, f) as

$$\rho\frac{D\mathbf{v}}{Dt}=-\nabla p+\mu\nabla^2\mathbf{v}+\mathbf{f} \tag{A.24}$$

A.2 Couette rheometer uncertainty

The uncertainty shown in this work for the Couette measurements is calculated from the precision error of the instrument. This is calculated according to the square root of the sum of the uncertainty of each variable

$$u_p = \sqrt{\sum_{i=1}^{N} u_i^2} \tag{A.25}$$

where u_i is the product between the sensitivity of the main governing equation F to a given variable x_i to the standard deviation error of that variable σ_i, or

$$u_i = \frac{\partial F}{\partial x_i}\sigma_i \tag{A.26}$$

The Couette viscosity equation used in this work is

$$\eta = \frac{R_o^2 - R_i^2}{4\pi L R_o^2 R_i^2 c_L} \cdot \frac{\bar{M}}{\omega} \tag{A.27}$$

Accordingly, the precision uncertainty is calculated with

$$u_\eta = \left[\left(\frac{\partial \eta}{\partial R_o}\sigma_{R_o}\right)^2 + \left(\frac{\partial \eta}{\partial R_i}\sigma_{R_i}\right)^2 + \left(\frac{\partial \eta}{\partial L}\sigma_L\right)^2 + \left(\frac{\partial \eta}{\partial c_L}\sigma_{c_L}\right)^2 + \left(\frac{\partial \eta}{\partial \bar{M}}\sigma_{\bar{M}}\right)^2 + \left(\frac{\partial \eta}{\partial \omega}\sigma_\omega\right)^2 \right]^{1/2} \tag{A.28}$$

the sensitivity for each variable is given in table A.1. The errors for the average torque $\sigma_{\bar{M}}$ and angular speed of the bob σ_ω are calculated with the analysis program according to the standard deviation from the mean of the measured values. The error for the correction length term σ_{c_L} is determined from calibrations with standard oils.

Table A.1: Couette viscosity uncertainty

Variable x_i	Sensitivity $\frac{\partial F}{\partial x_i}$	error σ_i
R_o	$\frac{\partial \eta}{\partial R_o} = \frac{1}{2\pi R_o^3 L c_L}\frac{\bar{M}}{\omega}$	$\sigma_{R_o} = 5 \times 10^{-4}$ m
R_i	$\frac{\partial \eta}{\partial R_i} = -\frac{1}{2\pi R_i^3 L c_L}\frac{\bar{M}}{\omega}$	$\sigma_{R_i} = 5 \times 10^{-4}$ m
L	$\frac{\partial \eta}{\partial L} = -\frac{R_o^2 - R_i^2}{4\pi R_o^2 R_i^2 L^2 c_L}\frac{\bar{M}}{\omega}$	$\sigma_L = 5 \times 10^{-4}$ m
c_L	$\frac{\partial \eta}{\partial c_L} = -\frac{R_o^2 - R_i^2}{4\pi R_o^2 R_i^2 L c_L^2}\frac{\bar{M}}{\omega}$	$\sigma_{c_L} = 1 \times 10^{-1}$
$\bar{M}$	$\frac{\partial \eta}{\partial \bar{M}} = \frac{R_o^2 - R_i^2}{4\pi R_o^2 R_i^2 L c_L}\frac{1}{\omega}$	$\sigma_{\bar{M}}$ =measured
ω	$\frac{\partial \eta}{\partial \omega} = -\frac{R_o^2 - R_i^2}{4\pi R_o^2 R_i^2 L c_L}\frac{\bar{M}}{\omega^2}$	σ_ω =measured

A.3 Three point beam bending uncertainty

The method for calculating the uncertainty in section A.2 was also applied to the three point beam bending measurements. Substituting $I_c = bh^3/12$ and $A = bh$ into equation 4.13 gives

$$\eta = -\frac{gL^3}{12bh^3v}\left[M + \frac{\rho bhL}{1.6}\right] \tag{A.29}$$

The corresponding uncertainty is then

$$u_\eta = \left[\left(\frac{\partial\eta}{\partial g}\sigma_g\right)^2 + \left(\frac{\partial\eta}{\partial L}\sigma_L\right)^2 + \left(\frac{\partial\eta}{\partial b}\sigma_b\right)^2 + \left(\frac{\partial\eta}{\partial h}\sigma_h\right)^2 + \left(\frac{\partial\eta}{\partial v}\sigma_v\right)^2 + \left(\frac{\partial\eta}{\partial M}\sigma_M\right)^2 + \left(\frac{\partial\eta}{\partial\rho}\sigma_\rho\right)^2\right]^{1/2} \tag{A.30}$$

where the uncertainties and errors are listed in table A.2. Note that the uncertainty in material density varies depending on the composition, therefore the uncertainty of $\sigma_\rho = 1\%$ was used as an approximation. Similarly, the uncertainty in the measured deflection rate depends on the LVDT sensor's accuracy, and a conservative estimate of $\sigma_v = 1\%$ is used in this work.

Table A.2: Three point beam bending viscosity uncertainty

Variable x_i	Sensitivity $\frac{\partial F}{\partial x_i}$	error σ_i
g	$\frac{\partial\eta}{\partial g} = -\frac{L^3}{12bh^3v}\left[M + \frac{\rho bhL}{1.6}\right]$	$\sigma_g = 9.8 \times 10^{-2}$ m s^{-2}
L	$\frac{\partial\eta}{\partial L} = -\frac{gL^2}{12bh^3v}\left[3M + \frac{4\rho bhL}{1.6}\right]$	$\sigma_L = 5 \times 10^{-4}$ m
b	$\frac{\partial\eta}{\partial b} = \frac{gL^3}{12b^2h^3v}$	$\sigma_b = 5 \times 10^{-4}$ m
h	$\frac{\partial\eta}{\partial h} = \frac{gL^3}{12bh^4v}\left[3M + \frac{2\rho bhL}{1.6}\right]$	$\sigma_h = 5 \times 10^{-4}$ m
M	$\frac{\partial\eta}{\partial M} = -\frac{gL^3}{12bh^3v}$	$\sigma_M = 1 \times 10^{-4}$ kg
ρ	$\frac{\partial\eta}{\partial\rho} = -\frac{gL^4}{19.2h^2v}$	$\sigma_\rho = 1\%$
v	$\frac{\partial\eta}{\partial v} = \frac{gL^3}{12bh^3v^2}\left[M + \frac{\rho bhL}{1.6}\right]$	$\sigma_v = 1\%$

References

[1] Tempus bildverarbeitung. Technical Report Hb 2435-1, S.E.A. Datentechnik GmbH, 2007.

[2] G. Adam and J.H. Gibbs. *J. Chem. Phys.*, 43:139, 1965.

[3] A.L. Greer A.L. Drehman and D. Turnbull. *Appl. Phys. Lett.*, 41:716, 1982.

[4] C.A. Angell. *J. Non-Cryst. Solids*, 102:205–221, 1988.

[5] C.A. Angell. *Science*, 267:1924–1935, 1995.

[6] C.A. Angell. *Science*, 319:582–587, 2008.

[7] A. S. Argon. *Acta Metallurgica*, 27:47–58, 1979.

[8] A. S. Argon and H. Y. Kuo. *Mater. Sci. and Eng.*, 39:101–109, 1979.

[9] M. F. Ashby and A. L. Greer. *Scripta Mater.*, 54:321–326, 2005.

[10] H.V. Atkinson. *Progress in Materials Science*, 50:341–412, 2005.

[11] M. Avrami. *J. Chem. Phys.*, 7:1103, 1939.

[12] I. Avramov. *Phys. Chem. Glasses*, 48:61–63, 2007.

[13] H.A. Barnes. *Journal of Rheology*, 33:329, 1989.

[14] J.D. Bernal and J. Mason. *Nature*, 188:910, 1960.

[15] W.H. Boersma. *AIChE Journal*, 36:321, 1990.

[16] H. Brenner. *Int. J. Multiphase Flow*, 1:195–341, 1974.

[17] J. Brillo and I. Egry. *Int. J. Thermophysics*, 24:1155–1170, 2003.

[18] R. Busch. *JOM*, 52:39–42, 2000.

[19] R. Busch. Electrostatic levitation investigation of the temperature dependent rheological and volumetric changes of molten zr-based bulk metallic glass forming alloys. DFG proposal BU2276 6-1, Saarland University, 2012.

[20] R. Busch. Kinetic and structural investigations of deeply undercooled zr-based bulk metallic glass forming liquids. DFG proposal BU2276 6-2, Saarland University, 2015.

[21] S. Chandrasekhar. *Hydrodynamic and Hydromagnetic Stability.* Oxford University Press, 1961.

[22] H.S. Chen. *Acta Metall.*, 22:1505, 1974.

[23] H.S. Chen and D. Turnbull. *J. Chem. Phys.*, 48:2560, 1968.

[24] H.S. Chen and D. Turnbull. *Acta Metall.*, 17:1021, 1969.

[25] H. Cohen and D. Turnbull. *J. Chem. Phys.*, 31:1164, 1959.

[26] C.R. Crowell. *Solid-State Electronics*, 8:395–399, 1965.

[27] D.L. Cummings and D.A. Blackburn. *J. Fluid Mech.*, 224:395–416, 1991.

[28] K. Easterling D. Porter and M. Sherif. *Phase Transformations in Metals and Alloys.* CRC Press, 2009.

[29] E.A. DiMarzio and J.W. Gibbs. *J. Chem. Phys.*, 28:807, 1958.

[30] E.A. DiMarzio and J.W. Gibbs. *J. Polym. Sci.*, 40:121, 1959.

[31] E.A. DiMarzio and J.W. Gibbs. *J. Polym. Sci., A*, 1:1417, 1963.

[32] A.K. Doolittle. *J. Appl. Phys.*, 22:1471, 1951.

[33] I. Egry. *J. Mat. Science*, 26:2997–3003, 1991.

[34] I. Egry and J. Brillo. *J. Chem. Eng. Data*, 54:2347–2352, 2009.

[35] I. Egry and D. Holland-Moritz. *Eur. Phys. J. Special Topics*, 106:131–150, 2011.

[36] A. Einstein. *Annalen der Physik*, 17:549, 1905.

[37] A. Einstein. *Ann. Phys.*, 34:592, 1911.

[38] A. Inoue et al. *Material Transactions, JIM*, 30:965, 1990.

[39] A. Inoue et al. *Material Transactions, JIM*, 31:177, 1990.

[40] A. Inoue et al. *Material Transactions, JIM*, 32:609, 1991.

[41] A. Inoue et al. *Material Transactions, JIM*, 34:351, 1992.

[42] A. Inoue et al. *Materials Transactions, JIM*, 34:1234, 1993.

[43] A. Wiest et al. *Scripta Materialia*, 60:160–163, 2008.

[44] B. Spencer et al. *Metallurgical Trans.*, 3:1925–1932, 1972.

[45] C. A. Schuh et al. *Acta Mater.*, 55:4067–4109, 2007.

[46] C. Huang et al. *PNAS*, 106:15214–15218, 2009.

[47] C. Way et al. *Acta Materialia*, 55:2977–2983, 2007.

[48] C. Way et al. *J. Alloys and Compounds*, 434-435:88–91, 2007.

[49] C. Zhang et al. *J. Chem. Phys.*, 133:014508, 2010.

[50] C. Zhang et al. *Chin. Phys. Lett.*, 11:116401, 2010.

[51] C.T. Moynihan et al. *J. Phys. Chem.*, 78:2673–2677, 1974.

[52] C.T. Moynihan et al. *J. Am. Ceram. Soc.*, 59:12–16, 1976.

[53] C.T. Moynihan et al. *Thermochimica Acta*, 280:153–162, 1996.

[54] D.A. Ditmars et al. *Journal of Reasearch of the National Bureau of Standards*, 87(2), 1982.

[55] D.M. Herlach et al. *Int. Mat. Reviews*, 38:273–347, 1993.

[56] F. Faupel et al. *Reviews of Modern Physics*, 75:237, 2003.

[57] G. Kumar et al. *Nature*, 457:868–872, 2009.

[58] G. Kumar et al. *Appl. Phys. Lett.*, 97:101907, 2010.

[59] G.N. Greaves et al. *Science*, 322:566–570, 2008.

[60] G.R. Heal et al. *Principles of Thermal Analyis and Calorimetry*. Royal Society of Chemistry, 2007.

[61] H.M. Chiu et al. *Scripta Materialia*, 61:28–31, 2009.

[62] H.W. Sheng et al. *Nature Materials*, 6:192–197, 2007.

[63] I. Egry et al. *Int. J. Thermophysics*, 13:65–74, 1992.

[64] I. Egry et al. *Meas. Sci. Tech.*, 16:426–431, 2005.

[65] I. Gallino et al. *J. Appl. Phys.*, 108:063501, 2010.

[66] I. Saika-Voivod et al. *Nature*, 412:514–517, 2001.

[67] J. Heinrich et al. *Appl. Phys. Lett.*, 100:071909, 2012.

[68] J.-L. Barrat et al. *Molecular Simulation*, 20:17–25, 1997.

[69] J. Loeffler et al. *Appl. Phys. Lett.*, 77:525–527, 2000.

[70] J. Loeffler et al. *J. Appl. Phys.*, 89:1573–1579, 2001.

[71] J.-M. Liu et al. *Phys. Stat. Sol. B*, 199:379, 1997.

[72] J. Schmitz et al. *Int. J. Mat. Res.*, 100:1529, 2009.

[73] J. Schroers et al. *Scripta Materialia*, 57:341–344, 2007.

[74] J.M. Piau et al. *Rheol. Acta*, 33:357–368, 1994.

[75] J.P. Chu et al. *Appl. Phys. Lett.*, 90:034101, 2007.

[76] K. Ito et al. *Nature*, 398:492–495, 1999.

[77] K. Mukai et al. *ISIJ Int.*, 40:suppl. S148–S152, 2000.

[78] K. Ohsaka et al. *Appl. Phys. Lett.*, 70:726–728, 1997.

[79] L. Rhim et al. *Acta Mater.*, 59:2166–2171, 2011.

[80] L. Xu et al. *PNAS*, 102:16558–16562, 2005.

[81] L. Xu et al. *Proc. Nat. Acad. Sci.*, 102:16558, 2005.

[82] M. Hemmati et al. *J. Chem. Phys.*, 115:6663, 2001.

[83] M.A. DeBolt et al. *J. Am. Ceram. Soc.*, 59:16–21, 1976.

[84] O. Kubaschewski et al. *Materials Thermochemistry*. Pergamon Press, New York, 6th edition, 1993.

[85] O. Mishima et al. *Nature*, 314:76–78, 1985.

[86] P. Scheidler et al. *Phys. Rev. B*, 63:104204, 2001.

[87] Q. Zeng et al. *Phys. Rev. Lett.*, 104:105702, 2010.

[88] R. D. Conner et al. *J. Appl. Phys.*, 94:904, 2003.

[89] R. Willnecker et al. *Appl. Phys. Lett.*, 49:1339, 1986.

[90] S. Mueller et al. *Proc. R. Soc. A*, 466:1201–1228, 2010.

[91] S. Tamura et al. *J. Chem. Thermodyn.*, 7:633, 1975.

[92] S. Wei et al. *Nature Communications*, 4:2083, 2013.

[93] S.C. Glade et al. *J. Appl. Phys.*, 87:7249–7251, 2000.

[94] T. Kordel et al. *Physical Review B*, 83:104205, 2011.

[95] T.A. Waniuk et al. *Acta mater.*, 46:5229–5236, 1998.

[96] T.Y. Liu et al. *Metallurgical and Mater. Trans. A*, 34:409–417, 2003.

[97] V. Rudnev et al. *Handbook of Induction Heating.* Marcel Dekker AG, 2003.

[98] W. Pabst et al. *J. Eur. Ceram. Soc.*, 26:149–160, 2006.

[99] W.K. Rhim et al. *Review of Scientific Instruments*, 64:2961, 1993.

[100] Z. Evenson et al. *Scripta Materialia*, 63:573–576, 2010.

[101] Z. Evenson et al. *Acta Mater.*, 60:4712, 2012.

[102] Z. Zhou et al. *Journal of Crystal Growth*, 257:350–358, 2003.

[103] Z. Evenson. *On the thermodynamic and kinetic properties of bulk glass forming metallic systems.* PhD thesis, Saarland University, 2012.

[104] Z. Evenson and R. Busch. *Acta Materialia*, 59:4404–4415, 2011.

[105] M.C. Flemings. *Metallurgical Trans. A*, 22:957–972, 1991.

[106] T.G. Fox and P.J. Flory. *J. Am. Chem. Soc.*, 70:2384, 1948.

[107] T.G. Fox and P.J. Flory. *J. Phys. Chem.*, 55:221, 1951.

[108] T.G. Fox and P.J. Flory. *J. Polym. Sci.*, 14:315, 1954.

[109] G.S. Fulcher. *J. Am. Ceram. Soc.*, 6:339, 1925.

[110] S. Gaertner. Untersuchung ... $\mathrm{zr}_{60.0}\mathrm{cu}_{25.0}\mathrm{al}_{15.0}$. Master's thesis, Saarland University, 2015.

[111] J.H. Gibbs and E.A. DiMarzio. *J. Chem. Phys.*, 28:373–383, 1958.

[112] H.M. Gibson and N.B. Wilding. *Phys. Rev. ESL*, 73:061507, 2006.

[113] V. Girault and P.A. Raviart. *Finite Element Methods for Navier-Stokes Equations: Theory and Algorithms.* Springler-Verlag, 1986.

[114] SGL Carbon GmbH. Sigrafine r6710 data sheet. http://www.sglgroup.com/cms/_common/downloads/products/product-groups/gs/tds/iso/SIGRAFINE_TDS-R6710_DE.02.pdf, 2015. Online; accessed 01.10.15.

[115] G. Gottstein. *Physikalische Grundlagen der Materialkunde.* Springer-Verlag, 2007.

[116] A.P. Gray. *Analytical Calorimetry.* Plenum Press, New York, 1968.

[117] G. Grest and H. Cohen. *Adv. Chem. Phys.*, 48:455, 1981.

[118] E. Guth and O. Gold. *Phys. Rev.*, 53:322, 1938.

[119] J.H. Simmons H. Tweer and P.B. Macedo. *J. Chem. Phys.*, 54:1952, 1971.

[120] H.E. Hagy. *J. Am. Ceram. Soc.*, 46, 1963.

[121] J. Heinrich. *Massivglasbildende metallische Legierungen als Konstruktionswerkstoff.* PhD thesis, Saarland University, 2012.

[122] W. Hembree. Improvements to ... alloy. Master's thesis, Saarland University, 2010.

[123] A. Inoue. *Material Transactions, JIM*, 36:866, 1995.

[124] A. Gebert J. R. Scully and J. H. Payer. *J. Mater. Res.*, 22, 2006.

[125] K.A. Jackson. *Liquid Metals and Solidification.* ASM, 1958.

[126] E.A.P.R. Jagla. *Phys. Rev. E*, 58:1478, 1998.

[127] W.A. Johnson and R.F. Mehl. *Trans. AIME*, 135:416, 1939.

[128] I. Jonas. *To be decided*. PhD thesis, Saarland University, 2016.

[129] W. Kauzmann. *Chem. Rev.*, 43:219–256, 1948.

[130] R. Kohlrausch. *Annalen der Physik und Chemie*, 91:56–82, 1854.

[131] A.N. Kolmogorov. *Izv. Akad. Nauk. SSR*, 3:355, 1937.

[132] I.M. Krieger. *Adv. Colloid Interface Sci.*, 3:111–136, 1972.

[133] K.S. Lee and Y.W. Chang. *Mater. Sci. and Eng. A*, 399:238–243, 2005.

[134] H.M. Lu and Q. Jiang. *J. Phys. Chem. B*, 109:15463–15468, 2005.

[135] C. W. Macosko.

[136] R. Manley and S. Mason. *Can. J. Chem.*, 33:763–773, 1955.

[137] D. Matyushov and C.A. Angell. *J. Chem. Phys.*, 126:AN 094501, 2007.

[138] T.G. Mezger. *The Rheology Handbook, 3rd Revised Edition*. Vincentz Network GmbH and Co, 2011.

[139] K.C. Mills and Y.C. Su. *International Materials Reviews*, 51:329–351, 2006.

[140] D.B. Miracle. *Nature Materials*, 3:697, 2004.

[141] D.B. Miracle. *Acta Mater.*, 54:4317–4336, 2006.

[142] C.T. Moynihan and C.A. Angell. *J. Non-Crystal. Sol.*, 274:131, 2000.

[143] S.V. Nemilov. *Glass Phys. Chem.*, 21:91, 1995.

[144] I. Newton. *Philosophiæ Naturalis Principia Mathematica*. 1967.

[145] NIST. *NIST Special Publication*, 96:2008, 2010.

[146] D.W. Oxtoby. *J. Phys. Condens. Matter*, 4:7627–7650, 1992.

[147] A. Peker and W. L. Johnson. *Appl. Phys. Lett.*, 63:2342, 1993.

[148] A. Peker and W. L. Johnson. *U.S. Patent*, No. 5288344, 1994.

[149] I.R. Rutgers. *Rheologica Acta*, 2:202–210, 1962.

[150] H. Laider S. Glasstone and H. Eyring. *The Theory of Rate Processes*. Princeton Univ. Press, 1941.

[151] S. Sarian and J. Criscione. *Journal of Applied Physics*, 38:1794–1798, 1967.

[152] J. Schroers. *JOM*, 57:35–39, 2005.

[153] J. Schroers. *Acta Mater.*, 56:471–478, 2008.

[154] J. Shi. *U.S. Patent*, No. 0177316 A1, 2005.

[155] S.Y. Shiraishi and R.G. Ward. *Canadian Metallurgical Quarterly*, 3:117–122, 1964.

[156] R.B. Sosman. *The properties of silica; an introduction to the properties of substances in the solid non-conducting state*. Book Dept., the Chemical Catalog Co., 1927.

[157] F. Spaepen. *Scripta Mater.*, 54:363–367, 2006.

[158] F.H. Stillinger. *J. Chem. Phys.*, 88:7818–7825, 1988.

[159] F.H. Stillinger and P.G. Debenedetti. *Annu. Rev. Condens. Matter Phys.*, 4:263–285, 2013.

[160] C. Suryanarayana and A. Inoue. *Bulk Metallic Glasses*. CRC Press, Taylor and Francis Group, 2011.

[161] G. Tammann and G. Hesse. *Z. anorg. Alleg. chem.*, 156:245, 1926.

[162] S. Tamura and T. Yokokawa. *Bull. Chem. Soc. Japan*, 48:2542, 1975.

[163] C.V. Thompson and F. Spaepen. *Acta Metallurgica*, 31:2021–2027, 1983.

[164] M. M. Trexler and N. N. Thadhani. *Prog. Mater. Sci.*, 55:759–839, 2010.

[165] F.T. Trouton. *Proc. Roy. Soc. London*, 77:426, 1906.

[166] D. Turnbull. *J. Appl. Phys.*, 21:1022, 1950.

[167] D. Turnbull. *J. Chem. Phys.*, 18:198, 1950.

[168] D. Turnbull. *J. Appl. Phys.*, 18:769, 1950.

[169] D. Turnbull. *J. Chem. Phys.*, 18:768, 1950.

[170] D. Turnbull. *Contemporary Physics*, 10:473–488, 1969.

[171] D. Turnbull and R.E. Cech. *J. Appl. Phys.*, 21:804, 1950.

[172] D. Uhlmann. *J. de Physique Colloques*, 43:175–190, 1982.

[173] V. Vand. *J. Phys. Colloid Chem.*, 52:277–299, 1948.

[174] H. Vogel. *Phys. Z.*, 22:645, 1921.

[175] M. Volmer. *Zeitschrift für Elektrochemie*, 35:555–561, 1929.

[176] R.H. Willens W. Clement and P. Duwez. *Nature*, 187:869, 1960.

[177] J.K. Weber. *Int. J. Appl. Glass Sci.*, 1:248–256, 2010.

[178] S. Wei. *Kinetic, thermodynamic, and structural transitions in order-disorder alloys and bulk metallic glass-forming alloys*. PhD thesis, Saarland University, 2014.

[179] Wikepedia. Derivation of the navier–stokes equations. https://en.wikipedia.org/wiki/Derivation_of_the_Navier_Stokes_equations, 2015. Online; accessed 01.10.15.

[180] G. Williams and D.C. Watts. *Trans. Faraday Soc.*, 66:80–85, 1970.

[181] J.G. Ziegler and N.B. Nichols. *Transactions of the ASME*, 64:759–768, 1942.